DOI:10.15774/PPKE.ITK.2015.006

Compressed sensing in FET based terahertz imaging

Gergelyi Domonkos
A thesis submitted for the Doctor of Philosophy

Pázmány Péter Catholic University
Faculty of Information Technology and Bionics
Roska Tamás Doctoral School of Sciences and Technology

Supervisor
Péter Földesy, Ph.D.

Budapest, 2014

DOI:10.15774/PPKE.ITK.2015.006

T É M A V E Z E T Ő I N Y I L A T K O Z A T O K

1. PUBLIKÁCIÓS TELJESÍTMÉNY

Alul írott *Dr. Földesy Péter* Témavezető nyilatkozom, hogy *Gergelyi Domonkos* doktorjelölt publikációs teljesítménye **megfelel** a doktori (PhD) fokozatszerzési eljárás előfeltételeként a Tudományterületi Doktori és Habilitációs Tanács által támasztott követelményeknek.

2. PhD disszertáció

Alul írott *Dr. Földesy Péter* Témavezető nyilatkozom, hogy *Gergelyi Domonkos* doktorjelölt benyújtott doktori munkájában meghatározott téma tudományosan értelmezhető, hiteles adatokat tartalmaz, az abban foglalt tudományos eredmények a jelölt saját tudományos eredményei, az értekezés megfelel a PPKE PhD szabályzat, és a MMT DI SzMSz előírásainak.
A PhD disszertáció nyilvános vitára történő benyújtását **támogatom.**

2015. Május 13.

.....

Dr. Földesy Péter, PhD, Egyetemi docens, PPKE-ITK

DOI:10.15774/PPKE.ITK.2015.006

Table of Contents

DOI:10.15774/PPKE.ITK.2015.006

Structure of the work

After a short introduction of the field in section 1, I summarize the long-term aims of the terahertz research group at the Computational Optical Sensing and Processing Laboratory (COSPL) that drove the work during the past years. I continue with describing the utilized setup giving also an insight to the process of the project that helps to clearly position my own contribution.

The third section constitutes the core of this thesis starting with the general approach of my investigations and an overview of the used methods. Then, I present the scientific results of my work.

In the next part, a collection of some measurements brings the work closer to the reader demonstrating the technological problems and challenges of terahertz sensing. I close the work by outlining the conclusions and discussing the fields of application.

For several sections of the document, I utilized the text of my publications word by word as concise description of a number of topics (especially [2]).

DOI:10.15774/PPKE.ITK.2015.006

List of Abbreviations and Symbols

2DEG	Two Dimensional Electron Gas
ADC	Analog to Digital Converter
AMC	Amplifier Multiplier Chain
BP	Basis Pursuit
BPDN	Basis Pursuit Denoising
BSIMv3	A physics based circuit simulation model of a MOSFET developed by the UC Berkeley Device Group; version 3.0; first industry-wide standard, 1996
CCD	Charge-coupled Device
CMOS	Complementary Metal Oxide Semiconductor
CoSa	Compressed Sampling
CoSaMP	An optimal CS reconstruction algorithm regarding, the reconstruction error, and the number of measurements
COSPL	Computational Optical Sensing and Processing Laboratory of the ICSC
CS	Compressed Sensing
CV	Cross-validation
CW	Continuous Wave
DAQ	Data Acquisition
DMD	Digital Micromirror Device
FET	Field Effect Transistor
FFT	Fast Fourier Transform
FPA	Focal Plane Array
ICSC – HAS	Institute for Computer Science and Control of the Hungarian Academy of Sciences
IMPATT diode	IMPact ionization Avalance Transit-Time diode; high power semiconductor diode; oscillator, amplifier in the range 3-100 GHz
ITU	International Telecommunications Union
LC	Liquid crystal
LNA	Low Noise Amplifier
MOS	Metal Oxide Semiconductor
NA	Numerical Aperture
NEP	Noise Equivalent Power
NF	Noise Figure
OMP	Orthogonal Matching Pursuit
PSD	Phase Sensitive Detection
SLM	Spatial Light Modulator
SNR	Signal to Noise Ratio

DOI:10.15774/PPKE.ITK.2015.006

SoC	System on Chip
THF	Tremendously High Frequency band (ITU) or THz; 300 GHz – 3 THz
THz	Terahertz; frequency of 10^{12} Hz
VLSI	Very Large Scale Integration
YIG	Yttrium Iron Garnet
ρ-Si	High resistivity silicon

---

t_{int}	It is used if no capacitance is considered inside the pixel, only integration after the LNA; therefore, $t_{int} = t_{int2}$
t_{int1}	In-pixel integration ratio (referenced to 0.5s – that is the base of NEP calculation by definition); also known as the relative integration time; this assumes an integrating capacitance inside the pixel (below the antenna) – hence, very limited – we assume no in pixel capacitance
t_{int2}	Relative integration time after the LNA ($t_{int2} = (\text{int. time in sec})/0.5\ \text{sec}$); otherwise the same as the in-pixel integration ratio or relative int. time
M_{pc}	Number of needed CS measurements per cluster ($M_{pc} < N_{pc}$) to be able to reconstruct all, N_{pc} number of pixel values within the cluster
N_{cs}	The average number of active pixels in the CS patterns (within the integration time)
N_{pc}	Number of pixels per cluster (pixel cluster size)
P_{total}	Total noise power of a detector transistor
T_0	290 K
$f_{s_{max}}$	The theoretical, summed maximum sampling frequency of all A/D unit working as a single unit in an ideal, time interleaved fashion
f_s	Sampling frequency of the A/D converters (we assume the total resources available for A/D is limited by the chip area; $f_s = f_{s_{max}}/r$)
f_{sm}	The modulation frequency of the source; it is used for the lock-in detection that is the assumed basic measurement scheme
fps	Acquisition speed; frame per second
L_0 norm	The "sparsity" of a vector; see section 1.2 for details
L_1 norm	The "absolute value norm" of a vector; see section 1.2 for details
λ	Wavelength
B	Bandwidth of the measurement (usually determined by the lock-in amplifier – f_{sm})
M	Number of needed CS measurements to reconstruct the image; at an estimated average compression: $M \approx 4s \log(N)$, if the image is s-sparse; it is for the whole image in contrast to M_{pc} that considers only a small cluster
N	Number of pixels in the imager
NF	Noise figure of the LNA

DOI:10.15774/PPKE.ITK.2015.006

S	Sample count (see definition in section 3.3.1)
k	Number of pixel clusters
r	Number of A/D converters; we assume ideal resource sharing; $r = k$
$\boldsymbol{x}$	The signal/image to be measured, rearranged in a vector form (column wise repacking, where the columns get below each other)
$\boldsymbol{y}$	The measurement vector; $\boldsymbol{y} \in \mathbb{R}^{\mathbf{M}}$ – it stores a single value for each measurement
$\boldsymbol{\phi}$	Measurement matrix; consisting of the patterns as its rows; $\boldsymbol{\phi} \in \mathbb{R}^{\mathbf{M}\times\mathbf{N}}$
η	Efficiency of summation at the compressed sampling (here ~0.81); summing the unity signal of N pixels, results in a signal amplitude: $N\eta$

DOI:10.15774/PPKE.ITK.2015.006

1 INTRODUCTION

1.1 Introduction of the field

1.1.1 Terahertz sensing

Terahertz science is a relatively new, fast developing research area that covers the electromagnetic spectrum from 0.1 THz to 30 THz. Its main topics cover the info-communication field and sensing in general. Astronomy was its first application field, where imaging started. Since then, surveillance applications came to everyday use to help security screening in avionics. The non-destructing imaging capabilities proved its usefulness for historians as well, by giving insight to ancient, closed crocks. Surface inspection, material characterization and biological observation are also in the forefront. Spectroscopy developed a lot since the beginnings; the new techniques provide much more information about molecular fine structures.

Non-invasive inspection of cell cultures and thick excisions of various tissues paved the way for the first clinical in-vivo application: breast cancer diagnosis [2].

1.1.2 Terahertz spectroscopy

The 0.1 THz to 30 THz frequency spectrum covers the $0.4 \cdot 10^{-3}$ – $120 \cdot 10^{-3}$ eV energy range. Thus, the electromagnetic field affects rotational and vibrating modes of the molecules making it applicable to gather information about the molecular structure of the objects and to characterize compounds via recording such features.

Investigations in this field started quite early in the 60s and 70s [3]. Since then, the aim has not changed much yet: increase accuracy further and further to create ever finer spectral traces and determine the observed molecular structure more faithfully.

With development of the technology many other subfield emerged and lower part of the spectrum, the THF band became more easily measurable (for instance the Schottky diode sources and detectors of the Bell Labs got widespread accessible).

Several methods are available to unveil spectral patterns of substances. Complementary or alternative approaches might provide the same spectral features (peaks) with different relative amplitudes, when the intensity values result from variant underlying processes. By way of example Raman spectroscopy, infrared spectroscopy and incoherent inelastic neutron scattering based crystallography relay on fundamentally different interactions.

However, there are many equivalent techniques giving the same results at different speed, precision and complexity.

DOI:10.15774/PPKE.ITK.2015.006

1.1.2.1 Time domain spectroscopy (TDS)

This proven technique is popular in the field of terahertz inspection, where a non-linear crystal such as ZnTe or $LiNbO_3$ converts the power of a pulsed laser source to terahertz radiation. The laser beam is divided to object and reference beams to allow the reference beam gating the detector through a delay line. This fine controlled delayed gating signal makes possible to scan the generated THz pulse in an iterative manner. All techniques utilizing such a conversion have advantage at in-vivo measurements as the probe consisting only the converter crystal and the detector can be "powered" through flexible, fiber cables. This makes the setup compact and ergonomic allowing probing arbitrary parts of the body in a diagnostic setup. The head of the probe can be relatively small with a silicon lens at its tip that couples the terahertz radiation from the crystal into the skin on a short traveling path and vice versa, gathering the backscattered signal from a greater solid angle. Then the sources of reflection are differentiated on a time of flight basis.

1.1.2.2 Raman spectroscopy

Matured forms of Raman spectroscopy use mainly gratings with CCD sensors providing a relatively simple and fast way of spectral recording. However, spontaneous inelastic scattering used in Raman spectroscopy is generally weak compared to the elastic scattering portion. Thus, efficient filtering of the emitted, frequency shifted photons is essential. Several improvements exist that increase the ratio of Raman - Rayleigh scattering to enhance the signal that is orders of magnitude lower in power than the irradiating beam.

Even so, the acquisition provides reliable and specific data by its nature: the indirect detection with the high frequency filtering lowers the disturbing sources within the signal. Therefore, this technology is among the firsts reaching the market with real non-invasive diagnostic applications. The Verisante Aura™ can differentiate malignant and premalignant lesions from benign tissue at 99 % sensitivity according to the survey of the inventors [4]. The device performs single point, in-vivo measurements on the surface of the human tissue 'in less than a second'. The spectral features consist of intensity values at 14 discrete frequencies. Although, there are other variants that can create 2D or even 3D images (at a significantly lower speed).

1.1.3 Terahertz imaging

Several imaging solution exist in the field; their spectrum ranges from handheld devices to near-field microscopes. Both continuous wave (CW) and pulsed sources are applicable. Electro-optical setups relay on pulsed laser sources and non-linear crystals that convert from the range of the laser source to the terahertz domain and vice versa. Then, CMOS or CCD detectors acquire the pixel information, even at real-time rate. This solution is fast and specific features of pulsed sources can be exploited for instance gating with the laser pulse (TDS, time of flight,

DOI:10.15774/PPKE.ITK.2015.006

lock-in detection). However, the achievable SNR is moderate due to the low conversion efficiencies. Another point is the needed bulky and expensive laser source.

Terahertz focal plane arrays consist of bolometers, Schottky diodes and antenna coupled FETs among others. Surface plasmon technology just emerges and promises the possibility of wide band high sensitivity detection.

Room temperature bolometers have higher noise equivalent power (NEP) values 10^{-8}–10^{-9} W/√Hz and their settling time is in the millisecond range.

Schottky diodes – developed at the Bell Labs in the late 60s – mean a matured technology providing NEP on the order of 10^{-9} W/√Hz and a settling time of nanoseconds [5].

The theory of two dimensional electron gas (2DEG) peaked at the development of antenna coupled FETs that can be embedded to standard, silicon based planar technologies as well ensuring reliable, simple and cost effective designs with the possibility for high scale integration. Antenna coupled FETs achieve 10^{-11} –10^{-12} W/√Hz NEP; however, NEP values of 10^{-20} W/√Hz are the theoretical lower bounds of the technology utilizing mixing and assuming a local oscillator power of 10 μW. As local oscillator technology develops, this branch of detector design can be interesting for future THz focal plane array (FPA) research.

The real importance of we are allowed to use standard MOS technologies is one can omit costly post processing steps that are not part of the planar technology (for instance connecting and fitting extra metal layers to the chip surface at a given distance). This also means that proof-of-concept designs may easily turn into mass production and – last, but not least – research groups without semiconductor fabricating facilities are able to create terahertz detectors as well. (This is how the COSPL could also investigate FET based THz sensing.)

2D and 3D electron plasma theory predicted the DC response of FET detectors to THz radiation and their behavior around instability. However, their in-circuit models failed to explain all the experimental results. Földesy gave a sound model in [6] that covers all biasing configurations.

1.1.3.1 Fourier pattern imaging

For Fourier pattern imaging (FPI), consider one mirror collimates the THz beam. Then, the object diffracts these parallel rays that a second mirror focuses in the end. In this general configuration, directly the Fourier transform of the object shows up in the focal plane whose acquired, spatially quantized variant will be denoted by "U". The inverse Fourier transform of the registered intensity image reconstructs a real picture of the object (V). The resolution of this resulting image (Δx, Δy) depends on the screen size (U_{dimX}, U_{dimY}). (I consider the screen as the registered spatial area – now, in the focal plane; unless scanning occurs, it equals the size of the sensor.) In ideal case:

$$\Delta x = \lambda f / U_{dimX} , \qquad (1)$$

DOI:10.15774/PPKE.ITK.2015.006

where λ is the wavelength and f is the focal length of the focusing mirror. The same relationship holds for the other spatial dimension. Aside from the smallest resolvable feature, the size of the real image is also a key point. The number of pixels in V will equal the number of sample points. Therefore, the dimension of the real image (V_{dimX} or V_{dimY}) depends on the sensor pitch (d_s):

$$V_{dimX} = \Delta x \, U_{dimX}/d_s \, . \tag{2}$$

Thus, V_{dimX} gives the image size in meteres, whereas U_{dimX}/d_s shows the number of pixels along the "x axis". (If scanning consists of measurements at uniform grid points, then d_s can be smaller than the physical distance of the sensor pixels.)

1.1.3.2 *Holographic imaging*

By holographic imaging both the amplitude and phase of the radiation is registered by fixing the relative phase with the help of a reference beam. The path difference of the object and reference beam should be less than the coherence length of the source. By THz CW sources, the coherence length expands to 0.5 m giving freedom in the setup design.

By holographic imaging, there is no need for a convergent beam to perceive the image of the object. The interference pattern is enough to reconstruct the real image; therefore, imaging is possible without any optics.

1.2 Compressed sensing

The response time of the FET plasma wave detector falls into the nanosecond region, giving an equivalent 8-10 bit precision supposing a desktop mW range source and near real time operational speed [26]. These properties are competitive regarding other technologies and give grounds to apply compressed sensing (CS) [8] that proved its usefulness in several areas for instance image acquisition at short wavelengths [12], astronomy [27], and quantum state tomography [28] including the terahertz domain as well [29], [30]. However, any non-linear reconstruction algorithm could be used as a post-processing framework by dropping the acquisition speed from the performance criteria.

The L_0, L_1 and L_p norm of the vector $\boldsymbol{v}$ refer to the following three definitions throughout the work, respectively:

$$\|\boldsymbol{v}\|_0 = \{\#\text{ of } v_i\text{-s that are greater than } 0\} \tag{3}$$

$$\|\boldsymbol{v}\|_1 = \sum_{i=1}^{n} |v_i| \tag{4}$$

$$\|\boldsymbol{v}\|_p = \sqrt[p]{\sum_{i=1}^{n} v_i^p} \text{ for } p = 2, 3, 4, \ldots \tag{5}$$

DOI:10.15774/PPKE.ITK.2015.006

I note that the "L_0 *norm"* is not a true norm from the mathematical sense, as it does not fulfill all the axioms of a norm. The smoothed-L_0 norms utilize some function f – other than the absolute value – in order to make the problem treatable:

$$\|\boldsymbol{v}\|_{\boldsymbol{s0}} = \sum_{\boldsymbol{i=1}}^{\boldsymbol{n}} \boldsymbol{f}(\boldsymbol{v_i}) \tag{6}$$

The complex sampling is the inherent part of CS, where a discrete signal is represented as the multiplication:

$$\boldsymbol{y} = \boldsymbol{\Phi x} \tag{7}$$

where $\boldsymbol{\Phi}$ is an M by N special matrix, called the measurement matrix. It can be for instance a random matrix containing only binary values with equal distribution. $\boldsymbol{'x'}$ is the signal vector and $\mathbf{y}$ is the vector of measurements. In Figure 1, one can see a possible realization of such a measurement in a stylized form.

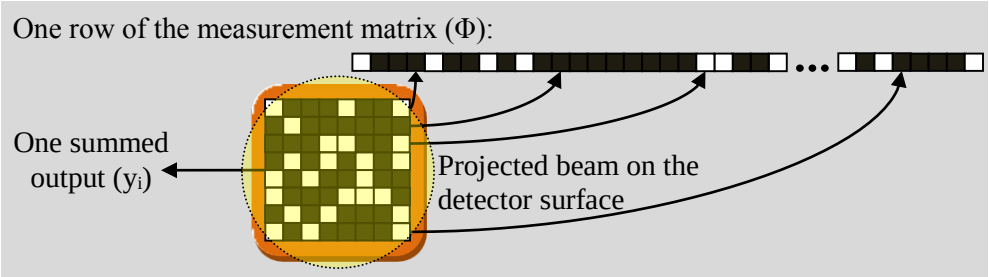

Figure 1 Stylized scheme of a complex measurement. A random pattern is set on a small detector array. The dark squares represent the active, 'ON' pixels that contribute to the summed response

The signal can be reconstructed, if a proper basis exists, in which the representation of the observed signal is sparse:

$$\boldsymbol{\Psi a} = \boldsymbol{x}\,. \tag{8}$$

Here Ψ is the matrix of the special basis and a is the sparse representation of the signal x. Exploiting this extra information one can minimize according to the l_0 norm, that is finding an a vector with the most zero components. Substituting (8) into (7), the problem formulated as:

$$\boldsymbol{a}^* = \mathbf{arg}\,\mathbf{min}_{\boldsymbol{a}} \|\boldsymbol{a}\|_{\mathbf{0}} \text{ such that } \boldsymbol{\Phi\,\Psi a} = \boldsymbol{y}\,. \tag{9}$$

To solve the combinatorial problem above is too hard, for greater sizes (N>1000) it is actually hopeless. However, a few seminal works proved that exact reconstruction can be ensured easily in the L_1 norm as well:

$$\boldsymbol{a}^* = \mathbf{arg}\,\mathbf{min}_{\boldsymbol{a}} \|\boldsymbol{a}\|_{\mathbf{1}} \text{ such that } \boldsymbol{\Phi\,\Psi a} = \boldsymbol{y}\,. \tag{10}$$

This problem is much easier to solve, because it fits into the framework of convex optimization. Thus, a rigorous mathematical background emerged due to its practical impact. There are several

DOI:10.15774/PPKE.ITK.2015.006

algorithms available to solve efficiently this problem. For instance, the 'state of the art' basis pursuit (BP), the orthogonal matching pursuit (OMP) or the basis pursuit denoising (BPDN) algorithm are of this kind.

Many L_1 optimization tool utilizes the L_2 solution for an initial guess that is the least-squares solution of the problem and comes down to multiplication with the pseudo-inverse ($\left(\mathbf{A}^{\mathrm{T}}\mathbf{A}\right)^{-1}\mathbf{A}^{\mathrm{T}}$, where $\mathbf{A} = \boldsymbol{\Phi}\,\boldsymbol{\Psi}$).

In the more important noisy case the measurements are corrupted with noise and (10) is relaxed:

$$\boldsymbol{\Phi}\mathbf{x} + \boldsymbol{\eta} = \mathbf{y} \tag{11}$$

$$\boldsymbol{a}^* = \mathbf{arg}\,\mathbf{min}_{\boldsymbol{a}}\|\boldsymbol{a}\|_1 \text{ such that } \|\boldsymbol{\Phi}\,\boldsymbol{\Psi}\boldsymbol{a} - \boldsymbol{y}\|_2 < b\,, \tag{12}$$

where b is the allowed deviation of the projected candidate solution from the measurements. The problem unites two goals in itself, the sparsity and the

We call the signal k-sparse if a^* has only k number of non-zero elements. However, this notion has practically no importance, because in a real-word problem all components have at least small non-zero values. Therefore, it is customary to assume that the rest N-k number of elements are less than a given ε. However, often, a power law is required for the proofs: the signal $\boldsymbol{x}$ is 'p-compressible' with amplitude R, if the following condition holds at any $p \in (0,1)$.

$$|\boldsymbol{x}|_{\boldsymbol{i}} < \boldsymbol{R}\,\boldsymbol{i}^{-\frac{\mathbf{1}}{\boldsymbol{p}}} \tag{13}$$

However, k-sparse vectors approximate 'k-compressible' signals quite good [31]:

$$|\boldsymbol{x} - \boldsymbol{x_k}|_{\mathbf{1}} < \boldsymbol{C_p}\cdot\boldsymbol{R}\cdot\boldsymbol{k}^{\mathbf{1}-\frac{\mathbf{1}}{\boldsymbol{p}}} \tag{14}$$

$$|\boldsymbol{x} - \boldsymbol{x_k}|_{\mathbf{2}} < \boldsymbol{D_p}\cdot\boldsymbol{R}\cdot\boldsymbol{k}^{\mathbf{0.5}-\frac{\mathbf{1}}{\boldsymbol{p}}} \tag{15}$$

where, $\boldsymbol{x}$ is the p-compressible signal and x_k is its k-sparse variant having non-zero elements only at the k largest components of $\boldsymbol{x}$. C_p and D_p ·are both constants depending on p.

To calculate the original signal from the sparse reconstructions we have several options; Needle gives a comprehensive survey of the available algorithms in [31] as of 2010, whereas [32] gives a recent insight to the topic concentrating on impulsive noise. Here, I summarize the basic notions behind the regularized reconstruction methods.

Candes [16] gave a universal condition for $\boldsymbol{\phi}$ with which one can ensure exact reconstruction of the signal with high probability in the form of the restricted isometry property (RIP). The measurement matrix ($\boldsymbol{\phi}$) satisfies the r-RIP, if there exist a $\delta_r > 0$, such that:

$$(1-\delta_r)\|\boldsymbol{x}\|_2^2 \le \|\boldsymbol{\phi}\boldsymbol{x}\|_2^2 \le (1+\delta_r)\|\boldsymbol{x}\|_2^2, \text{ for all } x \text{ that fulfills } \|\boldsymbol{x}\|_0 \le \boldsymbol{r} \tag{16}$$

where, the least δ_r is the so called r-th restricted isometry constant.

DOI:10.15774/PPKE.ITK.2015.006

The L_1 based convex optimization methods have guaranteed, optimal reconstruction error on *s*-sparse signals, assuming that the following – most recent – condition hold for the *2s*-th RIP constant (δ_{2s}) of their measurement matrix:

$$\delta_{2s} \leq 0.4652 \tag{17}$$

Interior point variants succeeding within $O(N^{1.5}M^2)$ time. If the vector is *s*-sparse, then the reconstruction of the L_1-norm based optimizations is optimal. This means that not only the error, but also the needed number of samples is minimal. Hence, the RIP condition is an elegant and powerful tool to ensure the quality of reconstruction. However, it needs $O(2^N)$ time to determine the RIP constant that involves the calculation of the greatest singular value of all *r*-column submatrices of $\boldsymbol{\Phi}$ (NP-hard problem). Therefore, the following general results help much the application of RIP.

Gaussian or Bernoulli random measurement matrices – having elements from i.i.d. Gaussian random variables or from uniformly distributed ± 1 values – have a *2k*-RIP constant: $\delta_{2k} < \epsilon$, if the number of samples fulfills the following condition [33]:

$$\mathbf{M} \geq \frac{\mathbf{s} \cdot \mathbf{log}\left(\frac{\mathbf{N}}{\mathbf{s}}\right)}{\boldsymbol{\epsilon}^{\mathbf{2}}} \tag{18}$$

For subsampled Fourier matrices, the bound is higher having a component raised to a low power ($log^5(.)$). The conjecture is $M = O(s \cdot \log(N))$ measurements are enough to have an exact reconstruction with high probability. (I note the used expression "high probability" is not corresponds to the exact mathematical definition; for the noiseless case the probability is even higher (overwhelming probability); however, due to the small practical importance of the noiseless case I do not give more detailed description of that – see the essential works of Candes, Tao [18] and Donoho [8] for that.)

These methods are robust and uniform, meaning they have guaranteed error on noisy, non-sparse signals as well and they work with a single measurement matrix on arbitrary inputs.

There are several different algorithms that solve this convex optimization problem. The best inner point methods succeed within $O(M^2*N^{1.5})$ running time.

Iterative greedy methods like the orthogonal matching pursuit (OMP) are faster, but most of them have greater guaranteed error and they may need more number of samples.

The compressed sampling matching pursuit (CoSaMP) algorithm and their variations give an optimal solution to the L_1 problem – (10) and (12) – considering guaranteed minimal error, minimal number of samples, stability, uniformity and computation speed [34] [31].

Even faster algorithms are available (sublinear in the signal vector), however they need highly structured measurement matrices and a bit more number of measurements (Fourier sampling, HSS pursuit).

DOI:10.15774/PPKE.ITK.2015.006

I tried out the state-of-the-art algorithms and used the BP, CoSaMP and a fast alternating projection method based on smoothed zero norm functions [35] [36]. According to my experience, the different algorithms produced images of similar quality in this application setting. (The squared error showed slight differences depending on the size, the content and the noise of the images and especially on the sensor noise – that is the total error of data acquisition.)

1.2.1.1 Complex sampling

I use the expression 'complex sampling' as the capability to perform a somehow aggregated sampling that results in appropriate data for a non-linear reconstruction complying with the above mentioned notation (equation 7 and 8). Thus, the concept relies on the basic measurement and reconstruction scheme of compressed sensing, but covers any non-linear reconstruction mechanism e.g. it is not restricted to the $M < N$ case.

1.3 Related work in the application of CS

1.3.1 SLMs in the THz domain

The spatial light modulator (SLM) based compressed sensing cameras promise the fast acquisition of large fields of view at high SNR within the THz domain as they can omit the slowly raster scanning of single pixel confocal setups. The first experiments were carried out with mechanical masks changed manually or fixed on rotating disks. In the recent years, electronic and optically controlled metamaterials emerged that can form the core of the SLM. At the beginning, the optically controlled THz SLMs relied on a digital micro mirror device (DMD). Here, the DMD controls an expanded laser beam that goes through a high resistivity silicon (ρ-Si) wafer simultaneously with the THz beam. With enough optical power, the photo excited electron plasma changes the transmittance characteristic of the ρ-Si wafer significantly. More developed solutions improve on the modulation depth with a metamaterial structure whose frequency characteristics (transmittance peaks) can be shifted with photo excited electrons in the underlying ρ-Si wafer [20]. This configuration achieved 64-1000 pixel resolution at 0.5 Hz and has about 67 % modulation depth with 10-15 % loss and a SNR greater than 100. The moving mechanical components limits the modulation frequency to a theoretical maximum of 20 kHz, however, the lock-in needs about 5 ms to settle in the actual design.

Full solid-state, electronic SLMs reduce the complexity of the setup by eliminating the need for any moving parts. Liquid crystals (LC) are proper birefringent materials whose refractive index can be changed with biasing. [13] and [21] shows such setups, demonstrating a 6 by 6 pixel and an 8 by 8 pixel reflective SLM, respectively. Their modulation depth is over 75 %, however, there are still severe shortcomings of the technique. First, the losses are high: by the actual liquid crystal covered metamaterial, the loss is more than 70 % at the highest modulation depth. Second, the technology is not matured yet, the manufacturing process includes several costly

DOI:10.15774/PPKE.ITK.2015.006

steps, and the resistivity of the LC compound should be properly controlled (avoiding ion trapping at the surfaces).

1.3.2 CS capable focal plane arrays for viewable light

Robucci et. al gave a 65 kpixel CS capable CMOS solution for short wavelengths [9]. This imager performs the complex sampling via the small pixel blocks of 8 units connected in parallel and a separate set of analog multipliers. With this, the IC generates 8 samples from every single measurement, however, the sampling consists an additional analog operation. The advantage of the array is the potential increase of the speed and the reduction of the power consumption according to [9].

DOI:10.15774/PPKE.ITK.2015.006

2 THE RESEARCH PROJECT

2.1 Aims of the project

The goal of the research project was to develop sensor arrays based on standard CMOS technology that make possible room temperature terahertz imaging for diagnostic applications. For this reason, we contacted with the Department of Dermatology, Dermatooncology and Venerology of the Faculty of Medicine at the Semmelweis University. The needed device specification for skin cancer diagnostics was determined with the help of the clinical professionals there. The obtained data regarding an in-vivo measurement is summarized in Table 1.

Min. lateral resolution	100 μm
Min. axial resolution	10 μm
Min. depth of sensing in human tissue	1 mm
Max. acquisition time	1-3 min.
Min. field of view	1.5 × 1.5 cm
Min. water content detectability	< 1 %
Measurement positioning	flexible (arbitrary point of the body)
Cancer indicator features	water content, spectral pattern, …
Min. diagnostic sensitivity rate of a system	> 99 % (this is the level of a human professional)
Min. diagnostic specificity rate of a system	> 85 % (avg. human is between 51-85 %)

Table 1 Rough requirements of a possible diagnostic device

The targeted lateral resolution (< λ) can be achieved only with super resolution techniques or at a considerably higher frequency (3 THz instead of 460 GHz). The field of view is large (22.5 kpixel with the given lateral resolution), although the diffraction limit reasons only about 534 pixels at 460 GHz.

To calculate an approximate irradiance showing up at the detector I used the following simple formula and assumed a homogeneous medium.

$$I = I_{incident} e^{-\alpha z} \left[\frac{W}{m^2}\right], \tag{19}$$

where α is the absorption coefficient and z is the traveled distance within the medium. 'α' varies on a wide range, however, as water absorbs high frequencies, all the wet environments have significantly large absorption coefficient:

- in air at 52 % humidity α is about 0.1 m^{-1} at 0.5-1 THz (except an absorption peak at 0.55 THz)
- in water α is around 145-240 cm^{-1} (0.1-1 THz)
- in biological tissues α can be approximated to be between 100-200 cm^{-1}

DOI:10.15774/PPKE.ITK.2015.006

- in adipose tissue it is only between 25-125 cm^{-1} (that is why the technology already successful in breast cancer diagnosis)

Figure 2 and Figure 3 give a more comprehensive notion about the absorption coefficient in the form of simplified sketches. These figures show only trends and omit the various absorption peaks.

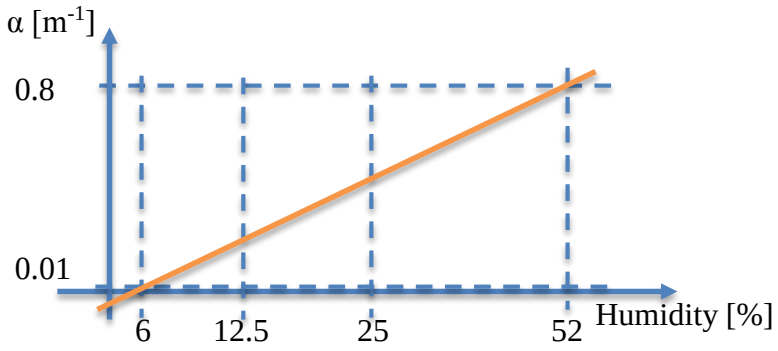

Figure 2 Sketch of the absorption coefficient of air at 1.5 THz

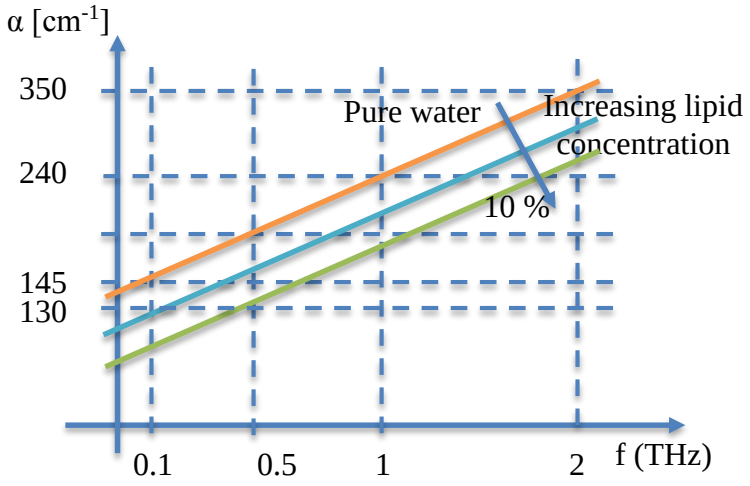

Figure 3 Sketch of the simplified absorption spectrum of water and water-lipid solutions

Of course, the diffraction can also seriously affect the total attenuation, but it has smaller significance on the millimeter scale traveling paths. Additionally, diffraction depends much on the actual structure of the specimen.

Here, I give the needed SNR and detectability to meet the specification with the actual setup at the COSPL. Because of the required minimum water content detectability of 1 %, there is demand for at least 1:100 signal-to-noise ratio that is 40 dB SNR. 1 mm depth means 2 mm travel length (the incident plus the reflected path). For this, the irradiance can be calculated in the following way in a homogeneous medium: $I = I_{incident} \cdot e^{-200 \cdot 0.2} \approx I_{incident} \cdot 4.24 \cdot$

DOI:10.15774/PPKE.ITK.2015.006

$10^{-18}\ \left[\frac{\mathrm{W}}{\mathrm{m}^2}\right]$ (at $\alpha = 200\ \mathrm{cm}^{-1}$) and for 0.5 mm depth it is $\mathrm{I} \approx \mathrm{I}_{\mathrm{incident}} \cdot 2 \cdot 10^{-9}\ \left[\frac{\mathrm{W}}{\mathrm{m}^2}\right]$ (at $\alpha = 200\ \mathrm{cm}^{-1}$).

If I approximate the obtainable SNR (not given in dB) in the following way with the noise floor that is the limit of sensitivity:

$$SNR \approx \frac{\mathrm{I \cdot A}}{\mathrm{P_{noise\ floor}}}, \text{ then} \tag{20}$$

$$\mathrm{P_{noise\ floor}} \approx \frac{\mathrm{I \cdot A}}{\mathrm{SNR}} \approx \frac{\mathrm{P_{source} \cdot 4.24 \cdot 10^{-18}}}{100} = 4.24 \cdot 10^{-20} \cdot \mathrm{P_{source}}\ [\mathrm{W}], \tag{21}$$

where "I" is the irradiance and "A" stands for the area of the detector. (For simplicity, I assume perfect focusing to the detector, that is $\mathrm{I_{incident}} \cdot \mathrm{A} = \mathrm{P_{source}}$). (21) shows how strong illumination would be needed to achieve these goals with a noise floor in the pW range, what we can get from the noise equivalent power (NEP):

$$\mathrm{NEP_{system}} \approx \frac{\mathrm{P_{noise\ floor}}}{\sqrt{\mathrm{B}}}\ \left[\frac{\mathrm{W}}{\sqrt{\mathrm{Hz}}}\right], \tag{22}$$

where "B" is the bandwidth of the system. It is obvious that this implies infeasible system NEP values even at good frequency filtering regarding the available source power of ~100 μW. Such depth is achievable only with high power sources, heterodyne detection and efficient frequency filtering.

However, the 1 mm depth can be achievable in other tissues with lower absorption coefficient and sensing is still possible at about 0.25 mm depth in biological tissues assuming a minimum NEP of $20\,\frac{\mathrm{pW}}{\sqrt{\mathrm{Hz}}}$, 10 Hz bandwidth, ensured by the lock-in amplifier and a minmum required SNR of 100:

$$z = \frac{1}{2}\frac{1}{\alpha}\ln\left(\frac{\mathrm{I_{incident}}}{\mathrm{I_{min}}}\right) = \frac{1}{400}\ln\left(\frac{\frac{\mathrm{P_{source}}}{A}}{\frac{\mathrm{P_{noise\ floor}}}{\mathrm{A}} \cdot \mathrm{SNR}}\right) = \frac{1}{400}\ln\left(\frac{100 \cdot 10^{-6}}{\sqrt{10} \cdot 20 \cdot 10^{-12} \cdot 100}\right) \approx 241\ [\mu\mathrm{m}] \tag{23}$$

See more considerations on the depth of sensing in section 3.4.3.

I conclude the main bottleneck of applicability is the limited SNR of the sensor. Sensitivity has to be improved in order to increase the depth of examination and the acquisition speed. Moreover, fulfilling the specification of lateral resolution may require silicon immersive lenses or super-resolution techniques.

Today THz FPAs are still far from their theoretical NEP values. The performance of the integrated systems within real application scenarios are often far from the reported best achievable NEP values of the devices [7]. Therefore, it is an important task to study the FPA architectures to help designers improve on system noise particularly for heterodyne detection, where the incoming signal mixes with the signal of a much stronger local oscillator (~10 μW) inside the channel improving the sensitivity several orders of magnitude.

DOI:10.15774/PPKE.ITK.2015.006

However, with high power sources (W-mW range) imaging at discrete frequencies is already possible in the 0.08-0.2 THz frequency range (see the IMPATT diode powered simple camera systems of TeraSense). The versatility of these low frequency setups imply the future power of imaging in the 0.2-1.5 THz range and motivates the work of the terahertz research group at the COSPL.

Water content measurements can be seen in Section 4.1.1, but Section 4 contains other related experiments as well.

2.2 The goals of my research work - problems to solve

The focus of my work was to study the compressed sensing based THz detectors and their forms of application. This served the ultimate goal of promoting the application of our FET based detectors in the field of THz diagnostics. This emerging research direction raises many basic problems. I list here a few big areas out of which I touched several ones during my work:

- Determine the specification of the sensor array
- Acquisition speed
- Weak signals, low SNR, high noise, small response, low penetration depth
- Low resolution (spatial), low NA optics
- Small pixel number
- Low quality images, low sensitivity, low contrast
- Scanning problem (time, accuracy)
- Low specificity at sub THz frequencies

2.3 Setup

2.3.1 Source

An yttrium iron garnet (YIG) base oscillator – tunable from 9.5 GHz to 14 GHz – powers the source of the quasi-optical setup that is a semiconductor based amplifier-multiplier chain (AMC). The AMC multiplies the base frequency with a factor of nine providing approximately 14 dBm (~0.25 W) typical output power in the frequency range of 82.5-125 GHz. The output of the AMC is a waveguide and a horn antenna couples the power to the air.

However, additional multipliers may connect to the output to cover higher frequency ranges with decreasing efficiency. Table 2 summarizes the technical data of the different configurations. These are the typical technical parameters of the setup from the datasheets; the measured output power at 460 GHz was 102 μW.

DOI:10.15774/PPKE.ITK.2015.006

Head	Mult. factor	Configuration	Typical power	Frequency range
WR9.0	9	WR9.0AMC	+ 14 dBm	82.5-125 GHz
WR4.3	18	WR9.0AMC + WR4.3X2	+ 3 dBm	170-250 GHz
WR2.8	27	WR9.0AMC + WR2.8X3	-1 dBm	250-375 GHz
WR2.2	36	WR9.0AMC + WR4.3X2 + WR2.2X2	-10 dBm	340-500 GHz
WR1.5	54	WR9.0AMC + WR4.3X2 + WR1.5X3	-21 dBm	550-750 GHz

Table 2 The characteristics of source configurations

In Figure 4 one can see the output characteristics of the WR2.2 multiplier head. Due to the waveguide-based structure, the spectrum has high variance with many narrow peaks.

The theoretical accuracy of the frequency tuning is on the order of 7 MHz, however any noise of the system deteriorates it. Aside from this, the YIG seems to have relatively high offset error that decreases the absolute precision of the source. Hence, by recording spectral features one has to sweep at higher frequency resolution than the targeted one and average several correlated spectra. This way one can create data appropriate for comparison.

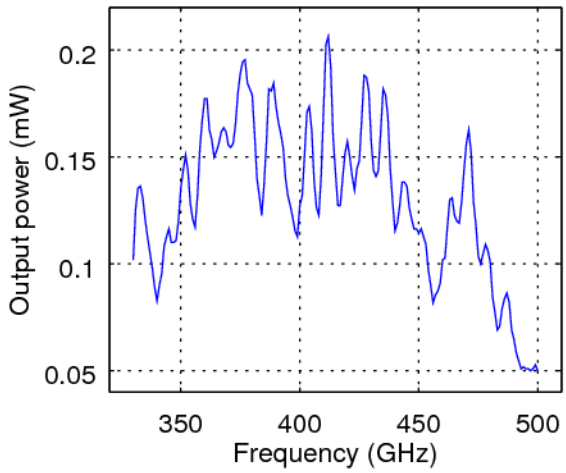

Figure 4 Power spectrum of the utilized terahertz source

The coherence length is around 0.5 m that means great freedom in holographic recordings considering the object and reference path difference, but rises severe technical problems by making the system very sensitive to any physical effects due to self-interference. This means that sub-millimeter (< 100 μm) changes of the optical path can cause over 50% changes in the recorded intensity. This issue makes in-vivo measurements a hard task, where the precise positioning of the body parts for at least tens of seconds is challenging. However, we had problems with in-vitro measurements as well, when solutions of different temperature were investigated: the thermal expansion of the plastic sample holder caused significant discrepancies. Diffusor plates could partially circumvent the problem of high coherence at the cost of decreasing the source intensity.

DOI:10.15774/PPKE.ITK.2015.006

2.3.2 Quasi optical setups

Quasi-optical setups may consists of parabolic mirrors, plastic lenses and beam splitters. Figure 5 presents the schematics of the imaging setups for CS measurements.

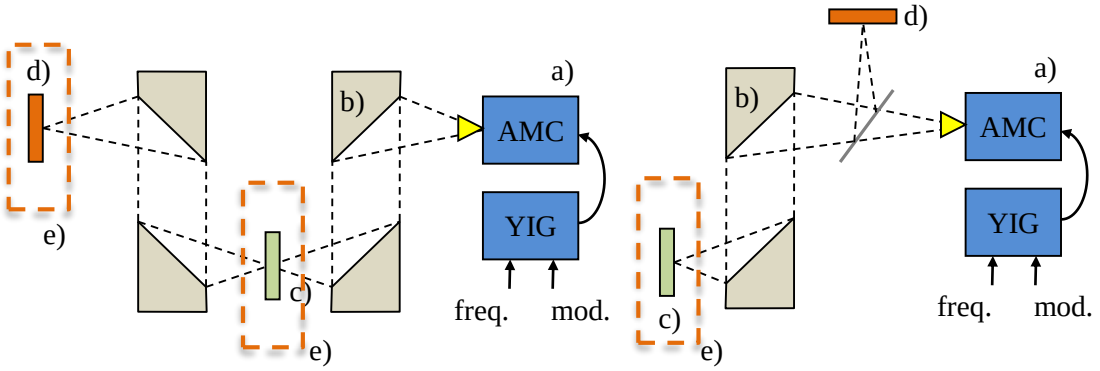

Figure 5 A transmissive and a reflective setup is depicted on the left and right side, respectively; the main components are: a) Terahertz continuous wave (CW) source: amplifier-multiplier chain (AMC) and yttrium iron garnet (YIG) oscillator, b) off-axis parabolic mirrors, c) target object d) detector chip e) 3 axis moving stage

The calculation of the sensor and image position is straightforward. For the real image, I used the mirror equation:

$$\frac{1}{f} = \frac{1}{d_I} + \frac{1}{d_O}, \tag{24}$$

where d_I and d_O means the distance of the object and that of the image, respectively. Figure 6 gives an overview about the basic configurations and helps to compare them.

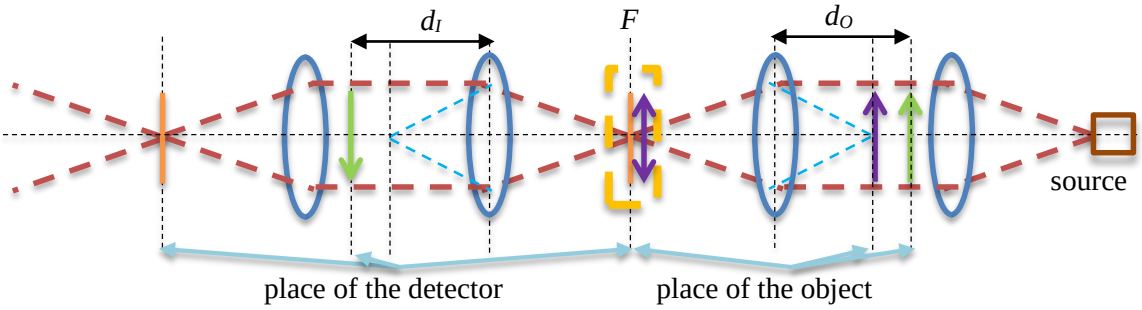

Figure 6 The basic image projection methods: a) real image with magnification ratio, $M = -d_I/d_O$ (green), b) confocal scanning (orange), c) Fourier imaging; the image is also right in the focal plane (purple); lenses are interchangeable with parabolic mirrors; the distances are not proportional

In the case a), the distances are not proportional in the figure, of course, when $f < d_O < 2f$, then $2f < d_I$.

To measure the resolution of the system in confocal scanning configuration and all pixel activated, I fixed the actual chip on a high precision, 3 axes moving stage. The parabolic mirrors

DOI:10.15774/PPKE.ITK.2015.006

collimated and focused the source beam onto the detector array. The Gaussian like spatial intensity distribution was registered with 100µm precision and presented in Figure 7.

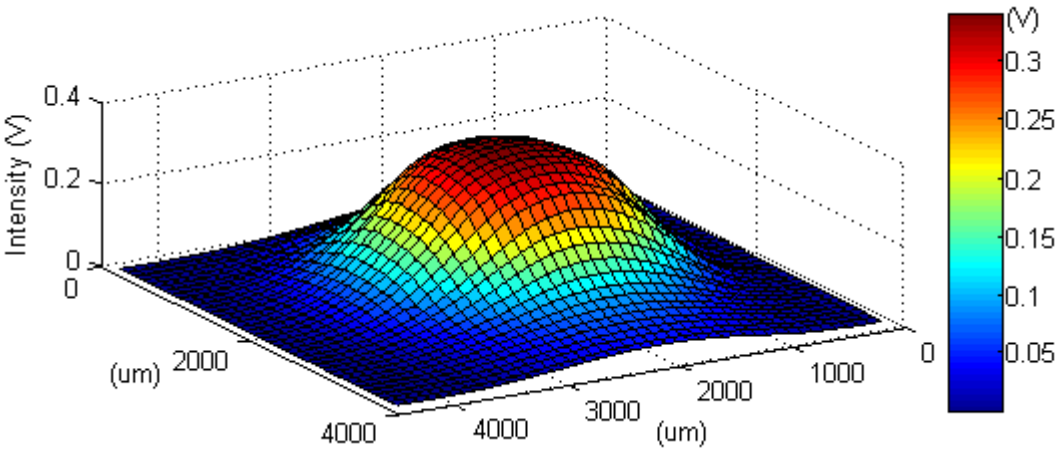

Figure 7 Raw measurement data of the focused Gaussian beam of the terahertz source

2.3.3 Antenna coupled FET detectors

2.3.3.1 Principle of detection

Here, I summarize the principle of FET based sensing and highlight some problems of such detector arrays. These gave additional motivation to make complementary architectural investigations.

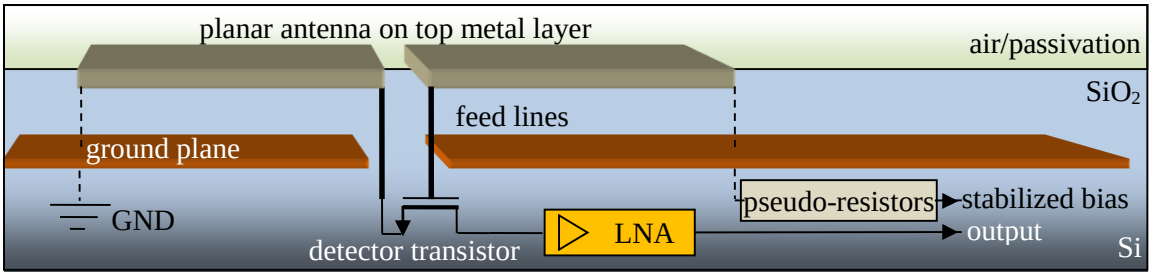

Figure 8 The scheme of a Si MOS based terahertz sensor element

In the followings I mean on 'terahertz sensing' power intensity measurements in the 125-750 GHz frequency range. Figure 8 shows the scheme of a single detector element, where detection is realized in the channel of an nMOS transistor. The high frequency signal of the antenna arrives to the transistor pads. The free electrons behave similarly as a gas or shallow water [23] under the gate, because plasma waves obey linear dispersion laws ($\omega = sk$), where ω, s, k denotes the frequency, the wave velocity and the wave vector, respectively. The velocity, $s = \left(\frac{Ue}{m}\right)^{1/2}$, where e and m is the charge and mass of the electron, in turn, U is the gate to channel voltage. Therefore, the Euler equations describe the excitation of the two-dimensional electron gas (2DEG) by small amplitude AC signal. The channel has a Reynolds number around 60

DOI:10.15774/PPKE.ITK.2015.006

(regarding HEMTs) as a cavity of the "fluid". Due to the nonlinearities of the plasma and the boundary conditions, a DC voltage emerges in the active zone of the channel. This is the "intrinsical" response of the device that is measured through the terminals, presenting a given load to the detector. The loading (or change in the boundary conditions) alters the intrinsical response. In the same time, the transistor works as a common gate amplifier according to the biasing conditions. Therefore, the measured, in-circuit response of the detector depends on the connectings of the antennas, the load and the biasing (among other factors) on a complex way [6].

Noise is another issue that changes on a different way, therefore minimum NEP and maximum response do not coincide.

2.3.3.2 Antenna design

The chief designer, Péter Földesy considered three main types of antenna arrangement for realization:

I. Aperture coupled variants:
   a) Chip on board (signal comes from the back through the substrate)
   b) Chip with covering (signal comes from the top)
   c) Chip with suspended covering (optionally with Fresnel aperture)

II. Planar antenna laying directly in the top metal layer of the chip
   a) Patch antenna
      1. Patch with striped, grid structure (to reduce capacitive losses)
   b) Fresnel aperture antenna

III. Flip –chip –like arrangement with isolating layer – its feasibility is questionable, however this way the distance of the patch and the chip surface could be tuned accurately with the thickness of the isolating layer.

These findings were shown to microwave communication specialists (Gergely Károlyi and Csaba Füzy) for performance comparison estimation. In the followings, I depict the schematics of the different antenna types to reveal the main difficulties of integration (See Fig. 9-13 for details; these are modified, extended versions of figures from [24].). I mention only the two most important problems: which antenna structure can be the most efficient and how to realize the feedline to minimize losses i.e. how to match the antenna to the detector. In the case of aperture coupled realizations the electromagnetic field couples through an aperture – practically a slot in a metal layer – to a planar feedline. This line is a simple metal wire of about 15 μm width with a closing stub at its ends. This stub is an overhang of the wire starting from the geometrical center of the aperture that takes place a few layers above the feedline what lays generally on the first metal layer.

DOI:10.15774/PPKE.ITK.2015.006

With this, the closing of the feedline can be tuned easily and accurately. Matching of the patch to the detector is only the question of proper distances between the feedline, the aperture, and the patch antenna. However, the distance of the aperture to the feedline can be set only in discrete steps of the metal layers within a very small range relative to the wavelength. The fixing of the patch is another problem. It needs a solid supporting surface that can be metalized. The space holder can be this carrier material itself or some auxiliary support structure (suspended covering). Here, the distance can be set more freely, but the fixing, accurate manufacturing and positioning of the patches is a hard and costly post-processing task. These facts make the variations in group I. and III. disadvantageous from feasibility point of view.

The direct planar antennas are easier to manufacture, however one have to be more cautious during design. For acceptable matching, one has to estimate the input impedance of the detector transistor at frequencies that are above the cut off frequency of the technology and not covered by the conventional channel models.

To steer clear of this problem, that could be solved precisely only with iterative design-manufacture-measure steps, we used the design strategy suggested by Csaba Füzy. According to this, we took the MOS transistor with near threshold gate bias as it was an open circuit from the GS and GD points, where G, S, D are the gate, source, drain contact points, respectively. Each of us simulated the antenna structures with its feedline and the transistor contacts. The antenna design and characterization was not carried out with the conventional antenna design methods. In that scheme a proper port configuration, often frequency domain simulation and S-parameters calculation takes place. Then the S-parameters are used as the key figure of merit. In the investigated system, however, the design was driven by the maximal field strength between the transistor contacts.

For this reason, the via stacks that constitute the feedline were not pure vertical columns, but they formed a V-shape approaching gradually the two contact point of the transistor from the opposite sites.

Details with schematics about the antenna connecting can be seen later in chapter 2.4.1.2.

DOI:10.15774/PPKE.ITK.2015.006

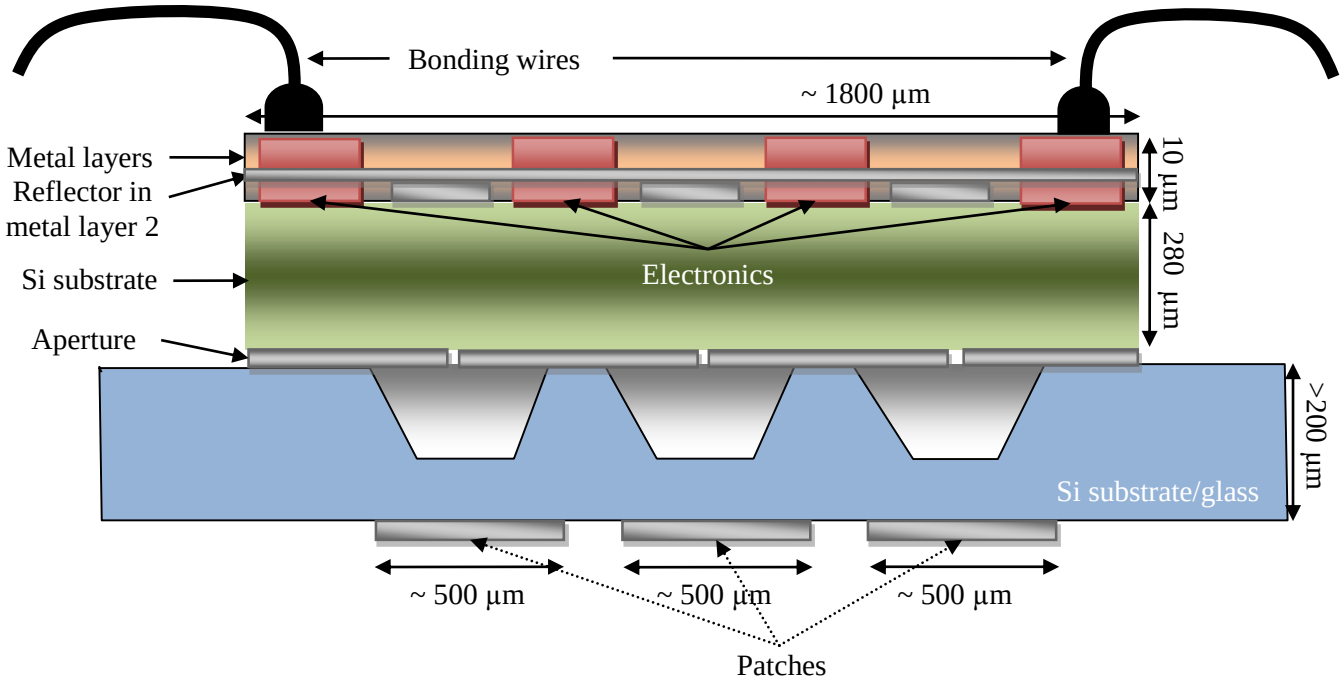

Figure 9 The schema of version I. a) chip on board with reflector.

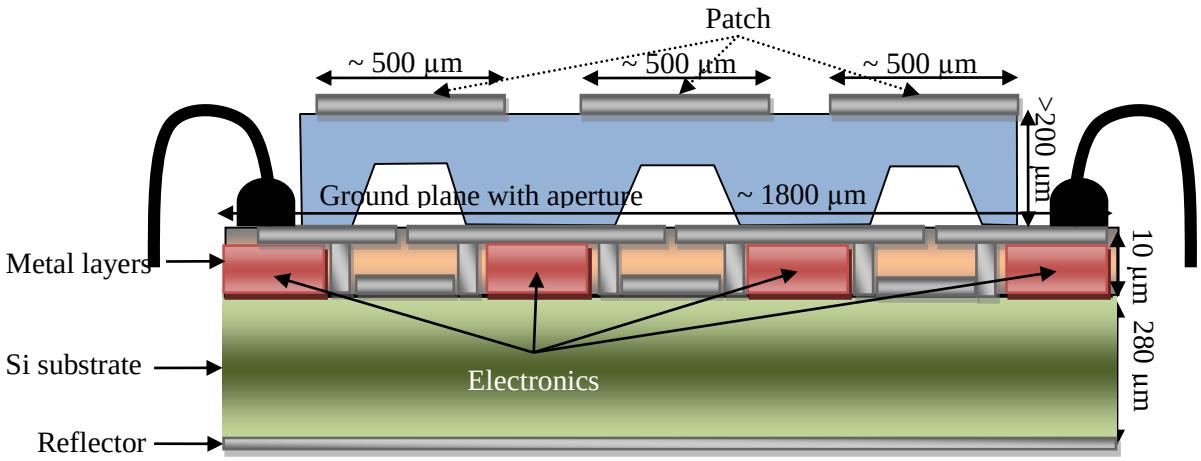

Figure 10 The schema of version I. b) chip with aperture coupled antennas and a covering with patch antennas and optional etched cavities for reducing dielectric losses.

DOI:10.15774/PPKE.ITK.2015.006

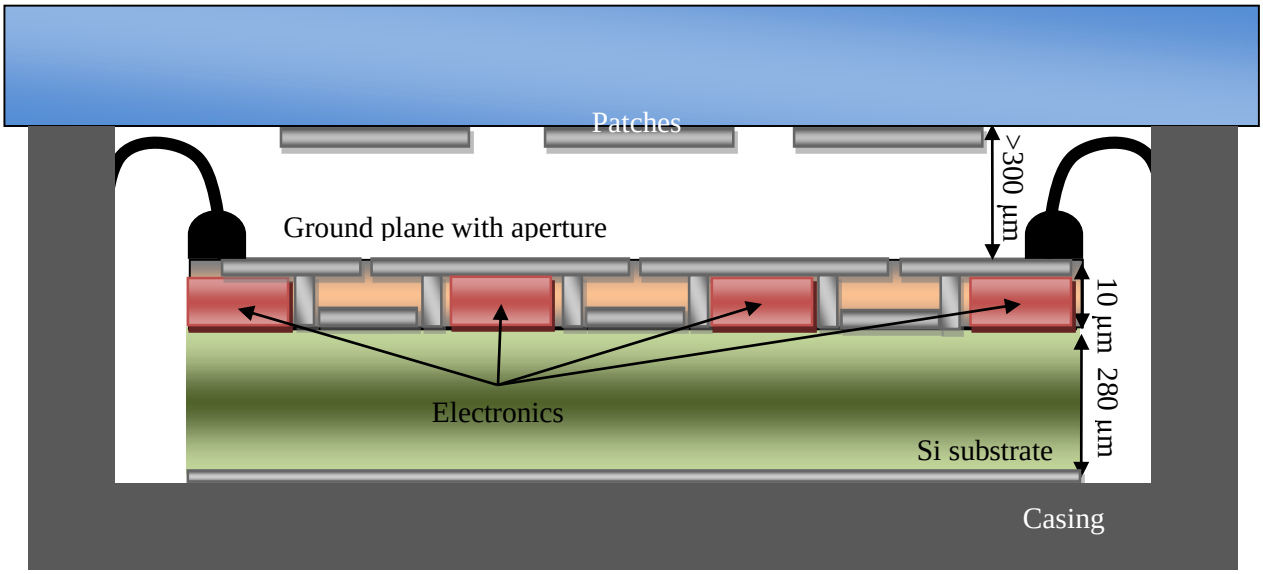

Figure 11 The schema of version I. c) chip with suspended covering. It can be combined with aperture coupled antennas or simple planar structures.

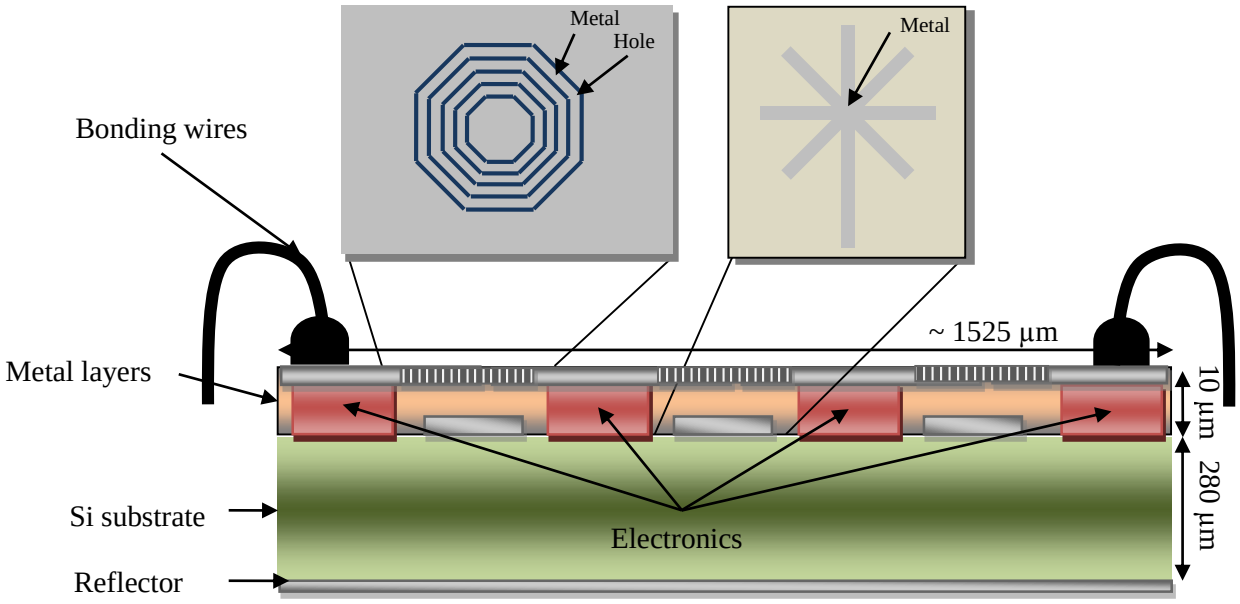

Figure 12 The schema of version II. b) The schematics of a more sophisticated aperture coupled antenna with polarization insensitive Fresnel aperture (without ordinary patch). In the case of version II. a), there is a simple or striped patch on the top and feed lines are formed from via stacks (see later in details).

DOI:10.15774/PPKE.ITK.2015.006

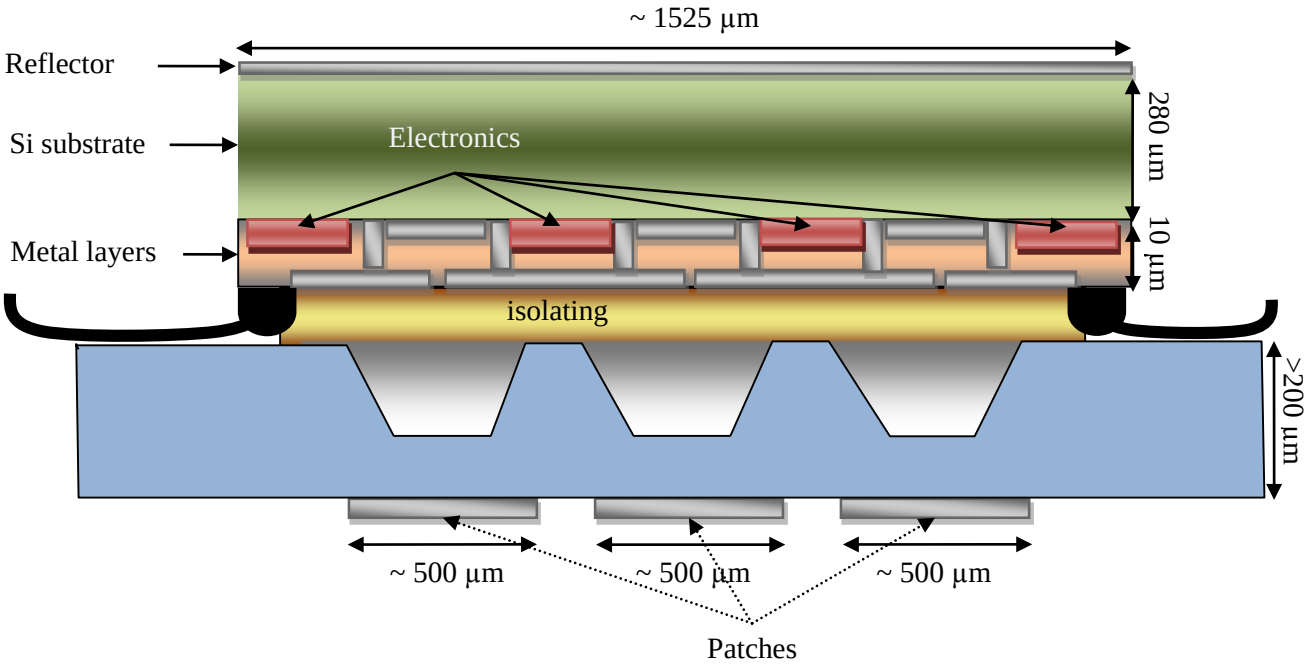

Figure 13 Version III. Flip-chip-like configuration with an isolating layer.

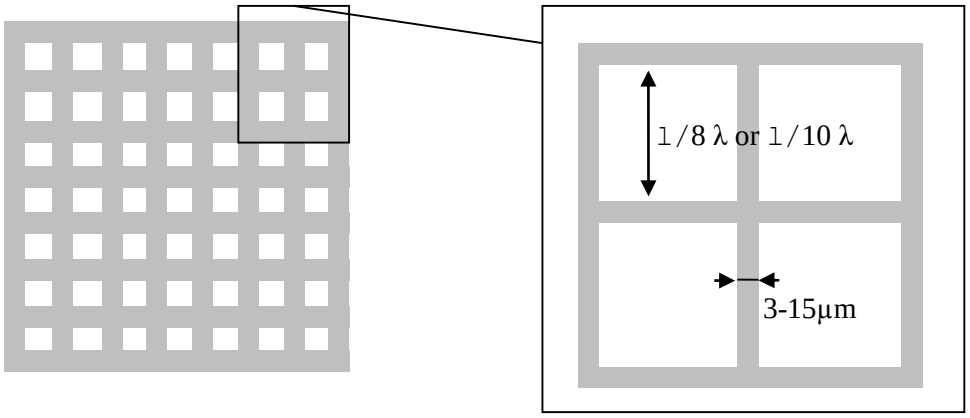

Figure 14 The envisioned striped, grid-like structure of the patches

I have considered several antenna types within the main categories. For instance, the striped patch antenna (see Figure 14). Patch antennas are broadband, simple to design and easy to manufacture. Their capacitive losses can be reduced if the patch has a grid like structure. If polarization sensitivity is not a problem that is only one receiving direction is used, stripes in only that single direction (no intermediate crossing) or clustered dipole structures can be more advantageous. Yet, it provides the possibility for heterogeneous detection. However, one has to keep in mind the manufacturing antenna rules (this notion is not related to the antenna design) and metallization restrictions during the design.

I have simulated special variants of quad antennas as well as possible compact and high gain solutions. These, antennas were generated by scripts and were easy to modify and optimize them on automated ways.

DOI:10.15774/PPKE.ITK.2015.006

2.3.3.3 Manufactured chips - premises

The first antenna coupled detector – made at the Intstitute for Computer Science and Constrol of the Hungarian Academy of Sciences (ICSC – HAS) by Földesy [12] – was a proof-of-concept chip manufactured at 180 nm feature size technology with photoconductive antennas on it. Several detector-antenna connectings and antenna types were tested, but the simplest arrangements provided the highest responsivity; these were used in the later designs.

A 90 nm SoC like monolithic detector array meant the second step, where both single-band and broadband antennas showed up with linear and circular polarization sensitivity. These designs paved the way for a compressed sensing based detector array. Péter Földesy proposed the idea that complex sampling capable THz detectors can be formed from serially connected arrays with individually controllable gate biases. I could also participate in the process and performed the sizing of the antennas according to the methodology determined by our RF experts. I used this chip as a starting point for my investigations and to validate the results with measurements.

2.3.1 A/D conversion

The A/D conversion must be an integrated part of a compact imager; however, experimental use and the need for easier prototyping may waive this requirement. Despite the COSPL had such an SoC-like design, in the experiments we used a commercial external data acquisition card (NI6343) to digitalize the output of the integrated LNA.

The absolute accuracy is usually much lower than that of the pure random noise would allow: AbsoluteAccuracy = Reading (GainError) + Range (OffsetError) + NoiseUncertainty.

This NI DAQ card had an absolute accuracy of 2190 µV, 1130 µV and 240 µV in the (-10 V, 10 V), (-5 V, 5 V) and (-1 V, 1 V) operating range, respectively – concerning only the applicable opportunities. The belonging RMS random noise (σ) was 270 µV, 135 µV and 28 µV, respectively that resulted in a noise uncertainty of 5.7 µV, 2.86 µV and 0.59 µV with 3σ coverage and 20000 samples. In the first two case, the given 16 bit precision (301 µV and 150 µV) is above the limit of the absolute accuracy, however, for the highest absolute precision (30 µV) at least 640 kSamples would be needed at maximal, 1 V readings. After all, the used lock-in amplification relied only on the relative accuracy of the A/D. In a typical operation configuration – (-5 V, 5 V) range, 2,5 V peak reading, relative measurements, 20 kSample – the 'gain error noise' is 163 µV whereas the random noise is 2.86 µV, therefore the system approaches the precision of the quantization (153 µV).

It follows that the A/D conversion meant no bottleneck in the read-out circuit.

2.4 180 nm Serially connected sensor array

The subject of my work links closely to the manufactured detector; therefore, I describe it in details in this separate section [2].

DOI:10.15774/PPKE.ITK.2015.006

To create images from the aggregated response we perform multiple complex measurements and optimization based reconstruction. In order to reduce also the acquisition time we can utilize the sampling scheme of compressed sensing. For this, one has to control the contribution of the individual detector elements to realize the complex measurements (represented by the matrix, Φ).

The solution of the COSPL at the ICSC – HAS allows complex sampling by exploiting the specialties of FET plasma wave detectors in the THz region. The two domains have significant implementation differences as orders of magnitude lower source power and plasma wave detection challenge actual analogue VLSI techniques.

The proposed solution reduces the noise of the created images in the following ways:

- A common practice to increase the signal level of voltage-based detectors is to bind multiple ones in series [13]. Elkhatib et al proved in [14] and [15] that the response of FET plasma wave detectors also adds up and scales linearly with the number of involved devices. (The thermal noise also increases, but only with the square root of the number of detectors.)

  Of course, the per pixel SNR remains the same, but this increase of the sensor SNR means higher, shifted signal level that is advantageous by the amplifier implementation.
- Compressed sensing reduces the needed sample count and decreases noise directly as well as the non-linear reconstruction can suppress Gaussian noise to certain extent [16].
- As the pixel cluster is serially connected, only one low noise amplifier (LNA) contributes to the output noise per cluster.

2.4.1.1 The working principle

In the case of FET based terahertz sensing, it is possible electronically controlling the photoresponse of each serially connected sensor elements. Figure 15 shows the typical response of a detector against U_{GS} that we measured on the proof-of-concept chip of the COSPL in open circuit mode. This indicates that we can significantly reduce the photoresponse and resistance contribution (i.e. thermal noise) of a given detector to the output by fully opening the detector transistor ("OFF" state). The created detectors are 1.8V standard transistors on a 180 nm CMOS technology. Worth to note, that the optimal gate bias voltage for the "ON state" depends on the number of active pixels. Moreover, they not necessary coincide with the maximum responsivity gate bias [15]. However, even a single, general bias voltage can provide acceptable performance (see measurements in section 4). This allows utilizing only simple, binary pattern generator circuitry with only two constant reference voltages (e.g. 0.35V and 1.8V). The exponentially increasing current induced flicker noise becomes dominant in subthreshold operation region, thus NEP minimum turns up at higher gate voltage regions.

DOI:10.15774/PPKE.ITK.2015.006

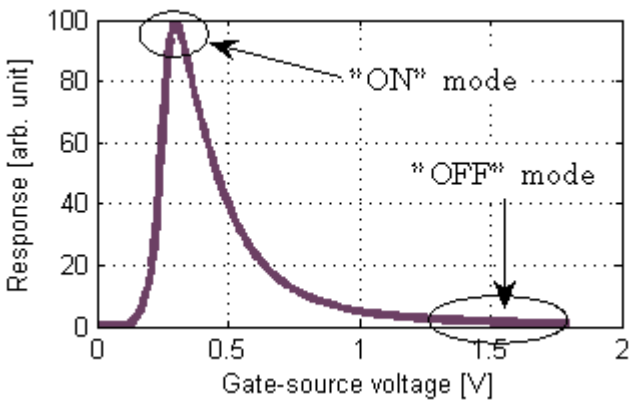

Figure 15 A measured, typical response of the detector array at different gate-source voltages

The frequency characteristics of the array is showed in Figure 16. This measurement was carried out with all pixels activated by uniform gate bias.

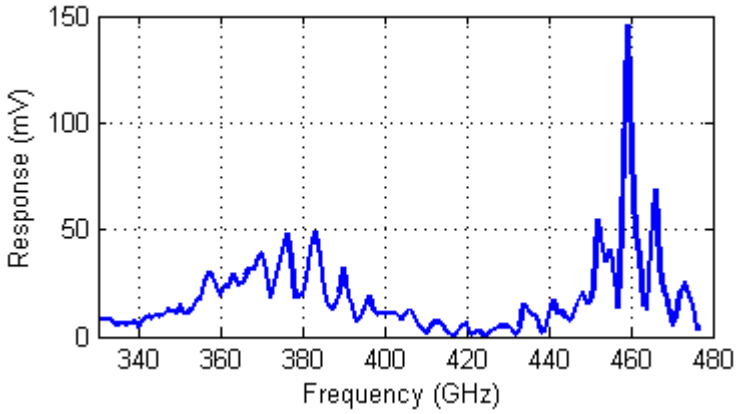

Figure 16 Average frequency characteristics of the detector array in the 330-480 GHz range

The originally targeted frequency was 470GHz to accommodate the specific power spectrum of the given AMC source. Because of the computational burden of precision, the simulations were done in two rounds: first with simplified structures and afterwards with the precise model of the chip including the dielectric layers, passivation and exact copy of the 3D structure exerted from the output of the layout program.

Comparing the simulation results of isolated, standalone versions and densely populated arrays of several pixels showed that frequency shifts upwards if more detectors are arranged near to each other. Figure 17 Part B and Part C is an example that shows that besides the reduction of gain a frequency shift with a factor of about 1.0187 occurs.

Thus, optimizations can be done on simplified models of isolated antennas by decreasing the target frequency to 460GHz. In the second round, the corresponding precise, isolated structures have a resonance frequency of 450 GHz (see an example in Fig. 10 Part A). Hence, the expected frequency peak for the array was about 458 GHz. On the chance that several other, non-simulated effect can increase the resonance frequency, we have kept this configuration.

DOI:10.15774/PPKE.ITK.2015.006

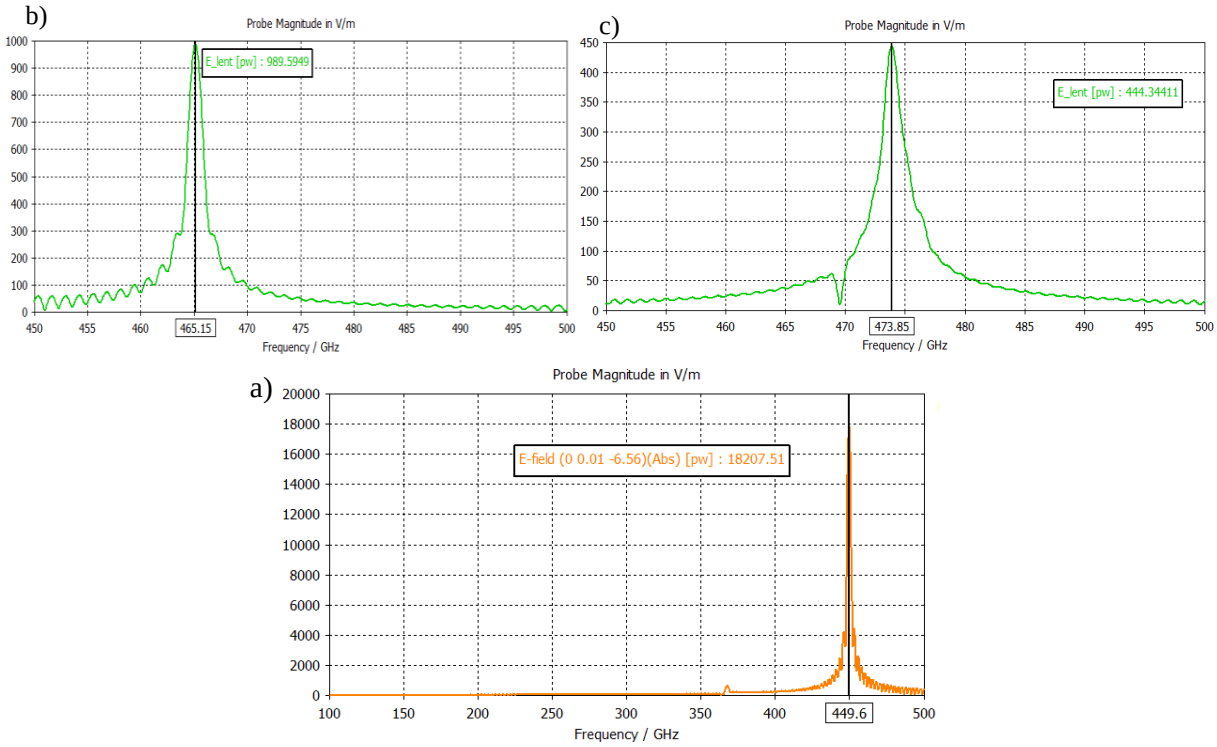

Figure 17 Resonance frequencies of different simulated structures

2.4.1.2 Details of the prototype detector array

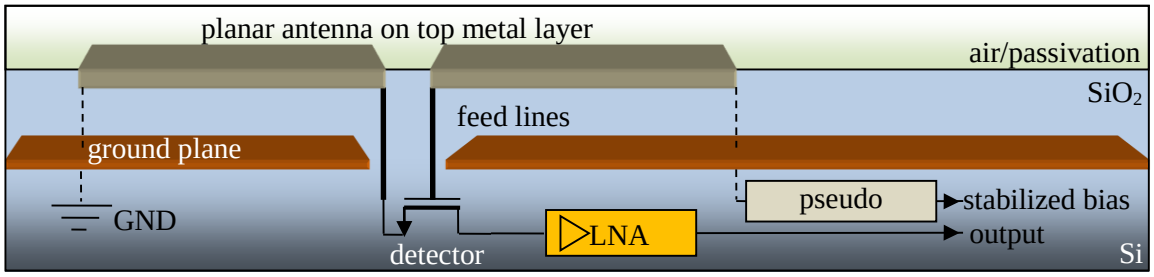

Figure 18 The scheme of a MOS based terahertz sensor element (figure repeated from section 2.3.3.1)

The detector array performs power intensity measurements at a single frequency of 460 GHz. Figure 18 shows the scheme of a single detector element, where detection is realized on an nMOS transistor by self-mixing. Considering the 125-750 GHz source frequency range and the Si MOSFET detector of 180 × 300 nm^2 size the non-resonant, long channel approximation applies [8]. Manufacturing came off at standard CMOS 180 nm technology sparing any extra post-processing. The antenna arms connect directly to the gate and source terminals of the detector transistor with the γ-shaped vertical structure built from via arrays and metal layers; see Figure 20 Part C. Thin, high inductivity wire connections ensure the proper biasing of the FET. Their placing is a crucial design step, especially at not nodal regions, because these contacts can fundamentally change the resonance of the antenna.

DOI:10.15774/PPKE.ITK.2015.006

The detectors run in both open-circuit and injected current configuration. Enforced drain current increases both the response and the noise [9] [5]. Because of the increased detector noise, the achievable SNR is lower than in open-circuit case, but the higher signal level can reduce the requirements of the auxiliary electronics and make scalable integration easier. This agrees with the results of Lisauskas [10], who deduced a theoretical upper limit of current mode gain that is about 1.35. In the actual measurements, I do not use induced current mode.

The gate bias is near to the open threshold voltage (0.2-0.5 V) and its optimal value depends on the load and the sampling scheme among others. Thus, the input impedance of the read-out circuit and the modulation frequency have large influence over the operating point [11]. Földesy [6] gave a unified model for all working conditions that explains all of the knnown measurments within the non-resonant frequency region. A single, two-component LNA conditions the signal of the pixel cluster with 100 times amplification. The lower and upper -3 dB cut-off frequencies are 10 Hz and 330 KHz, respectively. See Figure 19 for the schematics.

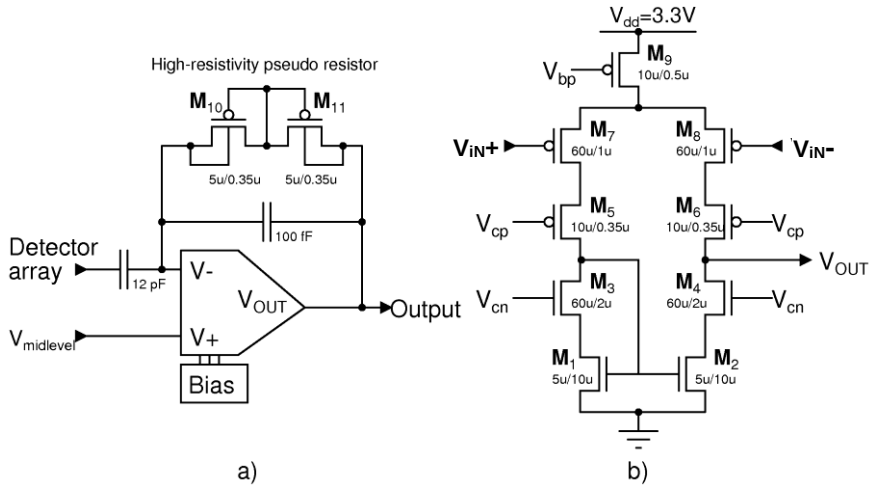

Figure 19 Schematics of the low noise amplifier a) shows the band pass amplifier filter and b) shows the telescopic OPA (This figure is from Földesy [6].)

The maximum system SNR appears at 1 kHz modulation frequency; over this value the response decays (roll-off effect). This is in accordance with the measurements of Sakowicz on single Si MOSFETs in [11]. The works, [8] and [11] give thorough analysis on the roll-off.

The transmission line between the detector transistor gate and the antenna feed point should be minimized to avoid losses. Therefore, the detectors got right below the feed point in every case. For experimental reasons, all the gates have direct terminals on output pads. However, our measurements prove capturing is still acceptable with uniform gate biases as well. This way it is enough to add a binary switching circuitry with two analog reference signals to realize a compact imager. Besides, several pixel clusters can share the same pattern generator.

DOI:10.15774/PPKE.ITK.2015.006

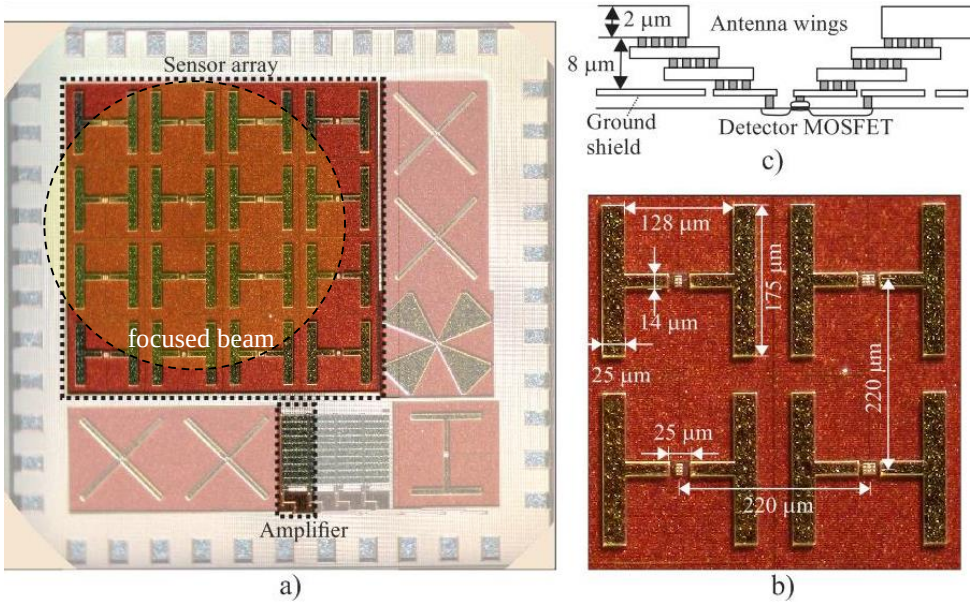

Figure 20 The image shows the physical design of the sensor array: a) microphoto of the chip, b) close-ups of four sensors with their designed dimensions, and c) illustrative figure of the antenna and detector MOSFET coupling (This figure is from Földesy [6].)

In Figure 20 Part A, one can see the microphoto of the detector array. We used H-shaped, single band, dipole antennas whose main dimensions are presented in Part B. The chosen 220 µm pitch is not optimal; the available small chip area restricted us in this decision. Simulations showed that under a given pitch value the antenna gain decreases slowly. Hence, we decided to create a 4×4-pixel array that can demonstrate the idea of CS more faithfully.

The antennas are sensitive to surrounding metal structures that makes the placement of the front-end circuitry difficult. One solution is to put the belonging wiring and possible additional electronics under a ground plane (GP) as shown in Figure 20 Part C. This shield affects the antenna behavior seriously. It shifts the resonance frequency and increases the theoretical Q-factor.

The 3 dB bandwidth of these planar structures spans 1.5 GHz based on our 3D simulations. However, any process variation defect and environmental part (e.g. wiring, bonding, and packaging) degrades the performance by shifting the resonance frequency or altering the radiation pattern.

Figure 21 shows the measured frequency characteristics of the array in open-circuit mode with all pixels activated by a uniform gate bias and compensated with the power spectrum of the source. The simulated resonance characteristics of a single detector also appears in Figure 21 with scale on the right side; the inlet helps to compare the 3dB bandwidth of the real construction to that of the simulated one, where the excitation signal was a Gaussian chirp.

DOI:10.15774/PPKE.ITK.2015.006

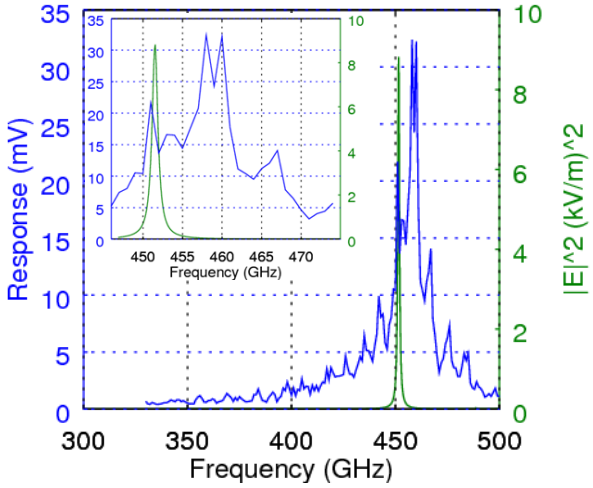

Figure 21 Measured and simulated frequency characteristics of the detector array in the 330-500 GHz range (left and right scale, respectively)

We utilized the BSIMv3 MOSFET model of the actual manufacturing technology to get the drain current characteristics of the detector transistor (see Figure 22).

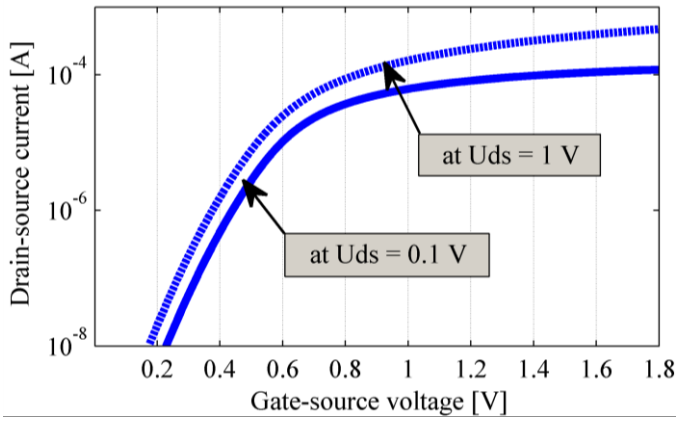

Figure 22 The simulated drain current of the used detector transistor: 180 nm nMOS of size 180 × 300 nm^2

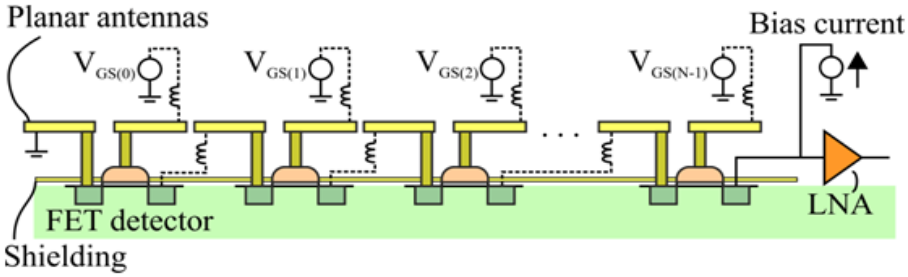

Figure 23 The stylistic schematics of a CS capable detector array

Figure 23 shows the schematic sketch of the proposed detector arrangement. The antenna and detector pairs are connected in series, consecutively chaining the MOS transistors at their source and drain respectively. Inside the pixel cluster, it is possible to tune the gate bias voltages independently. With that, we can control the contribution of each single detector independently.

DOI:10.15774/PPKE.ITK.2015.006

However, I used only two uniform gate biases for the ‘ON’ and ‘OFF’ state during my measurements with CS patterns. The serially connected functional blocks are placed in a meander style to form regular arrays on the chip. When doing so, one has to be careful with the connectional wiring.

To create imagers one can combine the proposed serially connected “pixel clusters” with standard read-out architectures.

2.4.1.3 Characteristics of the proof-of-concept detector array

We compared the performance to a standalone sensor with H-shaped antenna fabricated at 90 nm technology. This had the same detector structure as the sensors of the actual array only the resonant antenna sizes and planes differed. Both chip parts were thoroughly studied in a 3D, finite element, physical simulator, where the serial array was represented with six detectors at different densities (pitch values). The real and the targeted resonance frequency differed by roughly 1.5% (7 GHz uncertainty). The individual response of the detectors was about 23.5% of our best H-shaped standalone antenna, which worked at 360 GHz. This difference had two reasons. On one hand, the denser array arrangement and the higher frequency cause a loss of about 55% and 39%, respectively. On the other hand, due to the features of the 180 nm technology, the antennas got on a thinner metal layer (1.45 μm). Within the actual microstrip structure, this also lowered the antenna gain, but there is no simple trend as in the case of the ground plane distance.

Efficient utilization of the chip area requires minimal pitch, while preserving disjunctive effective areas of the antennas. Concerning this and the sensitivity of the antennas to the additional metal structures, placement of the front-end circuitry can be problematic. One solution is to put the belonging electronics under a ground plane (GP). This restricts the number of metal layers for routing, but it confines the antenna behavior more seriously. It shifts the resonance frequency and increases the theoretical Q-factor to an unwanted level that decreases the resonance amplitude of the real device due to the distortions.

Figure 24 shows this effect and summarizes the simulated behavior of our H-shaped antenna at different GP positions.

DOI:10.15774/PPKE.ITK.2015.006

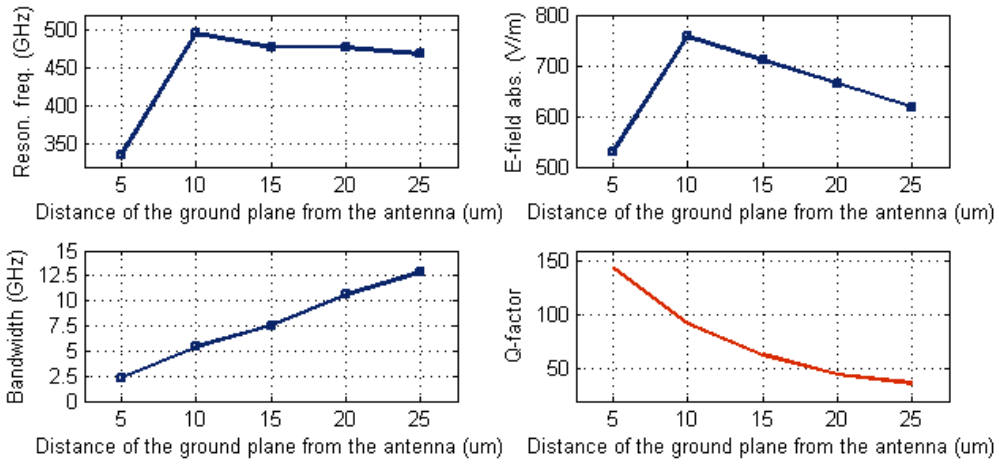

Figure 24 The effect of ground plane distance on the antenna characteristics

To get an insight into the relative radiation patterns of the individual detectors, I have done beam scans with the detector array. For this, I used the configuration presented in right part of Figure 5, Part A. The step size of the 2D scan was 0.1 mm in both directions. First, I have done measurements with single sensors by activating only one detector transistor at a time. In Figure 25 Part A, the radiation patterns – convolved with the Gaussian beam of the source – can be compared. Here, each small picture is a full raster scan of the Gaussian beam with the belonging detector.

Figure 25, Part B shows an additional measurement with all pixels activated at 0.3 V uniform gate bias. The scanned field of view is the same in every case (2.5 × 2.4 mm^2). The distortions come mainly from the metal layers of the pads and the wiring of the detectors that are invisible on the microphotograph (Figure 20).

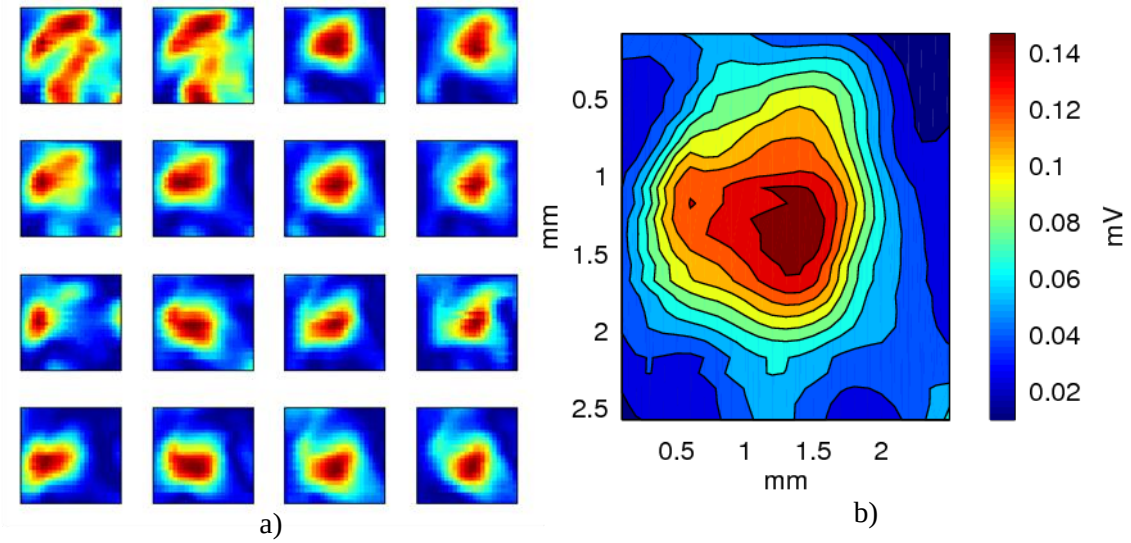

Figure 25 Beam scans with individual antennas to check proper pixel separation

Figure 26 explains the cumulative answer relative to the single detector responses. For an optimal summation, each detector should have a separate bias voltage to work at an ideal

DOI:10.15774/PPKE.ITK.2015.006

operating point as measured in [19-20]. Every bias would compensate the summed response of the preceding detectors, as well. By unbiased detection, if responses are small relative to the gate dependence, these effects are small. Since the individual signal levels were below 0.5 mV, a uniform gate bias is theoretically appropriate. The ‘inter die’ process variation of the pixels was around 9.1 % based on three measured chips. Thus, the transistor mismatch was significant and the distortion of the antenna radiation patterns added to this as well. However, not these, but the loading effects determine mainly the responsivity of the detectors; see [35]. Therefore, by open-circuit mode, consecutively connected detectors always have some responsivity loss. With the length of the continuous serial chains, this loss increases. Therefore, by switching on all detectors with the optimal, uniform gate bias the fused response approaches only 43 % of the sum of the individual responses; see also the subfigure at the top right corner of Figure 26 as an overview.

However, the random activation patterns break up the long serial chains and decrease the losses. Eighteen measured random patterns containing 3 to 11 active pixels confirm this in Figure 27; the patterns were randomly generated and presented without any selection. On the average, the responses of the random patterns are 80.7 % of the theoretical sum of the individual pixel responses that constitute the patterns.

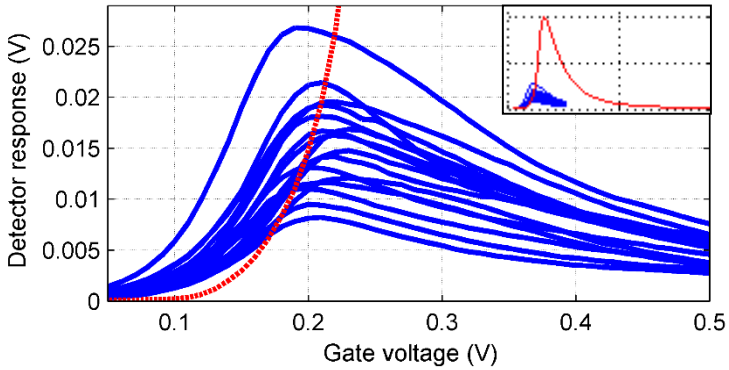

Figure 26 The measured characteristics of the individual detector responses (blue lines) and the fused response – all detectors switched on (red line)

In Figure 27 Part A, the two continuous lines point out the mean of the 18 corresponding values (the higher for the theoretical and the lower for the measured response). The CS pattern responses show high correlation with the theoretical sum of the individual detector responses: the mean, normalized error is 2.9 % that can be compensated likewise the fix pattern noise. I present this in Figure 27 Part B, where both groups of values were normalized to their mean. The CS images presented in section 4 were made with the first 14 of these patterns. However, I suggest using selected patterns that contain only 11 or more active pixels.

DOI:10.15774/PPKE.ITK.2015.006

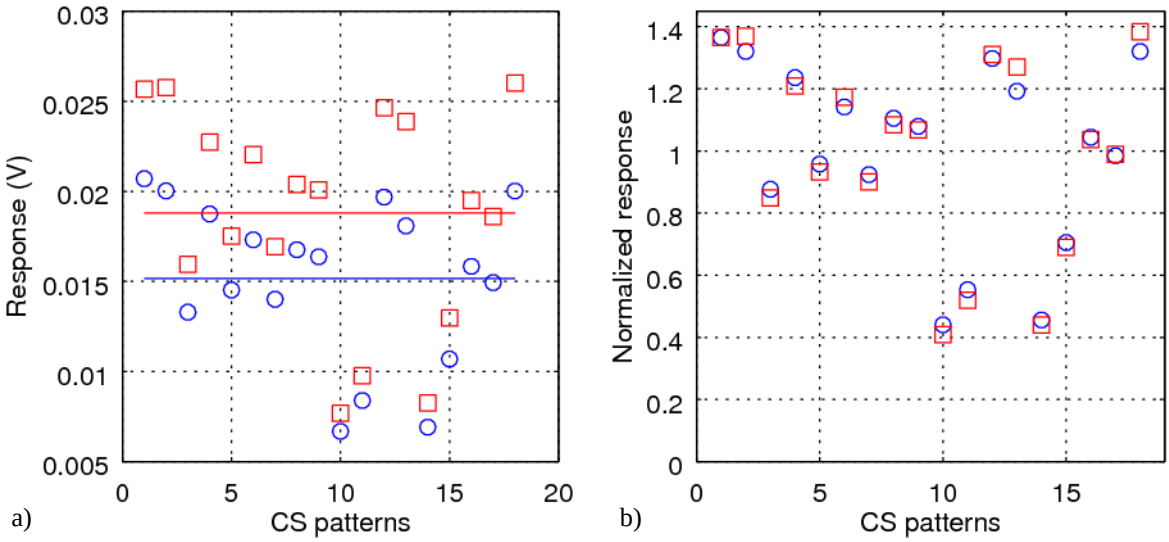

Figure 27 Performance comparison of the CS patterns (blue circle) to the theoretical sums (red square)

DOI:10.15774/PPKE.ITK.2015.006

3 NOISE PERFORMANCE OF COMPRESSED SENSING BASED DETECTORS

3.1 Motivation

My aim was to study the noise characteristics of the measurement system and perform a kind of 'holistic' analysis on that. The holistic nature means that the selected figure of merit represents not a component wise, but a system level requirement: maximizing the resulting image SNR of the terahertz measurement system. That is, the study includes both the hardware components (detector, LNA, readout-circuitry) and the post-processing. Hence, the work involves the heuristic combination of these two different aspects:

First, I investigate the non-linear reconstruction framework of CS to create images. The CS framework makes possible to increase acquisition speed and to add any additional information to the data that is available at the time of the post-processing about the imaged object: e.g. statistical properties of the noise and the imaged scene or more reliable measurement data about specific parts (pixels) of the scene. (Some of this information is available a priori, while the rest need additional measurement or the analysis of the previous images. Besides, conventional noise filtering and noise suppression techniques may also fit to this process.)

In the end, this makes possible to increase the SNR of the acquired image by reducing the error of the reconstructions at the expense of more intense post-processing on the measured data set.

Second, I investigated the performance of CS capable imaging devices (serially connected sensor arrays and SLMs) comparing them to conventional sensor arrays.

In the following section, I have to enlighten the relation between the sensor architecture and the main problems of system integration, implementation regarding the overall system performance (the SNR of the application specific output images).

3.1.1 The aspect of implementation and system integration

Utilizing standard CMOS technology to form terahertz imagers can be a crucial step to make room temperature terahertz investigation became a ubiquitous modality in biology and medicine. However, very-large-scale integration (VLSI) implementations may limit the resulting image SNR of such integrated devices. The read-out circuitry is a key point that has a great impact on the overall performance of the imager. It determines the sample count (S), the maximal integration time (t_{int}), and most of the additional noise sources.

The majority of the implementations multiplex the read-out; the number of low noise amplifiers (LNAs) is smaller or equal than the number of columns in the array and the number of A/D converters (r) is even more restricted: $r \ll N$, where N is the total number of pixels in the array. This confines the sample count (S) in any case:

DOI:10.15774/PPKE.ITK.2015.006

$$S < \frac{\mathrm{r\ f_s}}{\mathrm{N\ fps}} \tag{25}$$

where r, f_s and 'fps' stand for the number of A/D converters, the sampling frequency and the acquisition speed (frame per second), respectively.

The small area available for one pixel restricts the size of the integrating in-pixel capacitance, therefore also the integration time. Near-continuous integration would mitigate this problem with correlated double sampling (CDS) or correlated multiple sampling differential averaging (CMSDA) techniques by sampling at higher rates and averaging [17]. The noise suppression can be as high as 40% according to a paper on CMSDA [18] considering 1/f noise and fixed pattern noise.

However, the switching noise of the direct path still remains a significant, additional noise source of this solution, according to [17]. Moreover, I do not know yet working terahertz implementations of the CMSDA technique that could provide measurement data on that.

Due to the relatively high 1/f noise and the weak THz sources, frequency filtering is advisable that increases SNR with orders of magnitude. If lock-in amplification is assumed by digital phase-sensitive detection (PSD) in the post-processing, then the source modulation frequency (f_{sm}) gives an upper bound for the in-pixel integration time either way:

$$\mathrm{t_{int}} \leq \frac{1}{2\mathrm{f_{sm}}}. \tag{26}$$

Because of (1) and (2), the total noise power (P_{total}) shall depend on (N fps). Hence, the SNR will degrade by scaling-up and as N $\gg$ fps, it will be easier to produce low SNR, real-time video than high sensitivity images in several seconds. (The NEP value of sensor pixels refers to an ideal, 0.5s long integration.)

3.1.2 Considerations on the setup

Today terahertz applications are still SNR critical, but need higher resolutions and increased speed. The size of the integrated antenna coupled detectors has shrunk relative to the free air wavelength, enough to consider only $\lambda/4$ structures: dipoles, spirals, and bowties. The enclosing dielectrics also strengthen this effect increasing the effective length of the antenna compared to corresponding free air version. However, their responsivity and provided SNR also drops with their size. To meet the contrary requirements of lowering optical noise equivalent power (NEP) and increasing resolution is an active research topic [19].

In many optical setups, a natural oversampling takes place and the resulting image could be spatially averaged without significant loss of information. Images limited in spatial frequency are more likely compressible, that is, they can be represented more efficiently in a proper base (e.g. discrete cosine transform). Thus, they can be acquired by compressed sensing more efficiently. For instance, one can utilize aggregated architectures in the following cases:

DOI:10.15774/PPKE.ITK.2015.006

- Diffraction limited optical setups
- Setups with small sized, integrated focal plane arrays (FPA), where planar antennas are embedded in dielectrics with $\varepsilon_{eff} > 1$ (increase in effective length)
- The promising, slightly magnified, lens free holographic imaging belongs to these as well [20] [21] [22] [23] [24]. In appropriate setups, holographic coherent diffraction imaging (HCDI) also could benefit from averaging as it makes spatial oversampling of diffraction patterns unnecessary [25].

  An exemplary problem: Reflective imaging of soft tissue, cell culture or thick excision, where the scattered beam is highly diffuse and it is hard efficiently focusing it – In this case, additional optics, such as silicon solid immersion lens, can only partly mitigate the problem, but they decrease the source intensity and introduce further frequency dependent distortions, aberrations.

3.2 Methods

3.2.1 General approach

My goal was to evaluate the design decisions concerning their effects on the overall system performance, where the starting point of all investigations was the presented 180 nm sensor array of the research group at the ICSC (Section 2.3.1). The main task was to give a quantitative analysis on the effect of a serial sensor architecture considering also the needed post-processing. For this, a kind of "holistic" system modeling was utilized that covered every essential component of the imaging system. That is, I measured and calculated the change of the resulting image SNR (a system level indicator) concerning a change in one or more components (e.g. induced current of the detector, array size, and achieved compression).

This can be seen as a basic approach for a heuristic system level optimization: do not evaluating the design choices one by one, but mitigating the sensing problem as a whole. Figure 28 depicts partly the causation of the 4 targeted problems assuming room temperature, FET based detection with a tunable CW source. These notions can be divided further as going in to the details. Such diagrams are exemplary tools of concept sorting and determining the relationships between them in order to determine the most appropriate solutions for the problems at hand.

I assessed that the right choice of the sensor architecture, the optical setup, the measurement scheme and the post-processing can significantly improve the overall performance of THz imaging systems that involve CW source and FET based integrated detectors.

DOI:10.15774/PPKE.ITK.2015.006

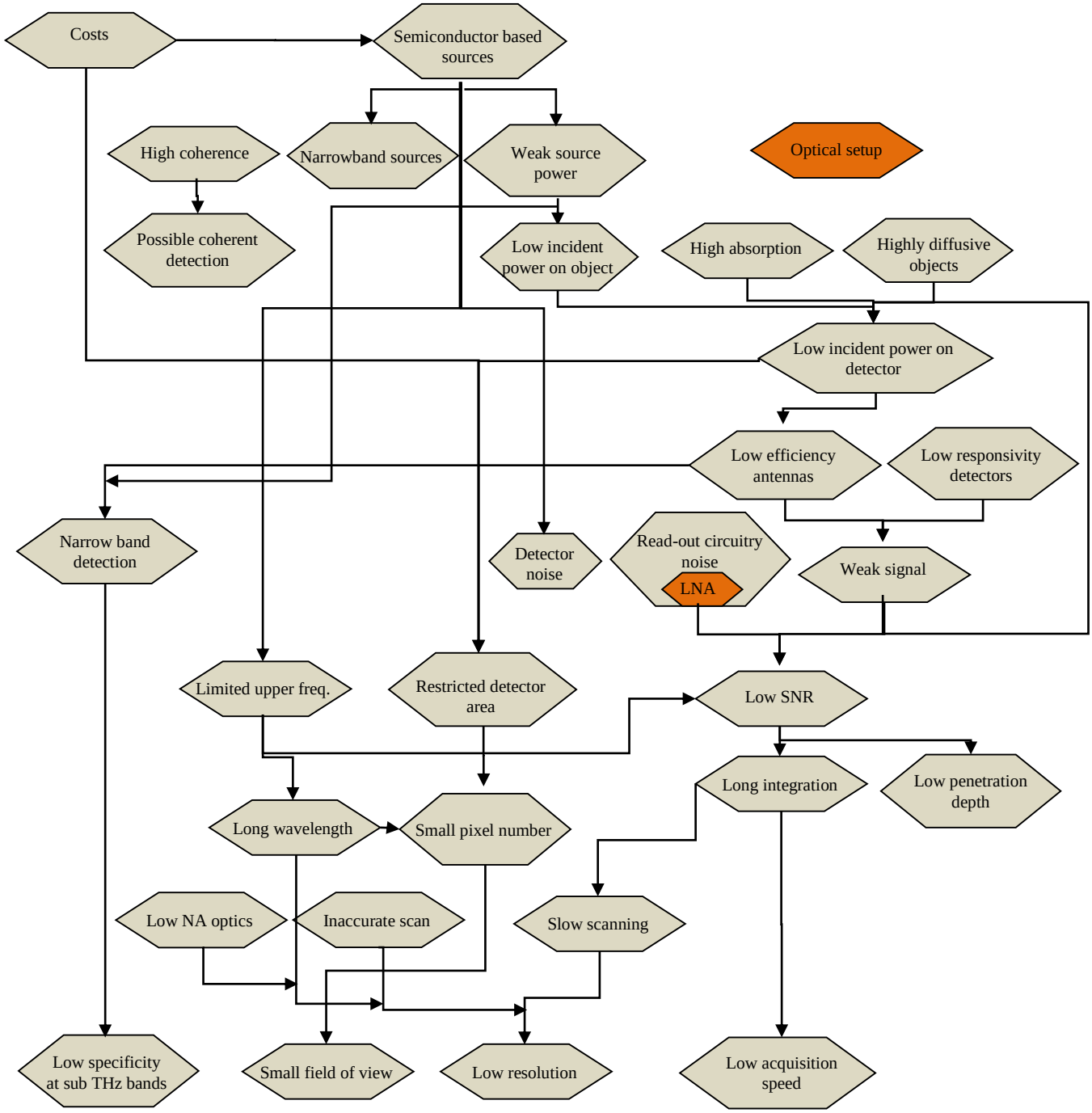

Figure 28 The diagram summarizes several touched notions connecting to the sensing problem and partly reveals the roots of the main problems;

The architecture can help to approach the theoretical performance of the detectors (LNA noise contribution, resource allocation within the read-out circuit) and it must suit to the inseparable triad of the optical setup, measurement scheme and post-processing framework that support noise filtering (and by any chance super resolution).

DOI:10.15774/PPKE.ITK.2015.006

3.2.2 Cross validation for increasing SNR

Cross validation (CV) has several applications within CS and has rigorous mathematical background. However, related works like [17] and [43] focus mainly on the approximation error estimation, and aiding the choice of parameters like the number of measurements or the assumed sparsity.

On the one hand, I investigate cross validation as a tool for reducing the noise of the reconstruction. In the end, this increases the SNR of the resulting images.

On the other hand, the low incident radiation implies we have to consider over sampling as well. I suggest, cross validation as an efficient way to integrate oversampling data with the compressed sensing based reconstruction framework. This way we can improve on the standard L_2 minimization (or least squares solution) results.

By usual compressed sensing imaging thorough cross validation is too expensive. Yet, in our case N is relatively small, meaning that the arising computational burden is tractable despite of the $O(L \cdot N \cdot \log(N))$ or in best case $O(L \cdot N)$ algorithms (here L is the order of CV).

By the suggested cross validation I divide the measured data set, D into two subsets D_1 and D_2. I perform the reconstruction using only D_1 (ignoring the elements of D_2) and may estimate the error of the candidate solution based on D_2, then I repeat the process with a different subset of another division. These iterations result in several 'candidate' solutions that can be combined on various ways to create the final image e.g. substitute the median of pixels or sum them weighted by their calculated error. The described technique belongs to thesis 1.2.

The proposed meta-algorithm connects to and extends the works [33] and [40]. Ward depicts the idea of using cross validation (CV) for the reconstruction in [33]. She mentions the main CV techniques and gives bounds on the L_2 error of the simple, incremental CV based on the Johnson-Lindenstrauss (JL) lemma [44].

Malioutov presents the idea of adaptive, sequential CS in [40], where, he gave the sufficient number of measurements for the reconstruction depending on the distance between the candidate reconstruction vector, $\boldsymbol{x}^{\mathrm{M}}$ (after M measurements) and $\mathrm{H}_{\mathrm{M+T}}$, the M+T dimensional affine subspace, where T denotes the number of spared, unused measurements. $\mathrm{H}_{\mathrm{M+T}}$ is the subspace of $\mathbb{R}^N$ confined by all the acquired measurements. This technique builds upon the estimation of the error based on the T additional measurements.

3.2.3 Figure of merit

The performance of terahertz detectors is characterized by the noise equivalent power (NEP), since it is a source power independent performance indicator of the sensory system. It incorporates both the noise power level of the detector and its responsivity as well. By definition, NEP is the input power that produces a signal to noise ratio of unity at the output of an optical detector:

DOI:10.15774/PPKE.ITK.2015.006

$$\mathrm{NEP_{detector}} = \frac{\text{noise voltage}}{\text{responsivity}} = \frac{\mathrm{U_{noise}}}{\left.\frac{\mathrm{U_x}}{\mathrm{P_{in}}}\right|_{x=0}} \tag{27}$$

where U_x is the voltage response of the detector at x input power. NEP assumes 1 Hz detection bandwidth (or 1 Hz sampling frequency) that means 0.5s integration time unless otherwise specified. NEP often defined also as the minimum detectable power per square root bandwidth changing the noise voltage ($\mathrm{U_{noise}}$) to the square root of the power spectral density ($\mathrm{S_{xx}}$) given in [V/√Hz].

$$\mathrm{NEP_{detector}} = \frac{\sqrt{\text{noise power spectrum}}}{\text{responsivity}} = \frac{\sqrt{\mathrm{S_{xx}}}}{\left.\frac{\mathrm{U_x}}{\mathrm{P_{in}}}\right|_{x=0}} = \frac{\mathrm{S'_{xx}}}{\left.\frac{\mathrm{U_x}}{\mathrm{P_{in}}}\right|_{x=0}} \tag{28}$$

In eq. 28, the dimension of the NEP also changes to [W/√Hz]. The responsivity characteristics of these detectors is usually not linear and less steep at the initial phase. Yet, such a measurement can be cumbersome without an appropriate equipment. Thus, often the mean responsivity of the full utilized dynamical range is used to calculate the NEP (so did I):

$$\mathrm{NEP_{detector}} = \frac{\mathrm{U_{noise}}}{\frac{U_{max}-U_{min}}{P_{max}}}\,. \tag{29}$$

This a good and practical approximation of the real performance of the detector. In this work I concentrate on the noise part of this performance indicator, thus it is easier to handle the different components by their noise figure (NF) providing ground for comparison independently from the amplifier gain:

$$NF = 10\log\frac{SNR_{in}}{SNR_{out}} = 10\log\frac{T_{off}+T_{on}}{T_0} \tag{30}$$

$$T = \frac{P_{noise}}{Bk_B} \tag{31}$$

The noise figure is dependent on the load presented to the given component and this formula applies to the matched case. T_{off}, T_{on} are the noise temperature of the component in OFF and ON state respectively, where as $T_0 = 290K$ is the reference noise temperature. B stands for the bandwidth at which the noise figure measurement is carried out and k_B is the Boltzmann constant. The noise temperature (T) assumes an additive, white noise source distribution. In this case, it is an acceptable estimation to handle the noises in a lumped form, if the measured bandwidth is restricted to a narrow portion of the frequency range, because flicker and shot noise can be also significant. To make easy comparisons to other indicators (e.g. NEP), one can use the approximation $T_{off} \approx T_0$, to calculate the absolute mean square noise power:

$$P_{noise} \approx T_0\left(10^{\frac{NF}{10}} - 1\right)Bk_B\,. \tag{32}$$

However, in an application environment the specification of the imaging system is usually

DOI:10.15774/PPKE.ITK.2015.006

described at a higher level, controlling only the quality of the results. Noise temperature means an easy, intuitive comparison among components with different impedances.

The resulting image SNR is taken as the main figure of merit regarding image quality. It is calculated according to the standard form:

$$\mathrm{SNR}_{\mathrm{result}} = 10\, log_{10} \frac{\|\mathbf{x_1}\|_2}{\|\mathbf{x_1} - \mathbf{x_{res}}\|_2} \tag{33}$$

where $\mathbf{x_1}$ is the original image (represented as a column vector) and $\mathbf{x_{res}}$ is the result of the processing. However, we calculated in every case the L_1 distance as well, which is proved to approximate the image quality better:

$$L_1\ \mathrm{error}_{\mathrm{result}} = 20\, log_{10} \frac{\sum|\mathbf{x_1}|}{\sum|\mathbf{x_1} - \mathbf{x_{res}}|} \tag{34}$$

3.2.4 Noise reduction basics

This part describes the profound basics of the noise reduction. I represent both the signal and the noise with a random variable drawn from normal distributions, $N(\mu_{sig}, \sigma_{sig}^2)$ and $N(\mu_0, \sigma_0^2)$, respectively.

Due to the central limit theorem, the sum of N identical distributions with expected value μ and variance σ^2 converges to a normal distribution $N(\mathrm{N}\mu, \mathrm{N}\sigma^2)$. This convergence in practice is fast, even the sum of 3 random variable can follow the rule well. Hence, their average goes to $N(\mu, \mathrm{N}(\sigma/\mathrm{N})^2) = N(\mu, (\sigma/\sqrt{\mathrm{N}})^2)$.

If we see σ^2 as the physical correspondence of noise power, then the average noise amplitude of N samples becomes √N times lower and the noise power reduces with a factor of N. Due to the conventions in the definitions of different noise representations (e.g. NEP), often altered units are used (V/√Hz or A/√Hz). Since these do not conform to the last statement, I use altered factors for the noise calculations.

Thus, a √N times reduction in σ_0 results in a reduction of only √N times in NEP as well.

We measure noise as voltage fluctuations at the detector output, and represent it by a random variable X from a normal distribution $N(\mu_0, \sigma_0)$. Then 'σ_0^2' should correspond to the average noise power amplitude. However, in measurements one often uses the power spectrum to indicate noise:

$$\mathrm{S_{xx}}(\omega) = \frac{\Delta \mathrm{t}^2}{\mathrm{T}} \left|\sum_{\mathrm{n}=1}^{\mathrm{N}} \mathrm{x_n} \mathrm{e}^{-\mathrm{i}\omega \mathrm{n}}\right|^2 = \frac{\Delta \mathrm{t}}{\mathrm{N}} \left|\sum_{\mathrm{n}=1}^{\mathrm{N}} \mathrm{x_n} \mathrm{e}^{-\mathrm{i}\omega \mathrm{n}}\right|^2, \tag{35}$$

where $\mathrm{x_n}$ with $n \in (1, \mathrm{N})$ stands for the measured photoresponse in Volts; Δt, and $\mathrm{T} = \mathrm{N}\Delta\mathrm{t}$ are the sampling period and the total measurement period, respectively.

I connect the notions of probability theory and statistics with the physical values through the following approximation:

DOI:10.15774/PPKE.ITK.2015.006

$$\sigma^2 \approx \frac{1}{M}\sum_{i=1}^{M} S_{xx}(\omega_i)\Delta\omega\,, \tag{36}$$

where M is the number of frequency bins within the frequency range under investigation and $\Delta\omega$ is the frequency resolution.

If the power spectral density is given in V/√Hz or A/√Hz ($S'_{xx}(\omega_i)$) , then (36) modifies to

$$\sigma^2 \approx \frac{1}{M}\sum_{i=1}^{M} (S'_{xx}(\omega_i))^2\Delta\omega \tag{37}$$

3.2.5 Assumptions

By the calculation of the mean instantaneous noise power of the detector and that of the LNA, I assume several conditions. At first, I take the input as a pure sinusoid. Since the lock-in amplification demands source modulation the YIG is driven by a square-wave signal at a distinct frequency therefore this is an acceptable approximation.

I assume that the impedance of the detector transistor (the source) matches the input impedance of the LNA.

I distinct between the three main types of noise sources with belonging spectral characteristic, but I assume the underlying processes to be Gaussian and I handle them together in the power calculations.

The output consists of several identifiable noise sources (or artefacts) that can be easily removed like the 50 Hz noise of the electrical network or the typical build-up phase of the signal at the beginning of the transitions in the "on-off-off+on" measurement scheme.

The windowing function plays an important role by the measurements. Both constant offset and linear drift have to be canceled. Considering white, 1/f and $1/f^2$ noise power spectral densities (PSD) the used "on-off-off+on" measurement scheme seems to be a standard in the field, see [37].

3.2.6 Noise model of terahertz FET detectors

The applied noise model provides the power spectral density of the detector and consists of the three usual additive components: flicker noise, shot noise and thermal noise.

I preferred to use the unified model of Hung to represent the flicker noise [38]. Thus, the model gives reliable noise values both for NMOS and PMOS devices in all operational domains. The input referred flicker noise power is given in $\left[\frac{V^2}{Hz}\right]$:

$$S_{V_g}^{flicker}(f) = \frac{kT}{\gamma f WL} N_t(E_{fn}) \left(\frac{q}{C_{ox}}\right)^{2-p} \left[\alpha\mu\left(V_g - V_{th}\right)\right]^p, \text{ where} \tag{38}$$

$$p = \begin{cases} 0, \text{if } N \ll (\alpha\mu)^{-1} \\ 1, \text{if } (\alpha\mu)^{-1} \leq N < N_{sat} \\ 2, \quad \text{if } N \text{ is close to } N_{sat} \end{cases}$$

DOI:10.15774/PPKE.ITK.2015.006

$\alpha \approx 10^{-15}$ [Vs] for scattering of electrons by oxide charge at the Si-SiO_2 interface

$\mu \approx 500 \left[\frac{\mathrm{cm}^2}{\mathrm{Vs}}\right]$ electron mobility

$\gamma \approx 2 \cdot 10^8$ [cm^{-1}] attenuation coefficient of the electron wave function in the oxide

C_{ox} bulk to gate capacitance

N is the charge carrier density in the channel

$N_t(E_{fn}) \approx 2 \cdot 10^8$ [$\mathrm{cm}^{-3}\mathrm{eV}^{-1}$] is the effective oxide trap density at the quasi Fermi level

Shot noise is covered with the following classical approximation regarding the spectrum and the root mean square voltage fluctuations (σ_v):

$$S(f) = 2q|I| \text{ and } \sigma_v = \sqrt{2qI\Delta f}R, \text{ where} \tag{39}$$

q the elementary charge

I is the DC current through the transistor channel

Δf is the considered bandwidth (here it comes from the minimal integration time: < 1 µs)

$R = \sum_{i=1}^{N} R_{ch_i} + R_{load}$ is the total resistive load (detector transistor channels and readout circuitry load, respectively)

Although, under the current working conditions (room temperature, low frequency) its contribution would be significant only in the < 100 nA drain current range, thus it can be neglected. For the thermal noise we simply use the white noise approximation:

$$S_V^{thermal}(f) = 4kBTR. \tag{40}$$

3.2.7 Detector response

For calculating the detector response, I have used the non-resonant approximation concerning the 100-460GHz working range. According to Lisauskas [10], this can be written as:

$$V_{photo} = \frac{V_a^2}{4\eta^2 V_T^2} \frac{I_0 R_d}{1+2e^{\frac{V_g - V_{th}}{\eta V_T}}} . \tag{41}$$

where the meaning of V_a, V_T, η, I_0, R_d, V_g and V_{th}, are listed in Table 3.

V_a	THz signal at the terminals of the detector transistor	R_d	channel resistance
V_T	thermal voltage	V_g	gate voltage
η	ideality factor	V_{th}	threshold voltage
I_0	initial current		

Table 3 Summary of the notations regarding the photo response

DOI:10.15774/PPKE.ITK.2015.006

3.2.8 Modeling of the system

The combined noise factor, F of an amplifier chain (or cascade of devices in the readout circuitry) is given as:

$$\mathrm{F} = \mathrm{F}_1 + \frac{\mathrm{F}_2 - 1}{\mathrm{G}_1} + \frac{\mathrm{F}_3 - 1}{\mathrm{G}_1\mathrm{G}_2} + \cdots + \frac{\mathrm{F}_n - 1}{\mathrm{G}_1\mathrm{G}_2 \ldots \mathrm{G}_{n-1}} \tag{42}$$

Where F_i is the noise figure of the *i*th stage and G_i is the belonging gain. Due to the usually high initial amplification, the first element would be the principal in general. Therefore, in the followings we indicate the post-processing noise only with the noise power of the LNA. Hence, the signature is simpler and the significance of the LNA noise is more intuitive.

According to this the noise power of the LNA on its input (P_{LNA}) and the output noise of the LNA (P_{noise}) can be written as:

$$P_{LNA} = \left(10^{\frac{NF}{10}} - 1\right) P_{det}\ ,\ P_{noise} = \mathrm{G}_1 10^{\frac{NF}{10}} P_{det} \tag{43}$$

Where G_1 is the gain of the amplifier; this factor falls out by the SNR calculations.

3.3 Results and conclusions

The CS acquisition is more than just a sampling scheme and belonging reconstruction algorithm as it means a flexible framework to process the measurement data in the form of a non-linear mapping between the measurement data and the resulting image. It inherently suppresses high frequency noises and helps sensitivity limited recordings to exploit the dynamical range of the sensors.

In the case of serial detectors, where the frequency of the pixel activation control is limited the reconstruction becomes an important question.

Thesis 1 [SNR enhancement of imaging systems with compressed sensing]

I have showed that the application of compressed sensing (CS) as a measurement scheme and a post-processing framework can increase the overall signal to noise ratio (SNR) of field effect transistor (FET) based terahertz imaging systems. [39]

Using CS in such an environment, where the theoretical conditions of the CS reconstruction (like sparsity) do not hold is not self-evident. This involves the acquisition of moderately structured (not sparse), small and noisy images. The guaranteed reconstruction error bounds do not hold or are so loose that makes them impractical for this scenario. (Determining the constants of some bounds is also unreliable for such small images.)

DOI:10.15774/PPKE.ITK.2015.006

To prove that the reconstruction works under these harsh conditions I have tested the performance of CS reconstruction algorithms whether they are capable to outperform the least-square solution of the problems or not.

I have given an actual example in the form of numerical simulations, where the CS measurement scheme yields SNR gain over the L_2 reconstruction technique in a specific parameter region. This result gave grounds to investigate some of the latent possibilities of the reconstruction and consider the use of CS as a measurement and reconstruction framework at serial detector arrays. CS algorithms tolerate noise relatively good. However, if the problem size is small (16×16 pixels), the measurements are noisy, and the imaged scene is less clearly structured then the problem became harder to solve. Figure 29 and Figure 30 demonstrate this phenomenon.

These figures summarize the outcome of numerous simulated CS measurements and image reconstructions, which mimic sensors with various signal-to-noise ratio and reconstructions involving different amount of measurement data relative to the total pixel count. The colorbar shows the resulting image SNR in dB. If we compare the output images to the original one, then the yellow part of the field indicates the region, which already has visually acceptable quality in these executions.

I have generated the used test images from natural, high resolution ones by cropping small regions of them. With this, I got moderately structured images (noisy, low contrast, slightly under sampled – “diffraction limited”) that resemble real THz measurements. Figure 30 illustrates the effect of increasing high frequency components in the sample image. On the left part, one can see the outcome of another assembly of simulations producing a similar image as Figure 29, but here, visualized as a surface. In the right part of the figure: the same simulation executed on an input image having higher entropy. The two objects have similar maxima, but the right one is much sharper indicating that the CS framework tolerates noise much less in this case.

DOI:10.15774/PPKE.ITK.2015.006

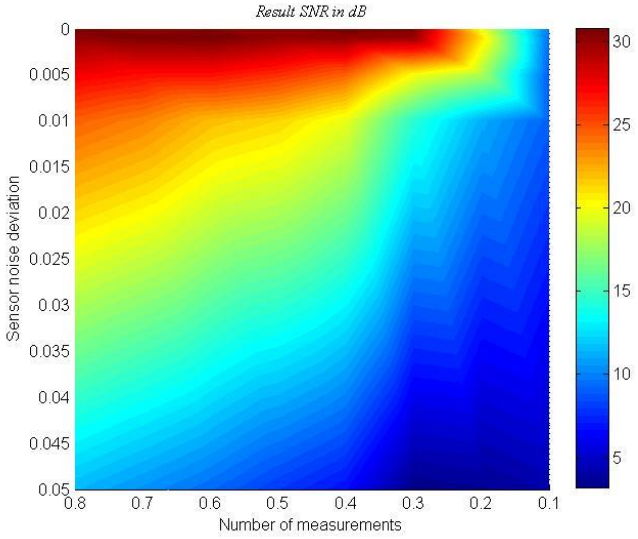

Figure 29 It shows the usual performance (SNR in dB) of a CS algorithm on a structured target. On the vertical axis, the standard deviation of the sensor noise is given relative to a fixed maximum that represents the mean maximal signal value in the measurement vector, "Y" based on several randommeasurements (to avoid referencing to an outlier). The horizontal axis shows the number of measurements relative to the total number of pixels.

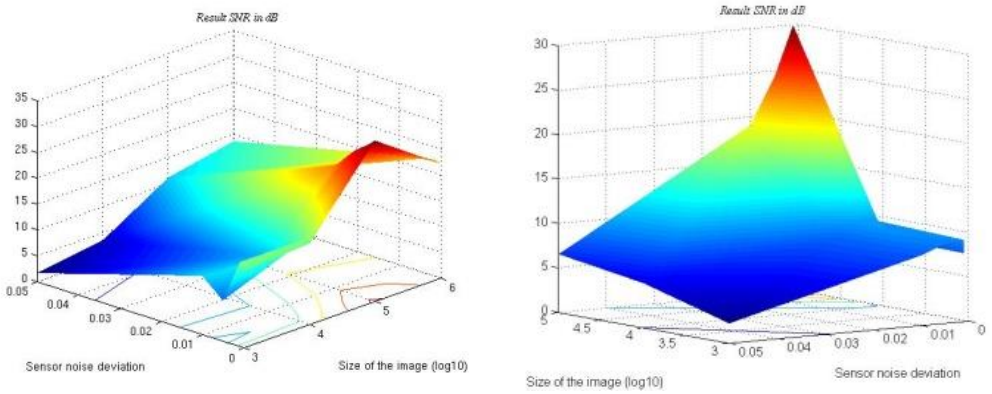

Figure 30 These example CS reconstructions give an insight to the effect of low sparsity. On the left one can see the image SNR as a surface over the image size and image noise axes. On the right I depicted the resulting SNR of the same algorithm, but sampling an image with higher entropy – indicating a richer surface texture. Their maximums are close to each other, but the latter became much sharper that is, it tolerates noise much less.

I investigated the parameter space determined by the noise variance, the size of the image, the M/N ratio and the entropy of the target texture and I found that there exist a small space where computationally more intensive methods yield considerable gain against L_2 minimization. This is visualized on Fig. 3. Here, an obvious case is shown of a less structured object. This example was performed with a smoothed-L_0 minimization algorithm.

DOI:10.15774/PPKE.ITK.2015.006

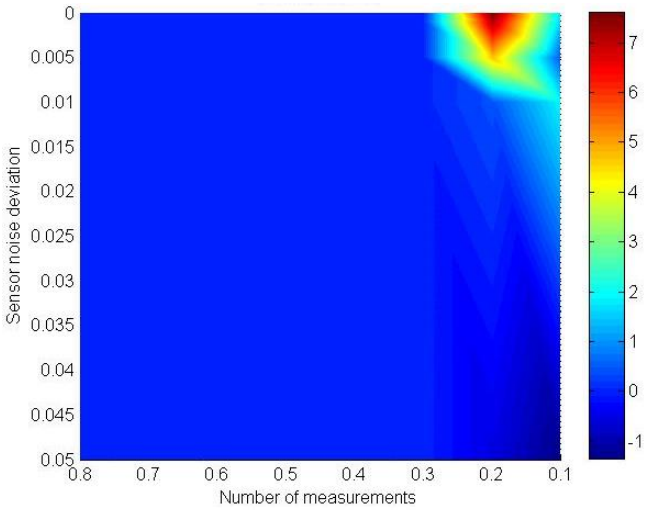

Figure 31 SNR gain of an alternate projecting algorithm over L_2 minimization. (The colorbar shows the gain in dB). On the vertical axis the sensor noise deviation is given relative to a fixed maximal signal value of Y. The horizontal axis shows the number of measurements relative to the total number of pixels. This test was performed on moderately structured images (sparsity around 0.75N) that are more close to the real measurements in tissues. This example makes obvious that for this type of application, the classical CS based algorithms have exploitable advances in a restricted region.

Based on these results I sentence the following thesis:

The potential of the CS technique for reconstruction serially connected sensors

Thesis 1.1 *I have shown that even a general smoothed L0-norm based algorithm can achieve gain over least-square reconstruction in case of small (0.25-3 kpixel), moderately structured (sparsity around 0.75N) images if the sensor noise deviation is below 0.01 and the compression ratio is between 0.1 and 0.3.*

With this, I conclude that a holistic optimization of a FET based, serial THz imaging system, where small images are acquired at relatively low SNR can incorporate the CS measurement scheme as well albeit the compression ratio of the L_1-norm based CS techniques depend logarithmically from the image size and is proportional to the sparsity. This point does not justify the use of the CS technique in any actual application, but proves the existence of an advantageous parameter region regarding image size, sparsity, compression ratio and sensor noise. Thesis group two deals with the closer relation of the CS technique to the physical implementations.

I have to emphasize that in typical applications of terahertz imaging the scene consists of mainly moderately structured features. The SNR of the investigated system is approximately 40 dB at free space (given the SNR as a voltage ratio). However, it drops rapidly either in transmissive or reflective configuration by scanning a specimen that has greater spatial extension or includes dispersive layers.

DOI:10.15774/PPKE.ITK.2015.006

The numerical simulations indicate that a system SNR between 31-36 dB is the practical lower limit of applying classical CS at 16 by 16 pixel images. However, under these extreme circumstances it provides practically no gain over L_2 minimization.

Therefore, I studied these measurement schemes and I have given application specific methods that help to exploit their intrinsical power: enhancing the image SNR by optimization driven reconstructions in the belonging post-processing.

Constructive algorithm to help exploiting the gain from the CS post-processing:

Thesis 1.2 *I have given a general post-processing algorithm for terahertz measurements involving cross validation (CV) and maximal entropy driven filtering that increases the overall SNR of the CS reconstruction in the presence of noise.*

Image noise cancels out by the addition of the pixel values, but sensor noise is a challenge for the sparsity driven reconstruction.

According to this, I have proposed to take more measurements than *M* by the acquisition. Then one has the chance to create different datasets of the same size (described in section 3.2.2). Assuming independent measurements, the new collection should induce the same stopping condition from [40]. Therefore, the candidate solutions x_{M_1} and x_{M_2} should be within the proven error of the reconstruction (an L_2 ball).

In the case of M + T samples, we could make a maximum of $\binom{M+T}{M}$ number of different data sets of size M. Then, if we take candidate solutions x_{M_i}, all should be within the range of the depicted error. Assuming that reconstruction error has Gaussian like noise components then averaging of appropriate candidates should decrease the error of the final result.

However, we have to be careful by choosing the right candidates, as adding up k dependent Gaussian or non-Gaussian random variables increases σ^2 proportional to k^2 and raise the offset error of pixels with their mean. Therefore, one has to create as 'distinct' datasets as possible. (The combinatorial nature of the original reconstruction problem does not imply such selections, but the L_1 problem may require this.)

The noise tolerance of the CV based post-processing and the relative performance of the proposed maximum entropy based filtering can be seen in Figure 32 and Figure 33, respectively. The averaging of the candidate solutions coming from the CV rounds result in an image that is low pass filtered too heavily. Therefore, I suggest maximum entropy based filtering or weighting to increase the entropy of the image to a more natural level with those pixels that have enough support among the results increasing the SNR of the outcome. According to this, we choose from the different candidate solutions those having the greatest entropy or rather weight them proportional to their entropy at the averaging.

DOI:10.15774/PPKE.ITK.2015.006

Figure 33 compares the normalized SNR of the proposed extensions regarding a reweighting algorithm that works optimally, selecting the weights of the candidate solutions based on the original picture.

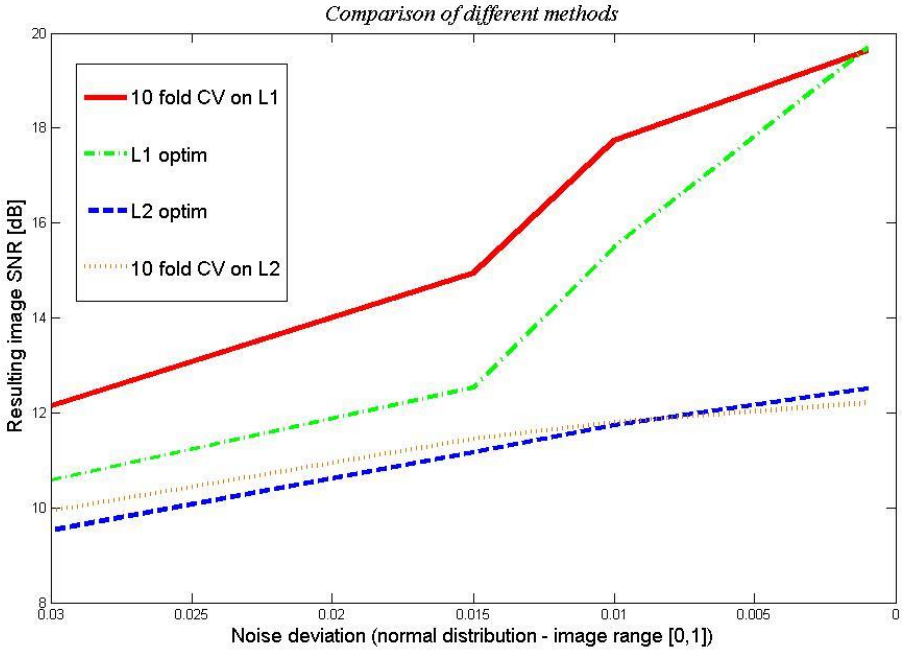

Figure 32 Comparison of the different optimizations used for the reconstruction of moderately structured images. On the horizontal axis the standard deviation of the additive noise can be seen assuming normalized pixel values. The vertical axis shows the achieved image SNR relative to the noise free case.

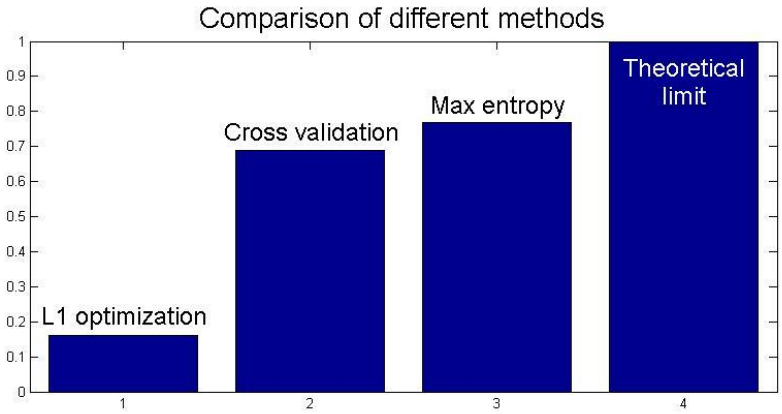

Figure 33 The comparison of the different reconstruction algorithms: L_1, CV and the CV + entropy based filtering at $\sigma = 0.015$. The vertical bars represent the normalized image SNR regarding an 'ideal' algorithm knowing the ground truth – the original image. The proposed algorithm increases the robustness of the CV based reconstructions.

The source of the gain is the intrinsical nature of the non-linear reconstruction. Giving emphasis to the application specific characteristics, I asses its advantage is it filters high frequency image noise efficiently and adds additional a priori information e.g. the input is structured or based on a given model. That is, given an appropriate base or library, the n-dimensional signal vector can be approximated more accurately with a candidate solution that has small L_0 or L_1 norm.

DOI:10.15774/PPKE.ITK.2015.006

Thesis 2 *[Relation of CS to physical implementations of terahertz imaging systems – holistic approach]*

I have shown, that in practical implementations of integrated FET based terahertz imagers, holistic optimization (system level, including both hardware structures and post-processing) results in SNR gain over the conventional component based optimization. Thus, otherwise deprecated solutions like serial connection of multiple detectors or induced current can be rational design choices. [1]

(The actual theses, 2.1 and 2.2 follow in the next sections.)

3.3.1 Passive gain of a CS architecture

Here I describe the passive gain of the architecture without considering the noise suppression of CS post-processing. This also means that I assume ideal reconstruction, because existing theoretical upper bounds do not reflect the real performance of actual CS algorithms (see more remarks on this in the discussion).

I define 'sample count' (S) as the maximum number of digitized samples, the imaging system acquires each frame to calculate a single pixel value (oversampling rate). Every frame assumes the reconstruction of all pixels.

Both the maximum integration time (t_{int}) and the frame rate (fps) are taken as a dimensionless ratio, where the point of reference is 0.5 s and 1 Hz, respectively – conforming to the definition of NEP.

Most of the implementations multiplex the read-out; the number of LNAs is smaller than or equal to the number of columns in the array and the number of A/D converters (r) is even more restricted: $r \ll N$, where N is the total number of pixels in the array. This confines the sample count (S) in any case:

$$S \leq \frac{r\, f_s}{N\, fps}\ , \tag{44}$$

where f_s and 'fps' stand for the sampling frequency of the A/D converters and the acquisition speed (frame per second), respectively.

The small area available for one pixel restricts the size of the integrating in-pixel capacitance, therefore also the integration time. Near-continuous integration would mitigate this problem with correlated double sampling (CDS) or correlated multiple sampling differential averaging (CMSDA) techniques by sampling at higher rates and averaging [17]. The noise suppression can be as high as 40% according to a paper on CMSDA [18] considering 1/f noise and fixed pattern noise. Although, the switching noise of the direct path still remains a significant, additional noise source, according to [17].

DOI:10.15774/PPKE.ITK.2015.006

t_{int}	*We assume no capacitance inside the pixel; this is the relative integration time (referenced to 0.5s – the base of NEP); means integration after the LNA* (t_{int} = (int. time in sec)/0.5 sec; actually this is around 0.6 µs	η	*efficiency of summation (here ~0.81)*
		B	*bandwidth of the measurement*
f_s	*sampling frequency of the A/D converters*	T_0	*290 K*
P_{total}	*total noise power*	k_B	*Boltzmann constant*
N	*number of pixels in the array*	NF	*noise figure of the LNA*
M	*number of needed CS measurements; M ≈ 4s log(N),if the image is s-sparse (value for the whole image)*	S	*sample count (see def. in the text)*
fps	*image acquisition speed (frame per second)*	k	*number of pixel clusters*
M_{pc}	*number of needed CS measurements per cluster* (M_{pc} < N_{pc})	r	*number of A/D converters*
N_{pc}	*number of pixels per cluster (pixel cluster size)*	N_{cs}	*the average number of active pixels in CS patterns within* t_{int}

non-CS architecture	CS architecture	
Sensor SNR		
$SNR^{sensor} = \frac{1}{(P_{det}+P_{LNA})\frac{1}{t_{int}}\frac{N\,fps}{r\,fs}}$	$SNR_{cs}^{sensor} = \frac{(N_{cs}\eta)^2}{(N_{pc}P_{det}+P_{LNA})\frac{1}{t_{int}}\frac{M_{pc}}{N_{pc}}\frac{N fps}{r\,fs}}$	(45)
Pixel SNR		
$SNR^{px} = SNR^{sensor}$	$SNR_{cs}^{px} = \frac{\left(\frac{N_{cs}\eta}{N_{pc}}\right)^2}{\left(P_{det}+\frac{1}{N_{pc}}P_{LNA}\right)\frac{1}{t_{int}S}}$	(46)
Relative total noise power		
$P_{total} = (P_{det} + P_{LNA})\frac{1}{t_{int}S}$	$P_{total} = \left(P_{det} + \frac{1}{N_{pc}}P_{LNA}\right)\frac{N_{pc}M_{pc}N\,fps}{t_{int}\,r\,f_s\,(N_{cs}\eta)^2}$	(47)

Table 4 The performance comparison of a serial and a uniform detector architecture

However, due to the high noise level and the weak THz sources, frequency filtering is advisable that increases SNR with orders of magnitude. For this, I assume lock-in amplification with digital phase-sensitive detection (PSD) in the post-processing, so the source modulation frequency (f_{sm}) gives an upper bound for the integration time either way:

$$t_{int} \leq \frac{1}{2f_{sm}}. \tag{48}$$

I compare the serial, CS capable architecture to the non-serial, uniform array in Table 4. $P_{det} = \sqrt{B}\,NEP$ and $P_{LNA} \approx T_0 k_B B\left(10^{\frac{NF}{10}} - 1\right)$ stand for the noise power of a single detector and the LNA noise power, respectively. All the other notations are indicated in Table 4. I do not recommend in-pixel integration because of the limited space and the antenna clearance; furthermore, VLSI implementations prefer oversampling to in-pixel integration [17], [18] and loading effects also justify integration after the LNA. Thus, I consider integration only after the amplifier with an integration ratio (t_{int}) referenced to 0.5 s as I have mentioned above.

Our analysis assumes ideal signal transmission and multiplexing on both the CS and non-CS case. Hence, the sample count equals its upper limit:

DOI:10.15774/PPKE.ITK.2015.006

$$S = \frac{r\, f_s}{\frac{M_{pc}}{N_{pc}} N\, fps}, \tag{49}$$

where M_{pc} and N_{pc} are the number of pixels and needed measurements per cluster, respectively. By the non-CS architecture, these parameters equal to one. Considering averaging S has a direct effect on the SNR, likewise $\mathrm{t_{int}}$ and the gain of the Fast Fourier Transform (FFT) from the PSD depends similarly on the sample count:

$$FFT_{gain} = 10 \log\left(\frac{S}{2}\right) \text{[dB]}, \tag{50}$$

This approximation assumes a flat noise spectrum; however, the actual gain of the frequency filtering can be higher, due to the low frequency flicker noise terms and several artefacts at discrete frequencies.

In the first two rows of Table 4, the SNR of the measurement and the resulting pixels show up as 'sensor SNR' and 'pixel SNR', respectively. In the third row of Table 4, I give the general formula of the total noise power (P_{total}) considering all the losses by referencing it to unity signal power. Comparing the pixel SNRs, (46) involves the following inequality should hold to keep the pixel SNR of the serial array higher than that of a uniform array.

$$(P_{det} + P_{LNA})(N_{cs}\eta)^2 \geq \left(P_{det} + \frac{1}{N_{pc}} P_{LNA}\right) M_{pc} N_{pc} \tag{51}$$

Since our prototype fulfills the following condition,

$$(N_{cs}\eta)^2 \geq M_{pc} N_{pc} \tag{52}$$

the advantage of the CS architecture is obvious: it tolerates the LNA noise much better giving the same SNR even at an order of magnitude higher LNA noise power. Therefore, the achieved performance of our sensor would be greater than or equal that of a non-CS array with arbitrary P_{det}, P_{LNA}, t_{int}, N, fps, fs and $r < N/N_{pc}$.

Equation 47 shows that P_{total} is proportional to (N fps). Since N $\gg$ fps, N affects the most the performance of the read-out circuit at large array sizes. The proposed CS array has just a single output per a pixel bunch, thus it reduces the number of analog signals by a factor of $N_{pc} = 16$ facilitating the resource allocation.

If (52) does not hold than the CS architecture has advantage only if the ratio of P_{det} and P_{LNA} fulfills the inequality:

$$\frac{P_{LNA}}{P_{det}} > \frac{(N_{cs}\eta)^2 - N_{pc}M_{pc}}{M_{pc} - (N_{cs}\eta)^2}. \tag{53}$$

This assessment can be reformulated regarding the noise figure of the LNA:

DOI:10.15774/PPKE.ITK.2015.006

$$NF \geq 10\log\left(\frac{M_{pc}(N_{pc}-1)}{(N_{cs}\eta)^2-M_{pc}}\right). \tag{54}$$

The development of local oscillators promises heterodyne detection in a monolithic form. The much lower theoretical NEP values – on the order of 10^{-20} W/√Hz assuming a local oscillator power of 10 μW – will need new low noise solutions. The CS coarse grain architecture could be ideal for these scenarios. From this viewpoint, the above criterion has also much practical importance.

Not represented in the table, but the non-linear reconstruction also filters Gaussian noise to certain extent. Mainly the high frequency noise terms fall out during the sparsity driven optimization. Yet, by up-scaling and proper preconditioning, the gain of the non-linear reconstruction also increases with natural, structured images [41]. The signal is '*s*-sparse' if a basis exist in which all component of the signal vector is close to zero, but *s* element. Then, only *s·log(N/s)* measurement is enough to reconstruct the signal [16] (see details in section 1.2). These facts give the scalable nature of the architecture.

The SNR advantage of the CS solution takes the following form (in dB):

$$10\log\left(\frac{1+K}{1+\frac{K}{N_{pc}}}\frac{(N_{cs}\eta)^2}{M_{pc}N_{pc}}\right), \text{ where } K=\frac{P_{LNA}}{P_{det}}. \tag{55}$$

For the specification of the LNA it is important to express the relation of the architecture to the noise factor of the LNA (F_{LNA}).

$$K=\frac{P_{LNA}}{P_{det}}=F_{LNA}-1 \tag{56}$$

The advance can turned into SNR increase as depicted above; however, loosing the specification of the LNA or allowing greater detector noise could be also of practical importance. Therefore, I give also the other two extreme cases where the CS architecture would still provide the same performance as a uniform array: the advance in terms of the detector noise or the noise factor of the LNA.

$$P_{\text{det\_max}}=\frac{(N_{cs}\eta)^2}{M_{pc}\cdot\left(\frac{N_{pc}-1}{F}+1\right)}\,P_{det} \tag{57}$$

$$F_{\text{LNA\_max}}=(F_{LNA}-1)\cdot N_{pc}+1 \tag{58}$$

According to the above results (especially Table 4, (51), (52) and (55) I conclude to the following assessment:

DOI:10.15774/PPKE.ITK.2015.006

Serial, CS based THz FET detectors have advantage over uniform arrays

Thesis 2.1 *I have proved, that serially connected sensors are advantageous in VLSI implementations of FET based, integrated terahertz imagers if special conditions hold for the detector NEP and the noise figure of the integrated LNA.*

To exploit the statistical advantages of a greater image size, it is not necessary to increase further the size of the pixel cluster. The samples from the clusters can be summed up in different combinations during the post-processing to create greater data units for the reconstruction. Hence, the serial clusters can be inserted into conventional read-out organizations forming coarse-grain arrays and still preserving the potential statistical advantages.

An additional column of the table above can be the single pixel camera with a spatial light modulator (SLM). This is a promising approach, combining highly focused beam with multi-pixel sensing. It preserves the single pixel area and one can utilize a more bulky single detector with lower NEP. However, today state off the art SLMs suffer from cross talk, power loss, and frequency sensitivity.

The condition (52) means the actual performance of the array highly depends on the compression ratio and the accuracy of the algorithm that is the efficiency of the used reconstruction mechanism. Therefore, the evaluation of the CS solutions should include both the hardware and post-processing part and handle them as a whole.

3.3.1.1 Discussion

Serially connected architectures are not seem to be advantageous by themselves. However, if one combines this approach with the existing read-out organizations, it forms a coarse grain architecture that extend the possibilities of implementation: building larger arrays or increasing the image SNR.

This solution organizes the pixels of a regular array in serially connected, but individually controllable ‘clusters’ that provide a single, summed response of the constituting pixels. Hence, one performs a sequence of measurements with different pixel activation patterns to reconstruct the individual pixels of each cluster. This reduces the size and noise of the pixel level electronics and needed readout circuitry, whereas makes available the CS post-processing toolset. Table 5 presents the advantages and disadvantages of the solution in an outlined form (concerning our proof-of-concept chip specifics to match with the presented measurements in section 0).

If the compression ratio is above a given threshold, this coarse grain, CS architecture provides better performance regarding both speed and SNR – measurements in section 4.2 achieved this limit presented in section 3.3.1.

DOI:10.15774/PPKE.ITK.2015.006

Advantage	Disadvantage
Complex measurements can be done that can reduce the overall number of needed measurements (CS) and increase SNR through the noise suppression of the non-linear optimization based reconstruction. These advantages increase by scaling up.	At small size arrays (< 100 pixels), the advantage is smaller; the sample count reduction is 62.5% in the case of our prove-of-concept chip with one pixel cluster (16 pixels).
Only one low noise amplifier (LNA) needed per pixel cluster. Thus, the LNA noise contribution is far less than in the case of non-serial architectures and the needed area decreases significantly.	Additional binary switching circuitry needed for pattern generation (e.g. a shift register (SR) and a buffer on each bit to select between the two global reference voltages (on/off); but switches can be shared among several clusters)
It forms a coarse grain architecture that reduces spatial multiplexing 16 times and improves antenna clearance.	The additional serialization limits the maximal theoretical in-pixel integration time.

Table 5 Outline of the main properties of the complex sampling capable architecture

To achieve these ideal results one has to apply the "best" reconstruction algorithms. Since the image size is small, we have much more freedom in performing computationally intensive post-processing (like the proposed meta-algorithm in 0). However, solving the combinatorial problem is still too expensive with brute-force even for 8-bit four by four pixel images. Therefore, I suggest to reverse the problem: build application specific library from the images and apply a 2D, model based reconstruction. These problems are hard to solve, but tractable. Yet, the CS sensor can solve easily the library building task, because it is capable for normal single-pixel measurements at a lower speed. Hence, the initialization of the system would only require measurements with the very same configuration at a low speed. This enables high quality, low noise library data that is the essential prerequisite of good reconstruction performance.

3.3.2 Considerations on the implementation

Lisauskas in [10] investigated the effect of induced current on the detector noise and gave a theoretical upper bound on the achievable sensor SNR that increases at most to 1.35 times relative to the unbiased detector transistor. This advance should show up at subthreshold biasing and above the corner frequency of the excess noise. Nevertheless, there is no reported solution above 1 (attributing the effect to implementation losses (load) and altered noise sources). To summarize the effect: the signal level may grow significantly, but the noise increases at an even greater rate. (Resonant detection is also achievable in special cases; see [42] for a concise review.)

Later on, Földesy gave a new model for the in-circuit behavior of FET detectors [6] and proved that finite isolation between source and drain cause cross talk between the source-side and drain-side small signal response. Therefore, the measured value can be only smaller than that of the

DOI:10.15774/PPKE.ITK.2015.006

intrinsic open drain response and induced current does not affect this DC photoresponse (see (16) and (21) in [6]).

In spite of these facts, I have studied the characteristics of biased detection at CS based architectures and I have given general estimations on the current loss.

According to Földesy [6], the non-resonant FET detector works as a common-gate amplifier with a theoretical minimum noise factor (F_{det}) between 1.6 and 3 depending on the technology and the transistor parameters. That is, the bias current does not change the photoresponse at all, but additional current noise turns up resulting the reduced SNR of the amplified output. This enables to handle the detector on a similar way as the LNA and incorporate it in the previous model of CS based detectors. Hence, the SNR loss of the unchanged system (given in dB) will have the following form:

$$L\left(K, N_{pc}, F_{det}\right) = 10\log\left(\frac{\left(\frac{1}{K}F_{det}+F_{det}\right)\cdot N_{pc}+K+1}{\left(\frac{1}{K}F_{det}+1\right)\cdot N_{pc}+K+F_{det}}\cdot\left(1+\frac{\log k}{\log N_{pc}}\right)\right), \text{ where } K=\frac{P_{LNA}}{P_{det}} \quad (59)$$

If the noise figure is given, substitute $F_{det} = 10^{\frac{NF_{det}}{10}}$ in the above equation. Assuming $NF_{det} = 10\log(F_{\mathrm{det}}) = 10\log(3) = 4.77$ the SNR loss of current mode is:

$$L\left(K, N_{pc}, 3\right) = 10\log\left(\frac{3\mathrm{N_{pc}}+1+K_2}{\mathrm{N_{pc}}+3+K_2}\right), \text{ where } K_2=\frac{P_{LNA}}{P_{det}}+\frac{\left(3N_{pc}\cdot P_{det}\right)}{P_{LNA}} \quad (60)$$

The left side of Figure 34 visualize this 2D function to have some notion about its characteristic. The relevant part is $K \in (0,10)$ and $N_{pc} \in (10,10^2)$, where the loss is relatively small – see the right side of the figure, where the $N_{pc} = 16$ case is depicted.

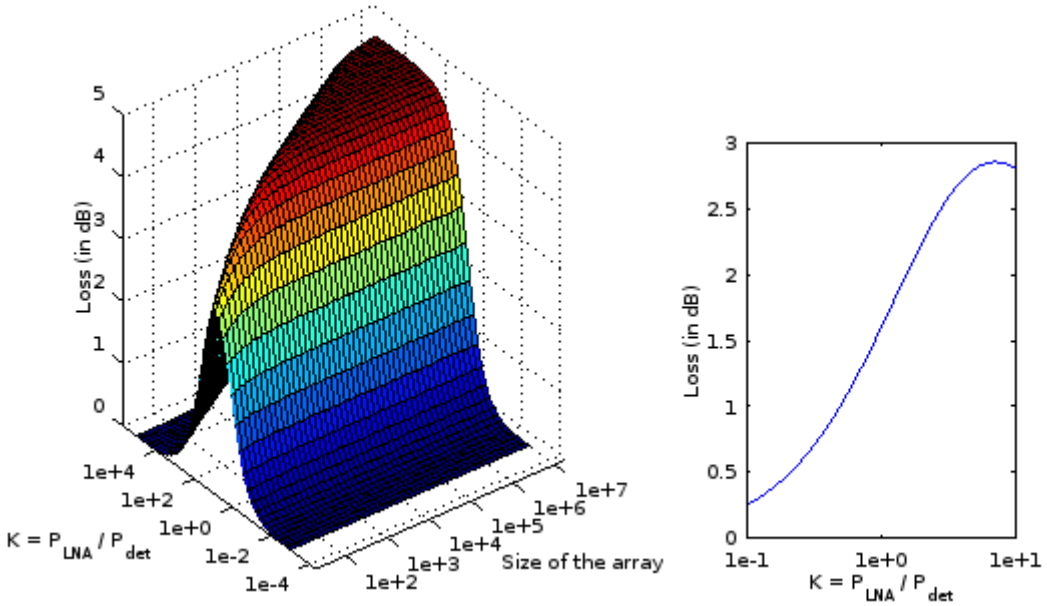

Figure 34 The SNR loss caused by the current mode in CS sensor arrays; without heterodyne detection $K < 1$

DOI:10.15774/PPKE.ITK.2015.006

The upper bound of the loss is

$$L(N_{pc}, F_{det}) \leq 10 \log\left(\frac{F_{det}\cdot N_{pc}+1+2\sqrt{F_{det}\cdot N_{pc}}}{N_{pc}+F_{det}+2\sqrt{F_{det}\cdot N_{pc}}}\right) \tag{61}$$

This bound gives a maximal loss of 2.79 dB for $F_{det} = 3$ and $N_{pc} = 16$.

The corner frequency of the flicker noise shifts to the MHz region in current mode. However, induced current allows higher modulation frequencies and can compensate for it. As proposed above, current mode reduces the losses of long serial chains, thus increases the efficiency of summation and allows greater CS arrays. (Increase of the array raises the current loss.)

Consider a CS array of greater size (N_{pc_2}) assuming that $M_{pc} = \mathrm{s} \cdot \log(N_{pc})$, then the general formula modifies to the following expression:

$$L(K, N_{pc}, F, k) = 10 \log\left(\frac{\left(\frac{1}{K}F+F\right)\cdot N_{pc_1}+\frac{K+1}{k}}{\left(\frac{1}{K}F+1\right)\cdot N_{pc_1}+K+F}\cdot\left(1+\frac{\log k}{\log N_{pc_1}}\right)\right),$$

$$\text{where } K = \frac{P_{LNA}}{P_{det}} \text{ and } k = \frac{N_{pc_2}}{N_{pc_1}} \tag{62}$$

If we substitute K with $(F_{LNA} - 1)$ we get a more pronounced formula.

$$L(F_{LNA}, F_{det}, N_{pc}, k) = 10 \log\left(\frac{\left(\frac{1}{F_{LNA}-1}+1\right)\cdot F_{det}N_{pc_1}+\frac{F_{LNA}}{k}}{\left(\frac{F_{det}}{F_{LNA}-1}+1\right)\cdot N_{pc_1}+F_{det}+F_{LNA}-1}\cdot\left(1+\frac{\log k}{\log N_{pc_1}}\right)\right),$$

$$\text{where } k = \frac{N_{pc_2}}{N_{pc_1}} \tag{63}$$

Equation 63 gives the exact SNR loss caused by the induced current, considering a *k*-times increase of the array size and could be used for evaluating an actual configuration. Increasing the size of the array do not imply an obvious SNR increase (the second term within the logarithm is slightly greater than one). It is also obvious that most of the cases the $F_{det}N_{pc_1}$ term will dominate the loss, but the relative tolerance of the LNA noise increases.

DOI:10.15774/PPKE.ITK.2015.006

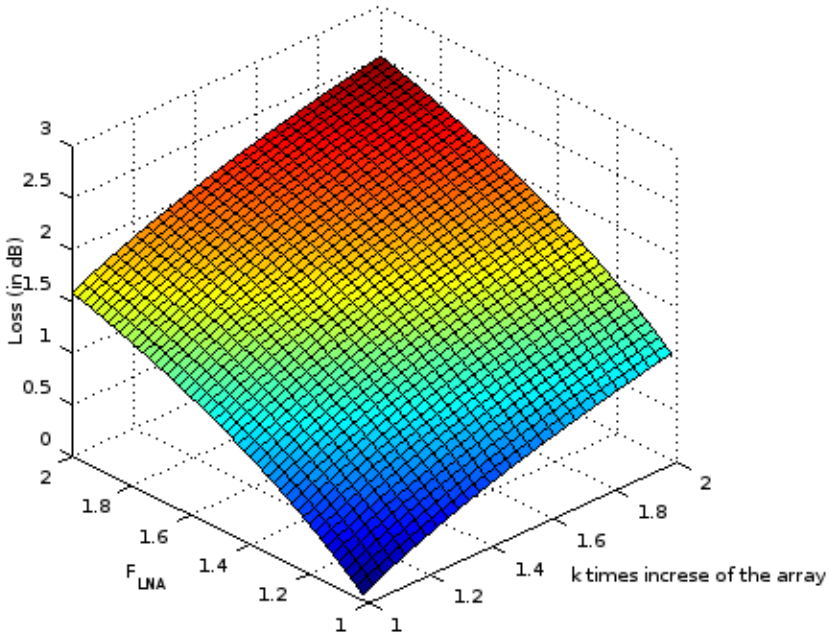

Figure 35 Equation 63 at low F_{LNA} values; $F_{LNA} = 3$, $N_{pc} = 16$; the current loss can be less than 15 %

The interesting case is when the low noise amplifier is very efficient for instance if $F_{LNA} = 1.2$ the loss is less than 13 %. The open drain efficiency of the summation (η) is only 0.8 and its expected improvement can balance the caused loss. According to the measurements of Elkhatib [30] summation efficiencies over 0.9 are achievable at appropriate gate-bias and load.
Based on these facts I conclude to the following thesis:

Induced current in integrated systems

Thesis 2.2 *I have proved that induced current can enhance overall system SNR in application oriented implementations of FET based FPAs.*

To give a sound picture, I also describe the simple, non-CS case, where induced current can result absolute SNR gain, if the performance of the integrated LNA is limited. We can get a practical lower bound on the detector gain G_1 by the noise factor of the system using (42).

$$F_{sys} = F_{det} + \frac{F_{LNA}-1}{G_{det}} \tag{64}$$

Hence, the degradation of the system SNR can be balanced by the gain of the detector – working as a common gate amplifier – if the gain fulfills the following inequality:

$$G'_{det} > \frac{F_{LNA}-1}{F_{LNA}-F'_{\mathrm{det}}}\text{, and assuming} \tag{65}$$

$$F'_{\mathrm{det}} < \frac{F_{LNA}-1}{G_{det}} + F_{det}\ , \tag{66}$$

that means cases, where the LNA is high relative to the detector noise:

$$G'_{det}(F'_{\mathrm{det}} - F_{\mathrm{det}})\ + 1 < F_{LNA}\ . \tag{67}$$

DOI:10.15774/PPKE.ITK.2015.006

where F'_{det} is the noise factor of the detector in current mode. Actually, if $F'_{\mathrm{det}} = 3$, then G'_{det} should obey the rule to achieve an absolute SNR increase:

$$G'_{\mathrm{det}} > \frac{F_{LNA}-1}{F_{LNA}-3} \text{ assuming that } F_{LNA} > 2G'_{\mathrm{det}} + 1. \tag{68}$$

The lower bound of the gain, where current mode results an absolute SNR increase shows up in Figure 36 without considering condition (66).

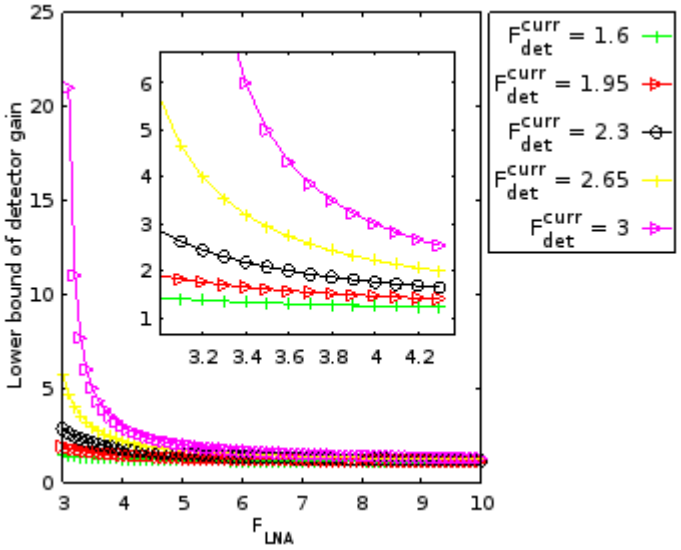

Figure 36 The lower bound of the detector gain, where current mode yields increase of the SNR, without condition (66); this advantage depends on F_{LNA} and of course, on F'_{det} itself; $F'_{det} = F^{curr}_{det}$ in the figure; Note: 1) a common gate amplification around thirteen is plausible 2) there is another linear criterion

I repeat the small signal amplification of a terahertz detector in common gate amplifier configuration from [6]:

$$G'_{det} = -\frac{(g_{ds}+g_m)Z_{load}}{1+g_{ds}Z_{load}}. \tag{69}$$

The irradiation that couples to the drain will slightly decrease the response, but we can use the following simple lower bound to incorporate this effect.

$$G'_{det} \geq \frac{(g_{ds}+g_m)Z_{load}}{1+g_{ds}Z_{load}} - 1\,, \tag{70}$$

where the channel conductance, transconductance, and the total load of the read-out circuit are treatable design parameters.

In the end, we arrive to the fact that current mode can result higher SNR in the non-CS case in special cases dependent on design choices like F_{LNA} and G'_{det}. The condition of the SNR gain is the following:

DOI:10.15774/PPKE.ITK.2015.006

$$\begin{cases} if\ 0 < G'_{det} < 1\ (lossy\ conf.)\ and\ 3 + \frac{2}{G'_{det}-1} < F_{LNA} < F'_{\mathrm{det}} \\ if\ 1 < G'_{det} < 2\ and\ 3 + \frac{2}{G'_{det}-1} < F_{LNA} \\ if\ 2 < G'_{det}\ and\ 2G'_{det} + 1 < F_{LNA} \end{cases} \tag{71}$$

In addition, current mode helps the system integration of the THz FET based FPAs. Greater drain current strengthens the driving capability of the detector allowing higher input load from the read-out circuitry. Eventually, it enables higher modulation frequency and increases the signal level, what can make the LNA implementation easier. The current mode sensor tolerates the environmental noises better, although, the corner frequency of its own flicker noise rises from a few kHz towards the MHz region.

Biased serial pixel blocks promise to cancel the losses caused by the loading effects and enable greater pixel clusters. With this, current mode can further reduce the number of LNAs, the LNA noise contribution and enhance the compression ratio.

Since, design and manufacturing costs restrict the area, technology, and design complexity there could be several suboptimal design choice from the viewpoint of the final performance. In these cases, induced current may also enhance the output SNR. Parameter sweeps with our detector support these findings.

Anyway, there is strong dependency among these parameters: gate voltages, modulation frequency, induced current, array size and pitch, minimal step of raster scanning. Thus, they cannot be tuned independently. This is why I suggest optimizing these values on a holistic way, starting at the design phase of the detector array.

Since different design goals (cost, time, easy system integration and reliability) enforce several suboptimal design choice from the point of the final performance, induced current may enhance the output SNR. Parameter sweeps with our detector support these findings.

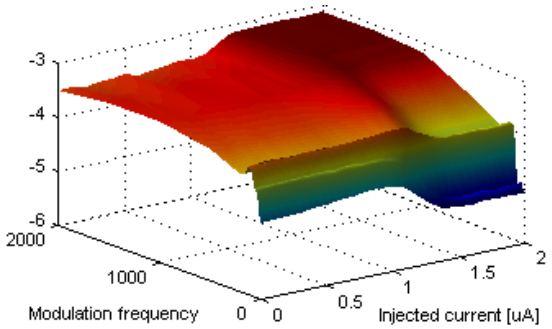

Fig. 6 SNR of the detector [dB] at U_{gs} = 0.75 V gate voltage

Fig 6 shows the dependence of the SNR on the modulation frequency and the injected current at a constant U_{gs} = 0.75 V and U_s connected to ground. It shows that in the given setup (single antenna coupled Si MOS FET with antenna connections on the source and the gate irradiated at 360 GHz frequency, LNA with a noise figure of about 3) the injected current increase the overall SNR of the system. This figure is based on the raw data, acquired by the DAQ card.

DOI:10.15774/PPKE.ITK.2015.006

3.3.2.1 Reconstruction on extremely small images

By the proposed realization of CS measurements, the size of the pattern generator block is limited. Restricting the number of the different patterns per pixel cluster is also desirable to decrease the complexity of the auxiliary electronics. The effect can be enhanced, if the reduced set of patterns can be used uniformly on the entire array.

3.3.2.2 The effect of the CS measurement scheme on the A/D conversion

To evaluate the effect of the CS architecture on the bit depth of the A/D converters, I assumed that at most $\sqrt{N}$ A/D converters gather samples in a time multiplexed fashion on the chip.

A drawback of the CS measurements from digitalization point of view they require $N_{cs}\eta$ times higher dynamical range. Therefore, maintaining the same precision would need with $\log_2(N_{cs}\eta)$ bits higher bit-depth A/D converters. (However, the minimal received signal level also increases shrinking the actually utilized dynamical range.)

For instance, an 8 bit pixel representation on a uniform array would demand $D_{bit} \approx 8 + \log_2(N_{cs}\eta)$ bits on the CS array ($\eta \approx 0.8$, $\frac{N_{cs}}{N} \approx 0.75$).

Since N_{cs} is small in the proposed coarse grain arrays (~12) extreme bit depths are not needed; actually the 8 bit depth grows to 11 bits. The fix measurement patterns can only slightly improve on this.

Simulations on natural images support the viability of simple approximations, like a test set based average dynamical range that provides acceptable performance.

In practice, the real dynamical range of the sensors is not utilized, as the problem is the weak signal. That is, the biological and diagnostic targets are quite similar in having high attenuation factor at these frequencies. Therefore, sensing little changes in refractive index (in attenuation factor) is even harder and the bottleneck of the system will be the detectivity and sensitivity of the sensors. Thus, both reflective and transmissive THz images have usually low contrast, hardly utilizing 8-10 bits. This can be interpreted as the CS measurement scheme helps to exploit more the dynamical range of the sensors and utilizes the "spare bits of the A/Ds" if any left in the architecture or it needs only moderately higher A/Ds.

3.3.2.3 Information stream of the sensors

The efficiency of the sensors regarding the total received information per second depends on the SNR of the sensors and on the relation of the image and the measurement scheme. The SNR determines the amount of information that a single measurement could provide, however this value is affected by the correlation among the pixels within a frame and between consecutive frames. That is, finally, the entropy of the gathered sample set ($Ent(D)$) – considering multiple images or a set of linear measurements belonging to a single frame – will determine the gathered information (I). This involves the SNR (not given in dB) of the single measurements in the

DOI:10.15774/PPKE.ITK.2015.006

constituting probabilities (P_i) by guiding the quantization – increased dynamical range with the maintained precision; $i = 1, \dots, \lfloor SNR \rfloor$.

$$I = Ent(D) \cdot |D| \tag{72}$$

$$Ent(D) = -\sum_{i=1}^{\lfloor SNR \rfloor} -p_i \cdot \log p_i \tag{73}$$

where D is the data set and $|D|$ indicates the cardinality of this set. P_i is approximated with the frequency of an item (x) in the set (D). Here, the SNR is given as a pure intensity ratio or the square root of a power ratio.

At this point, I consider entropy only within single images; however, entropy decreases significantly in video recording. If the change is small on consecutive images (that is the difference image is sparse), the CS-framework is inherently capable to efficiently handle the stream – even providing a new frame at every single measurement. Therefore, this scenario increases the advantages much.

Nevertheless, at real applications, the emphasis is on improving the quality of still pictures (and depth of sensing), therefore I investigated the entropy of bit streams resulting from a single frame.

Due to the increased dynamical range and the spatially distributed measurements, the entropy of the CS measurements is usually higher than that of a uniform array. My simulations showed (14 test images in more than 100 different variations, in sizes from 16 to $2.5 \cdot 10^3$ pixels) that the CS measurements had approximately 25-30 % higher entropy, although, at the smallest size this advantage doesn't show up (See Figure 37 to have an insight of the characteristics).

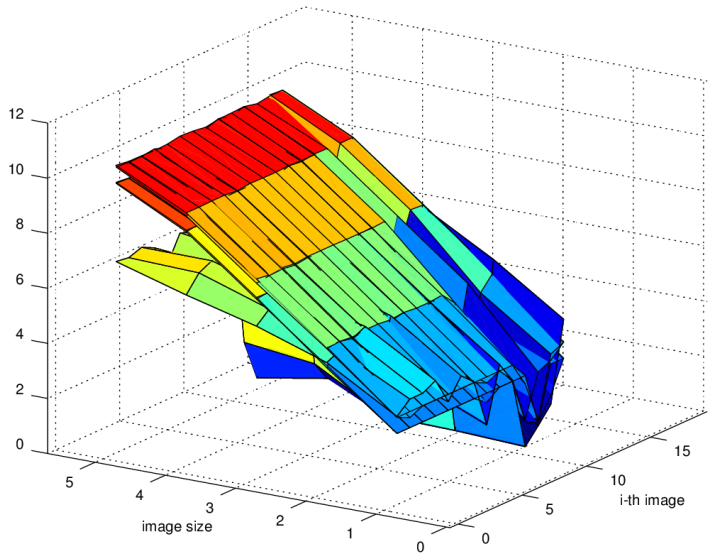

Figure 37 The entropy of normal and compressed sampling based measurements at different image size and test image; size is given in 10^x pixels; the z-axis gives the entropy of a single measurement in bits; the y-axis lists the indexes of the 8-bit, gray scale images: 1-10 natural images; 11-13 sparse images; 14 random image; the higher surfaces belong to the linear measurements at different pixel correlation levels

DOI:10.15774/PPKE.ITK.2015.006

– small, but consistent difference; as expected the CS measurements have much higher entropy by "sparse" images

I expect a further, significant increase of relative entropy by video recording at fixed background.

The limit of CS reconstructions whose optimization is driven by relaxed goal functions: they are only effective, when applied to images that have only comparable amount of information to the entropy of the measurement data stream or less.

I also note here, that I prefer the use of entropy to characterize the target scene from the viewpoint of sparsity, because it is independent from the chosen basis ($\boldsymbol{\Psi}$). However, the entropy depends on the quantization. Thus, one has to pay attention to be consequent by its usage.

3.4 Related problems

3.4.1 The problem of the optical setup

The optical setup also has great impact on the performance. My conclusion is shortening of the optical path and reducing the number of constituting elements may be advantageous. For this, lens free configurations (Fourier imaging, holography) are also worth to consider. Although, this technique would need the extension of the sensitive area to several square centimeters that significantly reduce the signal power intensity. One should consider scanning or utilizing multiple detector chips. As the mass production of such chips is not expensive, the latter solution is viable.

3.4.2 Raster scanning on non-uniform grids

There is often need to investigate a greater area of several square centimeters with the maximum achievable resolution e.g. inspection of human tissue. Keeping this example, at least a 1.5 cm × 1.5 cm^2 screen size has to be considered to unveil the penetration margins of a melanoma under the surface. For this, one has to perform a 2D scan with the available detector. As the resolution and frequency increases, the relative efficiency of the embedded antennas decreases (see the beginning of section 3.1.2). One option is to use oversized pixels (antennas with greater effective length). If scanning is an inherent part of the system, we can use greater pixels of size $0.5k\lambda$, $k = 1,2,3, \ldots$. With that, we can avoid the low efficiency of small antennas at frequencies in the 0.5-1 THz range. (For instance, antennas working at 460 GHz with 2.2 mm pitch size.)

For this, I suggest the idea of converting the multi-pixel sensing of the detectors into resolution increasing with overlapping scanning. According to this, we use imperfect grids with near-optimal step sizes for determining the measurement locations. With this, one can have greater resolution at the cost of overlapping scan positions, but still maximizing the step size to reduce the acquisition time.

DOI:10.15774/PPKE.ITK.2015.006

I give here three conditions for determining a near-optimal step size (s), given an actual detector (number of detector pixels (k_x, k_y), pitch size (p_x, p_y) both in the horizontal and vertical direction).

1. Ensuring there is no redundant measurement:

$$mod(p,s) > 0 \tag{74}$$

2. Sampling precision within a step size is smaller than a

$$mod\big(s, mod(p,s)\big) < a \tag{75}$$

3. (Virtually) extended detector with b more rows (y) or columns (x)

$$\left|\frac{s}{mod(p,s)} - k_x\right| < b \tag{76}$$

Then, finding a near-optimal step size is easy by choosing the appropriate additional conditions. For instance to get a near-optimal maximal lateral resolution at 2200 μm pitch size for a four by four pixel array – maximizing also the step size to maintain speed:

$$\max_s(resolution)\ such\ that\ \max(s), a = 1\ and\ b = 0 \tag{77}$$

We get 1760 µm for the near-optimal step size that will provide 240 µm resolution with only a few tens of µm error.

If the needed precision is beyond the full width at half maximum (FWHM) of the focused beam, then the result should be deconvolved with the point spread function (PSF) of the optical system. With this, we can get a kind of 'superresolution' image. Of course, oversampling the image with smaller resolution than half the wavelength is not advantageous.

By reflective imaging of greater, cylindrical objects (e.g. parts of the body) silicon lenses may be inappropriate to collect the reflected signal. Utilizing a great, flexible THz array with oversized, efficient antennas could be a cost effective alternative. The array of several centimeter size could be assembled easily from individual chips placed on a flexible printed circuit board (PCB) resulting in a huge pitch. In this case, the scanning of the great area would need only the small displacement of the whole array around its center position to increase the resolution to the level of a single chip, dense FPA. The scanning time also could be reduced with the proposed optimization.

3.4.3 Depth of sensing

I continue the considerations from section 2.1 and analyze the depth of sensing in relation with the imaging system.

$$z = \frac{1}{2\alpha}\ln\left(\frac{P_{source}}{\sqrt{B}\cdot NEP\cdot SNR}\right), \tag{78}$$

DOI:10.15774/PPKE.ITK.2015.006

where the required SNR is approximated with the inverse of the normalized detectability of the system. Hence, in our case it takes the form

$$z = \frac{1}{2}\frac{1}{200}\ln\left(\frac{100\cdot10^{-6}}{\sqrt{10}\cdot20\cdot10^{-12}\cdot100}\right) \approx 241\ [\mu\text{m}], \tag{79}$$

Based on measurements of the noise floor we got comparable results. The actual source output power is 102 μW at 460 GHz (and the sensor array has 200 kV/W responsivity); the limit of detectability showed up around 6 nW per pixel at 0.1 s integration (serial structure). This enables only

$$z = \frac{1}{2}\frac{1}{200}\ln\left(\frac{100\cdot10^{-6}}{6\cdot10^{-9}\cdot100}\right) \approx 128\ [\mu\text{m}], \tag{80}$$

inspection depth with approximately 84 dB SNR, if the beam is perfectly focused on a single pixel. The depth takes the following form, when expressed with the noise power of the detector and noise figure of the LNA:

$$z = \frac{1}{2\alpha}\ln\left(\frac{P_{source}}{P_{det}\cdot10^{\frac{NF}{10}}\cdot SNR}\right), \tag{81}$$

DOI:10.15774/PPKE.ITK.2015.006

4 EXPERIMENTAL VALIDATION - MEASUREMENTS

To determine the radiation pattern of the antennas the measurement data should be deconvolved with an estimated source beam. For the beam estimation I used simple sphere model concerning the utilized horn antenna on the AMC. The operation is performed as customary in the frequency domain.

4.1 Targeted diagnostic usage

Used frequencies (GHz): 325.2, 354.8, 393.8 (depicted on Figure 38.)

Measurement configuration: intensity registration on a reflective way.

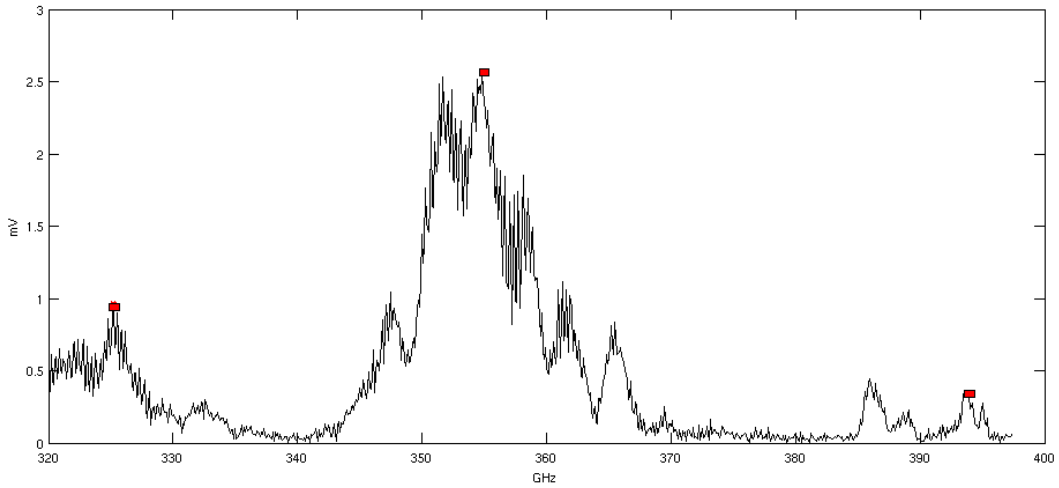

Figure 38 Frequency response of the used detector in a reflective setup. Only three measurement frequencies were selected for scanning to reduce acquisition time.

Water has very high absorption at specific frequencies. The lowest absorption peak is around 550GHz. Hence, in reflective setup water concentration changes can be registered confidently. We used frequencies below 500GHz, with much smaller absorption coefficient that allowed registering concentration changes in thicker samples. Cancerous skin areas often show increased water concentration (e.g. in the case of superficial basal cell carcinoma or squamous cell carcinoma [1]).

In vivo skin water concentration changes person by person: according to skin type, sustained stress and actual status (daily biorhythm). Moreover skin structure (thickness of different layers) changes according to skin area (placement on the body) as well. For that reason local contrast of absorption intensity can be used to distinguish between healthy and diseased skin areas [2].

To this end in vivo measurements should be carried out involving both diseased tissue and its broader surroundings. (As a compromise, measurements can be done on animals or on slightly affected in vitro skin samples as well.)

DOI:10.15774/PPKE.ITK.2015.006

4.1.1 Water concentration

The achievable sensitivity in water concentration directly indicates the suitability of the setup for water content based classification of tissues. I carried out direct water content measurements on paper samples of different thickness. Such results can be seen in Figure 39. Here, the thickness of the wet paper sheet provided the ground for comparison. This way approximate accuracy could be determined.

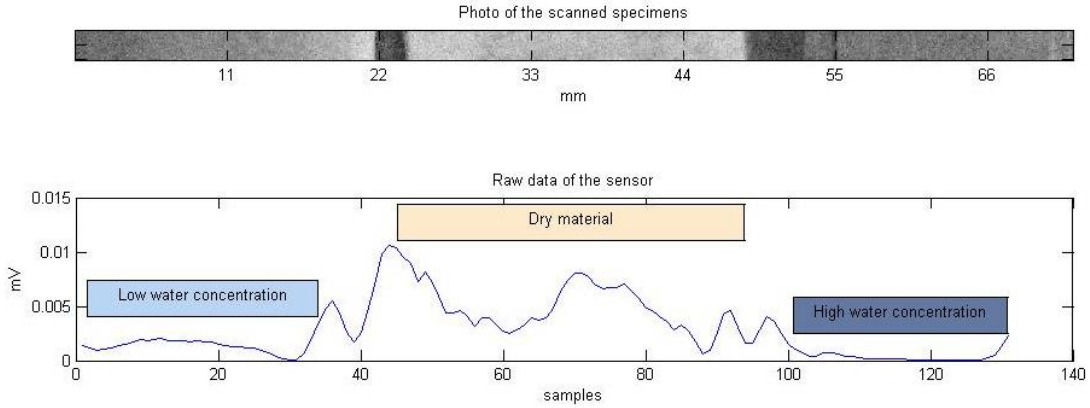

Figure 39 Direct water 'concentration' measurements on paper samples; The concentrations are the followings from the left: moderate (1 unit), low (dry sheet), high (2 unit); indicated in discrete units: number of paper sheets on top of each other. These samples were covered with plastic 1 mm thick plastic plate to ensure flat surface. At certain points of the plate and at the edges of the different specimens distortions can be observed (slight bending of the plate, changes in depth and contaminations); the figure shows raw sensor data.

4.1.2 Ex-vivo investigation of human tissue

We performed measurements on samples that differ from the original target of the above mentioned examination. Three cancerous tissue samples were examined, that were cut out from patients 3-4 days before the examination. These columnar structures consist of an overgrown tumorous skin tissue and several deeper layers of the skin.

The specimens were conserved in formalin that changed their natural water concentration. However, after cut-out the inter- and intracellular water concentration ratio changes fast and shriveling starts by all means.

The samples were placed in a coplanar plastic structure to ensure smoothed surface. Raster scanning was performed with 0.2, 0.3, and 0.5 mm precision respectively. Due to the course of the measurement, differentiation among the tissue types was not possible. However, inhomogeneities caused by the sponging of the specimens and irregular depletion of water were detected. These results can be seen in Fig. 2. Tissue specificity of the different frequencies were not significant in the actual range.

DOI:10.15774/PPKE.ITK.2015.006

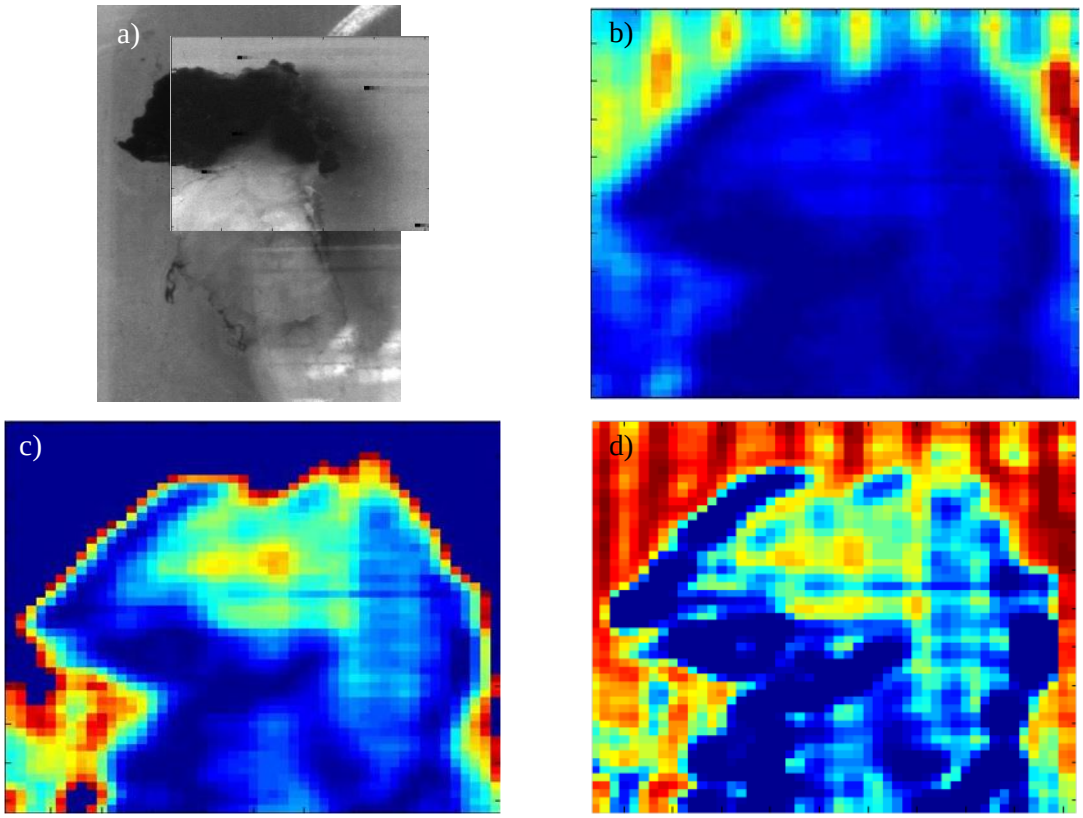

Figure 40 a) Gray color photo of the sample; b) Normalized intensity image at 354.8 GHz with 0.2 mm precision along "x" and "y" dimensions; c) and d) Normalizations within the range of the specimen.

We concluded that additional trials should be carried out in order to prove the applicability of the current sensor and measurement configuration for such diagnostic classification. Those tests should be performed on samples that have greater lateral extension, and on which local contrast changes of both healthy and diseased tissue can be registered.

4.1.2.1 Conclusions

As the main result of these measurements, I could identify the most important technical problems:

- The surface roughness of the observed objects should be handled at reflective measurements, because it makes the measurements unreliable. – Continuous repositioning of the target to find the maximal reflected signal at every point partly mitigates the problem in the case of point scanning.
- The coherence of the source should be eliminated, because subtle changes in the setup can alter the recorded intensity by more than 50%. For instance, the changing of the sample to another one or the slight excursions during in-vivo measurements cause disturbances. – One solution is the application of a diffusor plate (a moving or rotating diffusor plate is significantly better due to the smoother time average of the samples - suggested by Péter Földesy).

DOI:10.15774/PPKE.ITK.2015.006

- The waveguide based source has sharp peaks in its frequency spectrum and the device has considerable frequency offset error that must be canceled in order to produce comparable measurements. Péter Földesy supported this uncertainty of the recorded spectra with several frequency sweeps utilizing the Ericsson power meter.

4.2 Imaging of phantoms and test objects

In Fig. 11 and in Fig. 12 two CS measurements can be seen. The first image shows a part of phantom: the edge of a metal coin between two gummed paper sheets. The size of the captured image is 36x68 pixels (7.92 × 14.96 mm). It covers the central part of the coin that takes place on the right side of the scene.

The image was created with the 4x4-pixel serially connected array fixed on a moving stage. This way, we have simulated a 'virtual' detector of size 36x68 pixels. The pitch is 220µm in both dimensions, thus the chip had to be moved with a raster step size of 880 µm. In each position six measurements was made with different random patterns. From this data of the 4x4-pixel tiles a full frame image was reconstructed. Then, we have removed the fix pattern noise of the array and that of the reconstruction algorithm itself. However, increasing the image size the quality also improves without the need for increasing cluster size further.

We calculated the incident source power based on a beam scan at 10 cm distance. Assuming ideal positioning of the object, we have selected the area that equals the image size by thresholding the intensity recording. Then, the incident power is the integral of the intensity on the scanned area over that on the full recording (2 cm × 2 cm) multiplied by the total output power of the source.

Hence, the illuminating total source power was less than 46 µW at 459.9 GHz that spread over the surface of the phantom object. The noise floor was about 0.2 mV; the two paper sheets were not straight and the glue has strengthened the dispersion (the average attenuation was 36.5%). This caused low contrast at some parts on the left part of the image at the resulting average incident power of 11.9 nW per pixel (0.048 mm^2). The total integration time was 0.6 s for reconstructing the 16 pixels (performing a single measurement with one random pattern took 0.1 s). The contrast is still enough to notice the edge of the coin inside the phantom.

DOI:10.15774/PPKE.ITK.2015.006

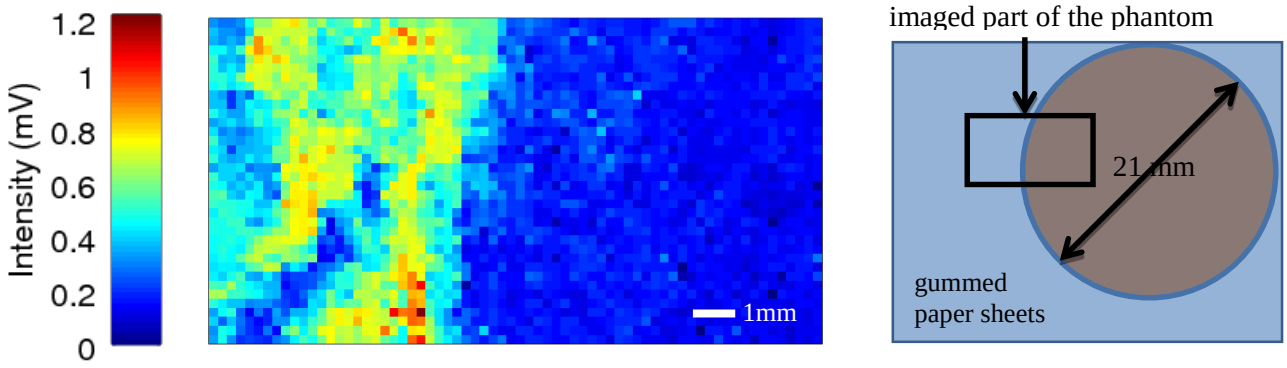

Figure 41 36x68 pixels image of a phantom acquired with CS technique

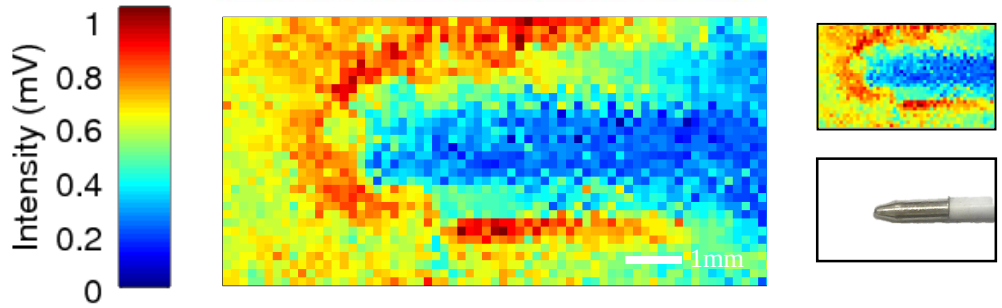

Figure 42 32x60 pixels CS image of the tip of a bedpan

The second image was created on the same way; it shows the tip of a bedpan (Fig. 12). The image size changed to 32x60 pixels (7.04x12.32mm). The metal tip of the bedpan was 2.2mm thick around which the diffraction patterns are also clearly visible.

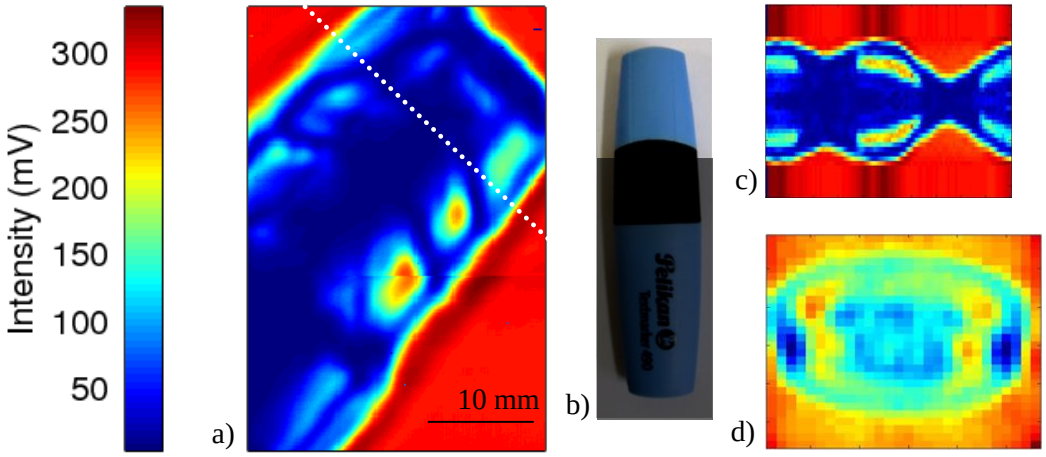

Figure 43 2D raster scanned image with full averaging (a) and cross-section (d) of a felt-tip pen (belonging photo (b) and sinogram (c) are also included)

Imaging of plastics and composite materials is a promising application area of terahertz technology [38]. Hence, we have selected a felt-tip pen for non-CS, raster scan imaging test at 459.2 GHz frequency. The step size was 100 µm; all detectors were active and no post-processing was applied on the image except the intensity normalization. Fig. 13 presents these results. The pen was rotated nearly 15 degrees about its longitudinal axis and tilted with 50

DOI:10.15774/PPKE.ITK.2015.006

degrees relative to the vertical axis. We have also captured a cross sectional image in the same way (all detectors on, no sub-image reconstruction). The object was rotated by 3.6-degree steps; the dotted line in Fig. 13 Part A shows the cutting plane.

DOI:10.15774/PPKE.ITK.2015.006

5 FIELDS OF APPLICATION

The results of thesis one can be applied for any CS based post-processing scheme, where small size, moderately structured, noisy images are to be reconstructed. Integrated FET based terahertz imaging is of this kind, especially, because the sensing is SNR critical and computationally expensive post-processing is acceptable.

Thesis two focuses on the overall performance of integrated arrays and helps the design of CS based terahertz focal plane arrays. It gives a guideline to determine the specifics of the built in LNA, exhibits the effect of a chosen read-out organization, and makes easier to calculate the achievable image SNR with a given configuration. It reveals the advantages of CS architectures and delimit the parameter region, where it is applicable.

The main bottleneck of today FET based systems is the SNR. With the development of local oscillators, the SNR of the detection is going to increase orders of magnitude. Therefore, the low noise system integration becomes an unavoidable question in the near future.

Another area where the results can be directly used is the evaluation of SLMs. Several approaches are developing (see section 1.3.1) and these emerging technologies promise the capability for single pixel imaging.

The results implies that the application of the CS technique on a higher level of the detection system would be another interesting point that would have applications in other frequency domains as well.

DOI:10.15774/PPKE.ITK.2015.006

6 SUMMARY

Terahertz sensing is a relatively new modality in medicine. Its clinical usage started in July 2012 by inspecting specific cancer diseases of dermal origin [1]. Terahertz imaging still has a long way to go to become an accepted technique in diagnostics. The possible applications require the fast observation of large areas with high sensitivity. For this, the large-scale integration and the overall noise suppression of the measurement system are indispensable.

In the Institute for Computer Science and Control of the HAS, research on CMOS based terahertz sensors has been carried out since 2008. Room temperature, antenna coupled, FET plasma wave detectors were in the focus of the research project I got the chance to join in 2009. With my work, I target the above-mentioned questions – scalability and overall system performance – by studying sensing in a holistic, application oriented manner: I consider the integrated focal plane antenna array, the detectors, the read-out circuitry and the post-processing as a whole.

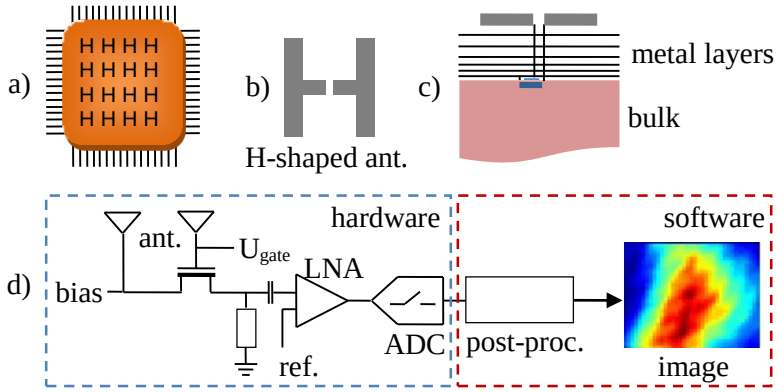

Figure 44 The study covers some parts of both the hardware (architecture of the antenna array, read-out organization) and the software (post-processing, image reconstruction); a) focal plane antenna array with the detectors; b) top view of a single antenna; c) cross section of the chip (antenna at the top and the MOS FET detector in the middle); d) the scheme of the studied system (considering a single detector element) – the components are represented with appropriate noise models to be able to handle them together, in a holistic way to evaluate design choices on a quantitative base

Fig 1 shows two simple experimental measurement setup and Fig 2 depicts the main components of the system that were modeled together primarily from the aspect of their noise performance. On the immature field of terahertz VLSI sensors, many design choices are being made according to intuitive considerations, starting from individually optimized components. However, several design choices have an indirect effect on the overall system performance; therefore, a kind of global, system wide optimization would be advantageous. In most of the systems, it is still impossible, because there is too much freedom in design choices and parameters.

In the presented holistic approach, I restricted the modeling according to the demands of the target applications. The figure of merit of the system was the SNR (and L_1 norm) of the resulting image. My primary aim was to investigate the performance of compressed sensing based

DOI:10.15774/PPKE.ITK.2015.006

detector organizations against the regular ones. For this, I utilized the simplest models of the touched components in order to tackle the problem quantitatively.

In the end, my answers help to find optimal solutions within the modeled framework and help the VLSI designers to evaluate their decisions directly from the aspect of the resulting image SNR of the system.

DOI:10.15774/PPKE.ITK.2015.006

7 ACKNOWLEDGEMENTS

I am grateful to many who accompanied my way. I list just a few of them, mentioning only one remarkable point regarding each person I have to thank; or I only allude to something I got. My short list starts with people from the academic environment: Tamás Roska inspired me many times; Péter Szolgay encouraged me whenever I met him; Judit Nyékyné Gaizler for giving me chance at important moments; Árpád Csurgay because of his professional courses; Judit Mikesy and Tivadarné Vida for their kind help.

Ádám Rák for the interesting talks; all members of the room 224 for the friendly atmosphere (András Horváth, Attila Stubendek, Gábor Tornai, Mihály Radványi, Miklós Koller, Tamás Fülöp and Tamás Zsedrovits);

Péter Földesy for the chance to join his group and showing me what exploratory research really is; all the 6 years; Ákos Zarándy for giving the possibility to stay at the ICSC and motivating me to complete my thesis; my colleagues Balázs Wittner, Borbála Pencz, Csaba Füzy, László Orzó, Márton Kiss and Zoltán Kárász for the conversations and enthusiastic explanations.

I am grateful to Adrienn Marschal for believing in my success and to Bence Gergelyi and Katalin Vájer for connecting me with the real word during this undertake. I have to thank Ágota Laskai and Roland Laskai for showing me, how fruitful diligence and responsibility can be. I thank my father, József Gergelyi that he taught me the consequent engineering thinking and demonstrated me if something seems to be impossible, you just may need to will stronger. At last, but not least, I thank my mother, Rita Tóth Gergelyiné, who created the peace around us and set an exceptional example of initiative will. Their outstanding work, the support of the family, was an invaluable driving force.

DOI:10.15774/PPKE.ITK.2015.006

8 AUTHOR'S PUBLICATIONS

[A1] **D. Gergelyi** and P. Földesy, "Digital Micromirror Device (DMD) projector based test bench for vision chips," in *Cellular Nanoscale Networks and Their Applications (CNNA), 2010 12th IEEE International Conference On*, Berkeley, CA, 2010.

[A2] **D. Gergelyi**, P. Földesy and Á. Zarándy, "Scalable, Low-Noise Architecture for Integrated Terahertz Imagers," *Journal of Infrared, Millimeter, and Terahertz Waves*, vol. 36, no. 6, pp. 520-536.

[A3] P. Földesy and **D. Gergelyi**, "Serially connected MOS terahertz sensor array," in *Infrared millimeter and terahertz waves (IRMMW), International Conference on*, Mainz, 2013.

[A4] P. Földesy, Z. Fekete, T. Pardy and **D. Gergelyi**, "Terahertz Spatial Light Modulator with Digital Microfluidic Array," in *26th Eurosensors Conference, appears in Journal of Procedia Engineering*, Kraków, 2012.

[A5] P. Földesy, **D. Gergelyi**, C. Füzy and G. Károlyi, "Test and configuration architecture of a subthz cmos detector array," in *Design and Diagnostics of Electronic Circuits and Systems (DDECS), 2012 IEEE 15th Symposium on*, Tallin, 2012.

[A6] G. Károlyi, **D. Gergelyi** and P. Földesy, "Sub-Thz Sensor Array with Embedded Signal Processing in 90nm CMOS Technology," *Sensors Journal, IEEE*, vol. PP, no. 99, pp. 1-1, 2013.

DOI:10.15774/PPKE.ITK.2015.006

9 REFERENCES

[1] S. M. P. a. D. D. Arnone, TeraView, 8 2012. [Online]. Available: http://www.teraview.com/news/terahertz-news/TeraView-receives-in-vivo-trials-approval.html. [Accessed 9 2014].

[2] D. Gergelyi, P. Földesy and Á. Zarándy, "Scalable, Low-Noise Architecture for Integrated Terahertz Imagers," *Journal of Infrared, Millimeter, and Terahertz Waves,* vol. 36, no. 6, pp. 520-536, 2015.

[3] P. H. Siegel, "Terahertz Pioneers: Manfred Winnewisser and Brenda Pruden Winnewisser: "Equating Hamiltonians to nature"," *Terahertz Science and Technology, IEEE Transactions on,* vol. 3, no. 3, pp. 229-236, May 2013.

[4] H. Lui, J. Zhao, D. McLean and H. Zeng, "Real-time Raman spectroscopy for in vivo skin cancer diagnosis," *Cancer research,* vol. 72, no. 10, pp. 2491--2500, 2012.

[5] D. Veksler, F. Teppe, A. Dmitriev, V. Y. Kachorovskii, W. Knap and M. Shur, "Detection of terahertz radiation in gated two-dimensional structures governed by dc current," *Physical Review B,* vol. 73, no. 12, p. 125328, 2006.

[6] P. Földesy, "Terahertz responsivity of field-effect transistors under arbitrary biasing conditions," *Journal of Applied Physics,* vol. 114, no. 11, pp. -, 2013.

[7] H. Sherry, J. Grzyb, Y. Zhao, R. Al Hadi, A. Cathelin, A. Kaiser and U. Pfeiffer, "A 1kpixel CMOS camera chip for 25fps real-time terahertz imaging applications," in *Solid-State Circuits Conference Digest of Technical Papers (ISSCC), 2012 IEEE International*, 2012.

[8] S. Preu, S. Kim, R. Verma, P. Burke, M. Sherwin and A. Gossard, "An improved model for non-resonant terahertz detection in field-effect transistors," *Journal of Applied Physics,* vol. 111, no. 2, pp. 024502--024502, 2012.

[9] M. Dyakonov and M. Shur, "Shallow water analogy for a ballistic field effect transistor: New mechanism of plasma wave generation by dc current," *Physical review letters,* vol. 71, no. 15, pp. 2465--2468, 1993.

[10] A. Lisauskas, S. Boppel, J. Matukas, V. Palenskis, L. Minkevičius, G. Valušis, P. Haring-Bolívar and H. G. Roskos, "Terahertz responsivity and low-frequency noise in biased silicon field-effect transistors," *Appl. Phys. Lett.,* vol. 102, no. 15, 2013.

[11] M. Sakowicz, M. Lifshits, O. Klimenko, F. Schuster, D. Coquillat, F. Teppe and W. Knap, "Terahertz responsivity of field effect transistors versus their static channel conductivity and loading effects," *Journal of Applied Physics,* vol. 110, no. 5, pp. 054512--054512, 2011.

[12] R. Robucci, J. D. Gray, L. K. Chiu, J. Romberg and P. Hasler, "Compressive sensing on a CMOS separable-transform image sensor," *Proceedings of the IEEE,* vol. 98, no. 6, pp. 1089--1101, 2010.

[13] B. Szentpáli, P. Basa, P. Furjes, G. Battistig, I. Bársony, G. Károlyi, T. Berceli, V. Rymanov and A. Stohr, "Thermopile antennas for detection of millimeter waves," *Applied Physics Letters,* vol. 96, no. 13, pp. 133507--133507, 2010.

[14] T. A. Elkhatib, V. Y. Kachorovskii, W. J. Stillman, D. B. Veksler, K. N. Salama, X.-C. Zhang and M. S. Shur, "Enhanced plasma wave detection of terahertz radiation using multiple high electron-mobility transistors connected in series," *Microwave Theory and Techniques, IEEE Transactions on,* vol. 58, no. 2, pp. 331--339, 2010.

[15] T. A. Elkhatib, D. B. Veksler, K. N. Salama, X.-C. Zhang and M. S. Shur, "Enhanced terahertz detection using multiple GaAs HEMTs connected in series," in *Microwave Symposium Digest, 2009. MTT'09. IEEE MTT-S International*, 2009.

[16] D. L. Donoho, "Compressed sensing," *Information Theory, IEEE Transactions on*, vol. 52, no. 4, pp. 1289--1306, 2006.

[17] N. Oda, M. Sano, K. Sonoda, H. Yoneyama, S. Kurashina, M. Miyoshi, T. Sasaki, I. Hosako, N. Sekine and T. Sudou, "Development of terahertz focal plane arrays and handy camera," in *SPIE Defense, Security, and Sensing*, 2011.

[18] N. Kawai and S. Kawahito, "Effectiveness of a correlated multiple sampling differential averager for reducing 1/f noise," *IEICE Electronics Express*, vol. 2, no. 13, pp. 379--383, 2005.

[19] T. Ouchi, K. Kajiki, T. Koizumi, T. Itsuji, Y. Koyama, R. Sekiguchi, O. Kubota and K. Kawase, "Terahertz Imaging System for Medical Applications and Related High Efficiency Terahertz Devices," *Journal of Infrared, Millimeter, and Terahertz Waves*, pp. 1--13, 2013.

[20] S.-H. Ding, Q. Li, Y.-D. Li and Q. Wang, "Continuous-wave terahertz digital holography by use of a pyroelectric array camera," *Optics letters*, vol. 36, no. 11, pp. 1993--1995, 2011.

[21] M. S. Heimbeck, M. K. Kim, D. A. Gregory and H. O. Everitt, "Terahertz digital holography using angular spectrum and dual wavelength reconstruction methods," *Opt. Express*, vol. 19, no. 10, pp. 9192--9200, 2011.

[22] Y. Zhang, W. Zhou, X. Wang, Y. Cui and W. Sun, "Terahertz digital holography," *Strain*, vol. 44, no. 5, pp. 380--385, 2008.

[23] S. Wang and X. Zhang, "Pulsed terahertz tomography," *Journal of Physics D: Applied Physics*, vol. 37, no. 4, p. R1, 2004.

[24] X. Wang, Y. Cui, W. Sun and Y. Zhang, "Terahertz digital holography," in *Photonics and Optoelectronics Meetings 2011*, 2012.

[25] T. Latychevskaia, J.-N. Longchamp and H.-W. Fink, "When holography meets coherent diffraction imaging," *Optics express*, vol. 20, no. 27, pp. 28871--28892, 2012.

[26] F. Schuster, D. Coquillat, H. Videlier, M. Sakowicz, F. Teppe, L. Dussopt, B. Giffard, T. Skotnicki and W. Knap, "Broadband terahertz imaging with highly sensitive silicon CMOS detectors," *Opt. Express*, vol. 19, no. 8, pp. 7827--7832, Apr 2011.

[27] J. Bobin, J.-L. Starck and R. Ottensamer, "Compressed sensing in astronomy," *Selected Topics in Signal Processing, IEEE Journal of*, vol. 2, no. 5, pp. 718--726, 2008.

[28] D. Gross, Y.-K. Liu, S. T. Flammia, S. Becker and J. Eisert, "Quantum state tomography via compressed sensing," *Physical review letters*, vol. 105, no. 15, p. 150401, 2010.

[29] W. L. Chan, K. Charan, D. Takhar, K. F. Kelly, R. G. Baraniuk and D. M. Mittleman, "A single-pixel terahertz imaging system based on compressed sensing," *Applied Physics Letters*, vol. 93, no. 12, pp. 121105--121105, 2008.

[30] C. Watts, W. Padilla and D. Shrekenhamer, "THz Imaging With Metamaterials," in *Infrared millimeter and terahertz waves, 2013 International Conference on*, 2013.

[31] D. Needell and J. A. Tropp, "Cosamp: iterative signal recovery from incomplete and inaccurate samples," *Communications of the ACM*, vol. 53, no. 12, pp. 93--100, 2010.

[32] Y. Ji and Z. Yang, "Mixed-norm Subspace Pursuit Algorithm for Compressed Sensing in the Presence of Impulsive Noise," *Journal of Computational Information Systems*, vol. 10, no. 13, pp. 5637--5648, 2014.

[33] R. Ward, "Compressed sensing with cross validation," *Information Theory, IEEE Transactions on*, vol. 55, no. 12, pp. 5773--5782, 2009.

[34] D. Needell and J. A. Tropp, "CoSaMP: Iterative signal recovery from incomplete and inaccurate samples," *Applied and Computational Harmonic Analysis*, vol. 26, no. 3, pp. 301--321, 2009.

[35] L. Mancera and J. Portilla, "L0-norm-based sparse representation through alternate projections," in *Image Processing, 2006 IEEE International Conference on*, 2006.

[36] H. Mohimani, M. Babaie-Zadeh and C. Jutten, "A Fast Approach for Overcomplete Sparse Decomposition Based on Smoothed L0 norm," *Signal Processing, IEEE Transactions on*, vol. 57, no. 1, pp. 289--301, 2009.

[37] Z. Popovic and E. N. Grossman, "THz metrology and instrumentation," *Terahertz Science and Technology, IEEE Transactions on*, vol. 1, no. 1, pp. 133--144, 2011.

[38] K. K. Hung, P. K. Ko, C. Hu and Y. C. Cheng, "A unified model for the flicker noise in metal-oxide-semiconductor field-effect transistors," *Electron Devices, IEEE Transactions on*, vol. 37, no. 3, pp. 654--665, 1990.

[39] D. Gergelyi and P. Földesy, "Digital Micromirror Device (DMD) projector based test bench for vision chips," in *Cellular Nanoscale Networks and Their Applications (CNNA), 2010 12th IEEE International Conference On*, Berkeley, CA, 2010.

[40] D. M. Malioutov, S. R. Sanghavi and A. S. Willsky, "Sequential compressed sensing," *Selected Topics in Signal Processing, IEEE Journal of*, vol. 4, no. 2, pp. 435--444, 2010.

[41] J. Haupt and R. Nowak, "Signal reconstruction from noisy random projections," *Information Theory, IEEE Transactions on*, vol. 52, no. 9, pp. 4036--4048, 2006.

[42] F. Sizov and A. Rogalski, "THz detectors," *Progress in Quantum Electronics*, vol. 34, no. 5, pp. 278 - 347, 2010.

[43] P. Földesy, D. Gergelyi, C. Füzy és G. Károlyi, „Test and configuration architecture of a subthz cmos detector array," in *Design and Diagnostics of Electronic Circuits and Systems (DDECS), 2012 IEEE 15th Symposium on* , Tallin , 2012.

[44] P. Földesy, Z. Fekete, T. Pardy és D. Gergelyi, „Terahertz Spatial Light Modulator with Digital Microfluidic Array," in *26th Eurosensors Conference, appears in Journal of Procedia Engineering*, Kraków , 2012.

[45] P. Földesy and D. Gergelyi, "Serially connected MOS terahertz sensor array," in *Infrared millimeter and terahertz waves (IRMMW), International Conference on*, Mainz, 2013.

[46] G. Károlyi, D. Gergelyi and P. Földesy, "Sub-Thz Sensor Array with Embedded Signal Processing in 90nm CMOS Technology," *Sensors Journal, IEEE*, vol. PP, no. 99, pp. 1-1, 2013.

[47] H.-B. Liu, G. Plopper, S. Earley, Y. Chen, B. Ferguson and X.-C. Zhang, "Sensing minute changes in biological cell monolayers with THz differential time-domain spectroscopy," *Biosensors and bioelectronics*, vol. 22, no. 6, pp. 1075--1080, 2007.

[48] Z. D. Taylor, R. S. Singh, D. B. Bennett, P. Tewari, C. P. Kealey, N. Bajwa, M. O. Culjat, A. Stojadinovic, H. Lee and J.-P. Hubschman, "THz medical imaging: in vivo hydration sensing," *Terahertz Science and Technology, IEEE Transactions on*, vol. 1, no. 1, pp. 201--219, 2011.

[49] D. Veksler, F. Aniel, S. Rumyantsev, M. Shur, N. Pala, X. Hu, R. Fareed and R. Gaska, "GaN heterodimensional schottky diode for THz detection," in *Sensors, 2006 IEEE International*, 2006.

[50] R. M. Woodward, V. P. Wallace, R. J. Pye, B. E. Cole, D. D. Arnone, E. H. Linfield and M. Pepper, "Terahertz pulse imaging of ex vivo basal cell carcinoma," *Journal of Investigative Dermatology*, vol. 120, no. 1, pp. 72--78, 2003.

[51] D. Veksler, A. Muravjov, V. Y. Kachorovskii, T. Elkhatib, K. Salama, X.-C. Zhang and M. Shur, "Imaging of field-effect transistors by focused terahertz radiation," *Solid-State Electronics*, vol. 53, no. 6, pp. 571--573, 2009.